Calibration and Alignment of the CMS Silicon Tracking Detector

Dissertation

zur Erlangung des Doktorgrades
des Departments Physik
der Universität Hamburg

vorgelegt von

Markus Stoye

aus Köln

Hamburg
2007

Gutachter der Dissertation:	Prof. Dr. P. Schleper Prof. Dr. J. Mnich
Gutachter der Disputation	Prof. Dr. P. Schleper Prof. Dr. B. Naroska
Datum der Disputation:	12.7.2007
Vorsitzender des Promotionsausschusses:	Prof. Dr. C. Hagner
Vorsitzender des Prüfingsausschusses:	Prof. Dr. G. Huber
Dekan der MIN-Fakultät:	Prof. Dr. A. Frühwald

Abstract

The Large Hadron Collider (LHC) will dominate the high energy physics program in the coming decade. The discovery of the standard model Higgs boson and the discovery of super-symmetric particles are within the reach at the energy scale explored by the LHC. However, the high luminosity and the high energy of the colliding protons lead to challenging demands on the detectors. The hostile radiation environment requires irradiation hard detectors, where the innermost subdetectors, consisting of silicon modules, are most affected.

This thesis is devoted to the calibration and alignment of the silicon tracking detector. Electron test beam data, taken at DESY, have been used to investigate the performance of detector modules which previously were irradiated with protons up to a dose expected after 10 years of operation. The irradiated sensors turned out to be still better than required.

The performance of the inner tracking systems will be dominated by the degree to which the positions of the sensors can be determined. Only a track based alignment procedure can reach the required precision. Such an alignment procedure is a major challenge given that about 50000 geometry constants need to be measured. Making use of the novel χ^2 minimization program Millepede II[1] an alignment strategy has been developed in which all detector components are aligned simultaneously, as many sources of information as possible are used, and all correlations between the position parameters of the detectors are taken into account. Utilizing simulated data, a proof of concept of the alignment strategy is shown.

[1]Developed by V. Blobel.

Zusammenfassung

Die Experimente am Large Hadron Collider (LHC) werden in den nächsten Jahren die Hochenergie-Physik dominieren. Das Higgs-Boson des Standardmodells und supersymmetrische Teilchen werden bei Energien erwartet, welche vom LHC erreicht werden. Die hohe Luminosität und die hohe Energie der kollidierenden Protonen führen zu besonderen Ansprüchen an die Detektoren. Die extremen Strahlungsbedingungen erfordern strahlungsharte Detektoren. Dies gilt insbesondere für den innersten Detektor, den Spurdetektor aus Silizium-Sensoren.
Thema dieser Arbeit sind Kalibrierung und Alignierung des Silizium-Spurdetektors. Silizium-Streifen-Detektoren sind mit einem Elektronen-Strahl getestet worden. Die Detektoren sind zuvor mit Dosen von Protonen bestrahlt worden, welche einer Strahlenbelastung am LHC von bis zu 10 Jahren Betrieb entsprechen.
Die Qualität der Messungen im Spurdetekor ist dadurch limitiert, wie gut die Positionen der einzelnen Detektoren bestimmt werden können. Die erforderte Genauigkeit kann nur mit einer spur-basierten Alignierung erreicht werden. Diese Alignierung ist eine besondere Herausforderung, da circa 50.000 geometrische Parameter bestimmt werden müssen. Das neue χ^2-Minimierungs Programm Millepede II[2] wird verwendet, um eine Strategie zu erarbeiten, in welcher die Positionen aller Detektoren gleichzeitig bestimmt werden. Dabei werden so viele Informations-Quellen wie möglich genutzt und alle Korrelationen zwischen den geometrischen Parametern berücksichtigt. Es wird mit simulierten Daten gezeigt, dass das Konzept zu erfolgreichen Ergebnissen führt.

[2]Entwickelt von V. Blobel.

Contents

Chapter 1

Introduction

Colliding high energy particles and measuring their scattering has a long and successful history in physics. The existence of nuclei within atoms was discovered via scattering experiments about 100 years ago. Ever-since the particles energies and collision rates have been increased, giving new insights into particle physics. In the last decades, the standard model of particle physics was validated to high precision in accelerator (and other) experiments. However, not all particles of the standard model have been proven to exist and the validity of the theory is limited to a certain energy range. The Large Hadron Collider (LHC), built in the old LEP tunnel at CERN, will increase the center of mass energy of the colliding protons reached in previous experiments by about a factor of seven and the luminosity by a factor of $O(100)$ with respect to current collision experiments. It should become possible to find the last unknown particle within the standard model, the Higgs boson, and to explore physics up to a few TeV. Two multi purpose detectors, ATLAS and CMS, are currently set up at the LHC particle collision points. The LHC leads to high demands on the detectors measuring the particles originating from the collisions. The increase of luminosity and center of mass energy leads to unprecedentedly high event rates. About 20 inelastic collisions with altogether about 1000 charged particles occur per bunch crossing at design luminosity at a bunch collision rate of 40 MHz.

1.1 Challenge to Inner Tracking Detector

The LHC physics goals lead to especially challenging requirements for the inner tracking devices. To be able to associate the correct measurements to the individual tracks, a high granularity, fast readout electronics, and a good signal to noise ratio are of vital importance. The minimally required signal to noise ratio of individual measurements was estimated to be 10 [1]. This ratio needs to be maintained despite the hostile radiation environment which is caused by the high particle flux. After 10 years of operation corresponding to an integrated luminosity of 500 pb^{-1}, the innermost detectors of the silicon strip tracker will be irradiated by fast hadrons to a dose of $15.7 \cdot 10^{13}$

neutron equivalent fluence at 1 MeV [2]. It is therefore mandatory to test the irritation hardness of the sensors. In this thesis silicon strip modules of final design were investigated, which previously were irradiated with protons to a level corresponding to up to about 10 year of their operation. The modules were tested in an electron test beam at DESY.

Another key demand is the resolution of the track measurements. The required resolution of the transverse momentum at 100 GeV is ∼1% using tracker information only. The required resolution of the distance of closest approch to the vertex is aimed to be ∼10 μm. The dominating source of degradiation of the resolution are the errors of the position of the individual sensors (misalignment). The high resolution of the tracker demands that the sensor positions are determined to few μm starting from initial displacements of $O(100)$ μm. Misalignment scenarios representing the beginning of data taking (*first data*) and a later phase (*long term*) have been defined in the CMS collaboration to study the impact of misalignment. Figure 1.1 (left) shows the transverse momentum resolution as a function of the pseudorapitity (η). In figure 1.1 (right) the reconstructed Z^0/γ^* mass from di-muon events is shown. The resolution of the Z^0 mass measurement of a single event decreases by a factor of 1.5, from 1.5 GeV with the ideal geometry to 2.5 GeV with the *first data* scenario [3]. The resolution of the distance of closest approach decreases from 10 μm to 32 μm. An overview of performed studies on the effect of misalignment on analysis in the LHC experiments is given in [4].

However, so far no alignment procedure was presented which reached the precision assumed in the *long term* scenario. The knowledge from mounting precision, survey measurements, and the Laser Alignment System will not be sufficient to reach the precision required. Only a track based alignment strategy will allow to determine the sensors positions to the μm level. The large number of silicon modules (∼16000), which is about a factor of ten larger than for current silicon detectors, leads to com-

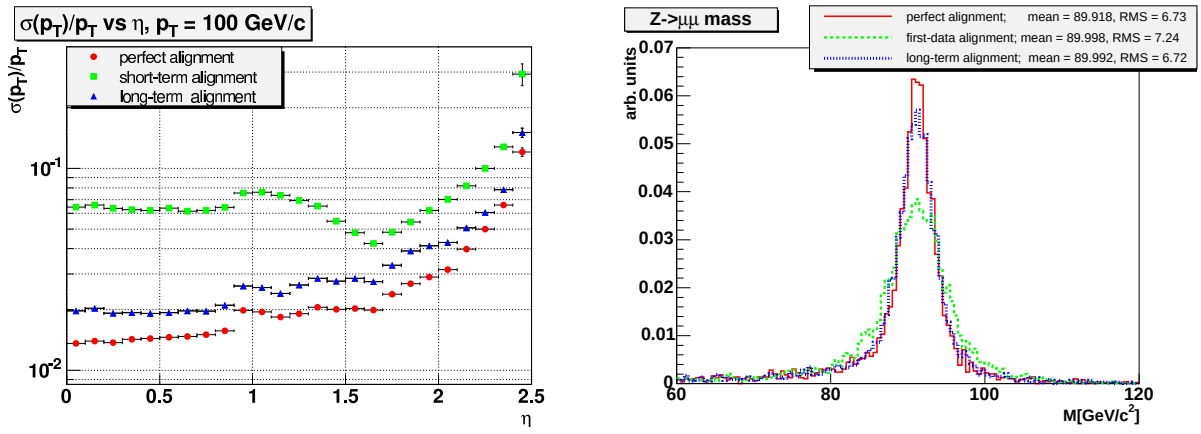

Figure 1.1: Left: Relative transverse momentum resolution as a function of η for different misalignment scenarios. Right: Reconstructed mass of $Z^0\gamma^* \rightarrow \mu\mu$ events for different misalignment scenarios.

putational problems for certain algorithms. In addition the "golden channel" at e^+e^- colliders for alignment, namely $ee \rightarrow \mu\mu$, does not exist for proton colliders. Hence previous alignment procedures cannot easily be adopted to the CMS tracker. A major alignment problem is that track based alignment is hardly sensitive to certain correlated displacements of sensors. For this reason a strategy was adopted which includes following key ingredients:

- Tracks from complementary datasets.
- Z^0 mass constraint.
- Vertex constraint.
- Survey measurements.
- Mechanical mounting precision.
- Hierarchy of mechanical support frames.
- Inclusion of all correlations between position parameters.
- Rejection of corrupted tracks.
- Expected symmetries of track parameters.

The new algorithm Millepede II [5] is used to perform a global fit determining all alignment constants from several million tracks simultaneously. The final aim is to develop a (standalone) tracker alignment strategy without using informations from other detector components.

Chapter 2

Physics at LHC

This section is intended to briefly summarize the capabilities of the LHC and give a motivation for exploring physics at the TeV scale. Only a few typical searches are mentioned to highlight the discovery potential of LHC experiments. Many detailed analysis can be found in the physical technical design reports (TDR) of ATLAS [6] and CMS [7].

2.1 The Standard Model of High Energy Physics

The Standard Model (SM) is a gauge quantum field theory which comprises our knowledge of the structure of matter. Matter is built of fermions (spin $\frac{1}{2}$ particles) and their interaction is mediated by the exchange of gauge bosons (spin 1 particles). The weak and the electromagnetic force are unified in the GWS-Model [8] and the corresponding gauge bosons are the γ, Z^0, and $W^{\pm}$. The Higgs-mechanism [9] has been incorporated into the GWS-Model in order to generate masses for the Z^0 and $W^{\pm}$ as well as for the fermions. The Higgs-mechanism introduces a new particle, the scalar Higgs boson. Only with this Higgs bosons, the WW scattering cross section does not violate unitarity at high energies ($\sim$ TeV). However, the Higgs boson mass needs to be $\lesssim$ TeV to limit the WW scattering cross section. The electroweak sector of the SM is based on the $SU(2)_I \otimes U(1)_Y$ symmetry, where I is the weak isospin and Y the hypercharge.
Leptons are fermions which interact by the electroweak force only, while quarks carry also the color charge of the strong interaction. The $SU(3)_C$ color symmetry can be assigned to the strong interaction and the 8 corresponding gauge boson are called gluons. The gluons are color charged and interact with each other, which leads to a decrease of the strong coupling constant at small distances (high energies). Hence high energy quarks and gluons can be understood as free particles (asymptotic freedom) and the strong coupling constant is small enough to allow perturbative calculations.
The SM has been very successful in explaining the data from laboratory experiments to date. However, there are shortcomings in the SM, a selection of these are discussed below.

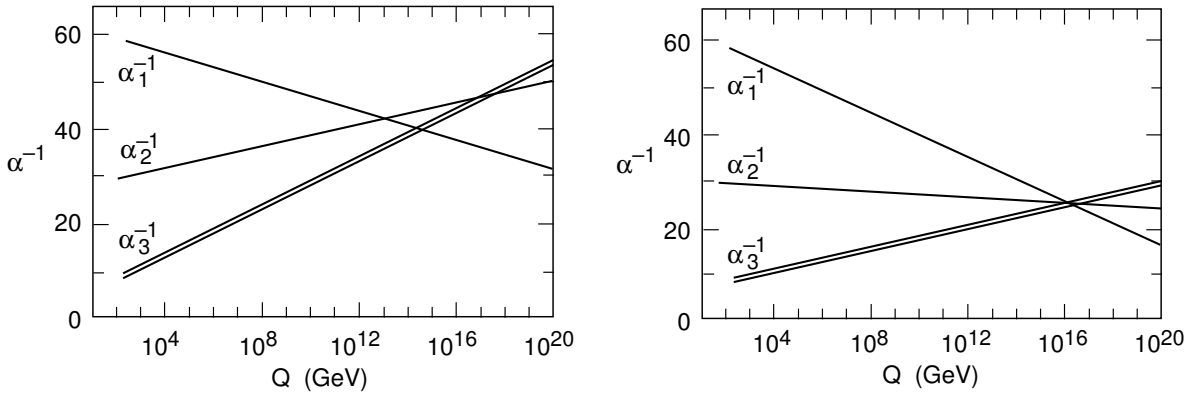

Figure 2.1: Inverse of running coupling constants. $\alpha_1^{-1}, \alpha_2^{-1}$, and α_3^{-1} are the inverse of the electromagnetic, the weak, and the strong interaction, respectively. Left: Running of coupling constants in the standard model. Right: Running of coupling constants for the minimal supersymmetric model and a SUSY scale of $\sim$ TeV.

- The SM does not unify the strong and electroweak forces. Grand Unifying Theories (GUT) unify these forces. A first model of this kind [10] assumed a broken $SU(5)$ symmetry which incorporates $SU(3) \otimes SU(2) \otimes U(1)$. GUTs allow proton decay and its lifetime depends on the GUT scale. The GUT scale predicted by $SU(5)$ symmetry is excluded by proton lifetime measurements.

- The visible Higgs mass is composed of a bare mass and radiative corrections. The leading term of the radiative corrections are quadratically dependent [11] on the cutoff energy Λ of the validity of the electroweak theory, which can be associated to the GUT scale. This term has to be subtracted from the bare mass squared. Only if the bare mass squared is know to 24 digits precision a Higgs mass of below a TeV results at the electroweak scale ($O(100)$) GeV. This problem is called the *fine tuning* problem.

- The large number of parameters (17 particles, 26 constants) and the fact that gravity is not included are further shortcomings of the theory. Also dark matter and dark energy observed in cosmology can not be explained within the SM.

However, there are extensions to the SM which resolve some of these shortcomings. A promising candidate is Supersymmetry (SUSY).

- SUSY introduces a fermion-boson symmetry, which postulates a fermion (boson) for each know boson (fermion). Adding the supersymmetric partner particles (sparticles) leads to radiative corrections which cancel the quadratically divergent terms of the Higgs mass, hereby solving the *fine tuning* problem of the SM. Supersymmetry is broken, since sparticles with the masses of the particles have

Energy per proton	7 TeV
Design luminosity	10^{34} cm^{-2}s^{-1}
Bunch separation	25 ns
Number of bunches	2808
Number of particles per bunch	1.15 10^{11}
RMS beam radius at IP	16.7 μm
Number of collisions per crossing	$\sim$20

Table 2.1: The start-up LHC machine design parameters.

not been observed. However, in order to cancel the quadratically divergent radiative correction terms the sparticles masses (SUSY scale) should not be above the $\sim$ TeV range. The sparticles change the running of the coupling constants once the SUSY scale is reached. All three coupling constants meet at a GUT scale of $O(10^{16})$ GeV if a SUSY scale of $\sim$ TeV is assumed (figure 2.1). Remarkably, the unification of the coupling constants results in a SUSY scale motivated by a different constraint (quadratic divergence cancellation) and the GUT scale is set to a value above the region excluded by proton lifetime measurements.
In addition sparticles lead to promising candidates for dark matter. The above arguments hold true if the number of sparticles (R-parity) is conserved (or at least R-parity violation is strongly suppressed), leading to at least one stable sparticle. Otherwise the proton lifetime would be decreased to excluded regions and the dark matter candidates would decay.

In conclusion, extending the experimental reach of high energy physics to the TeV range makes it possible to explore a mass-range where the Higgs boson and sparticles are preferably expected.

2.2 The Large Hadron Collider

The LHC is a proton-proton collider built in the old LEP tunnel at CERN. The design luminosity is 10^{34} cm^{-2}s^{-1} and the center of mass energy of colliding protons is 14 TeV. The bunch separation is 25 ns. At nominal luminosity about 20 collisions occur per crossing. The most important beam parameters are summarized in table 2.1. The luminosity will (presumably) be increased in several steps up to the design luminosity as shown in table 2.2.

2.2.1 Discovery Potential

The quarks and glouns in protons with TeV energies are asymptotically free. In that sense a "parton luminosity" can be defined, which incorporates the parton distribution functions and describes the luminosity for quark-quark, gluon-quark and gluon-gluon

	First Physics 2008	2009	2010	2011-2013
Luminosity [$cm^{-2}s^{-1}$]	$5 \cdot 10^{31} \rightarrow 4 \cdot 10^{32}$	10^{33}	$2 \cdot 10^{33}$	10^{34}
Integrated luminosity [$fb^{-}1$]	1	5	10	300

Table 2.2: Expected luminosities at LHC.

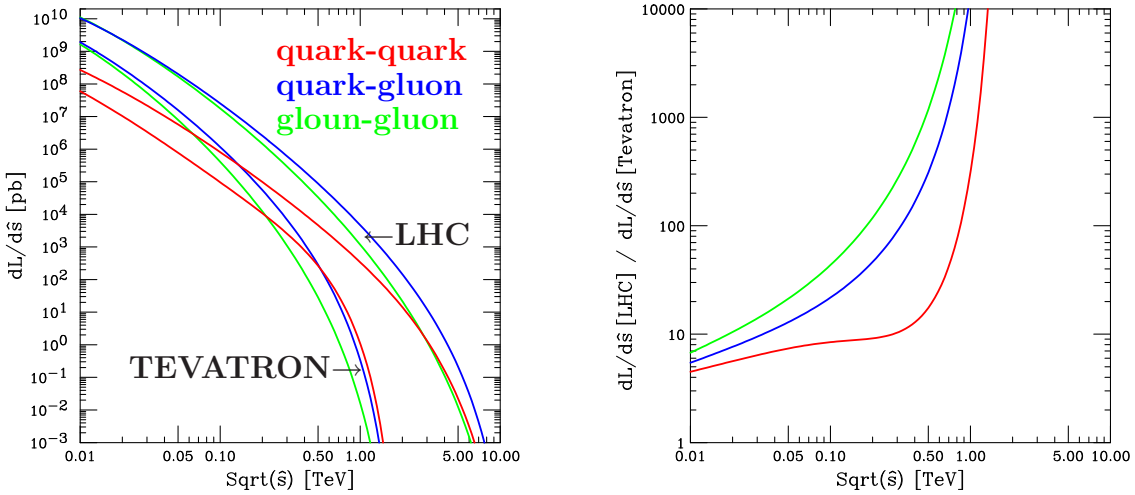

Figure 2.2: Left: Parton luminosity differentially in the center of mass energy ($\sqrt{\hat{s}}$) for the LHC and the TEVATRON. Right: Ratio of differential parton luminosities of the LHC and the TEVATRON (from [12]).

collisions. The parton differential luminosities as a function of the center of mass energy are compared in absolute numbers to the currently running TEVATRON collider in figure 2.2 (left) and as a ratio between them in 2.2 (right). The TEVATRON has a proton-antiproton center of mass energy of 2 TeV. At the LHC collider the quark-quark luminosities are nearly an order of magnitude larger at 500 GeV and the ratios of other luminosities are even more in favor of the LHC. This convincingly illustrates that a new energy region is explored. The proton-proton cross sections are illustrated in figure 2.3.

Higgs Search The Higgs boson has been directly searched for at the LEP experiments and a Higgs mass below 114 GeV is excluded at the 95% confidence level. Also an indirect search has been performed, in which the consistency between the precise measurements of the eletroweak sector of the SM and a given Higgs mass is tested. The result is shown in figure 2.4 and it can be concluded that a SM Higgs boson mass should be below 182 GeV 95% confidence level [13], if the direct search at LEP is included.

If Higgs bosons are produced at the LHC, the branching ratios for the decay channels

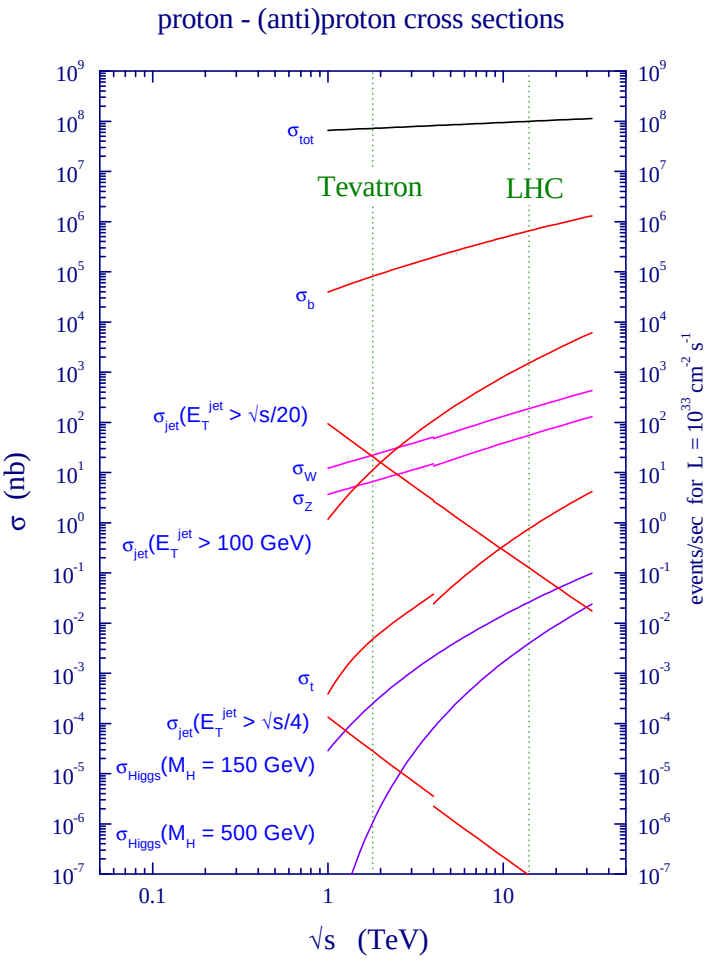

Figure 2.3: Total cross section and cross sections of individual SM processes as a function of the proton-(anti)proton center of mass energy [12].

will depend on the Higgs mass (figure 2.5 left). Although b quark pair production is the dominating decay channel at small Higgs boson masses, it will be hard to disentangle the Higgs signal in this channel from the large background from strong interaction processes which include b pairs. A cleaner signature and better signal to background ratios are achieved in the decay of the Higgs boson to two photons, two Z^0 or a $W^{\pm}$ pair, respectively. As a result, the discovery potential for a light Higgs boson (115-130 GeV) is the highest in the di-photon decay channel, while at higher masses the decay into the two Z^0 or a $W^{\pm}$ pair are the discovery channels. The important di-photon channel leads to high demands on the design of the electromagnetic calorimeter, where the photon energy is measured. The searches for the Higgs decaying to heavy gauge

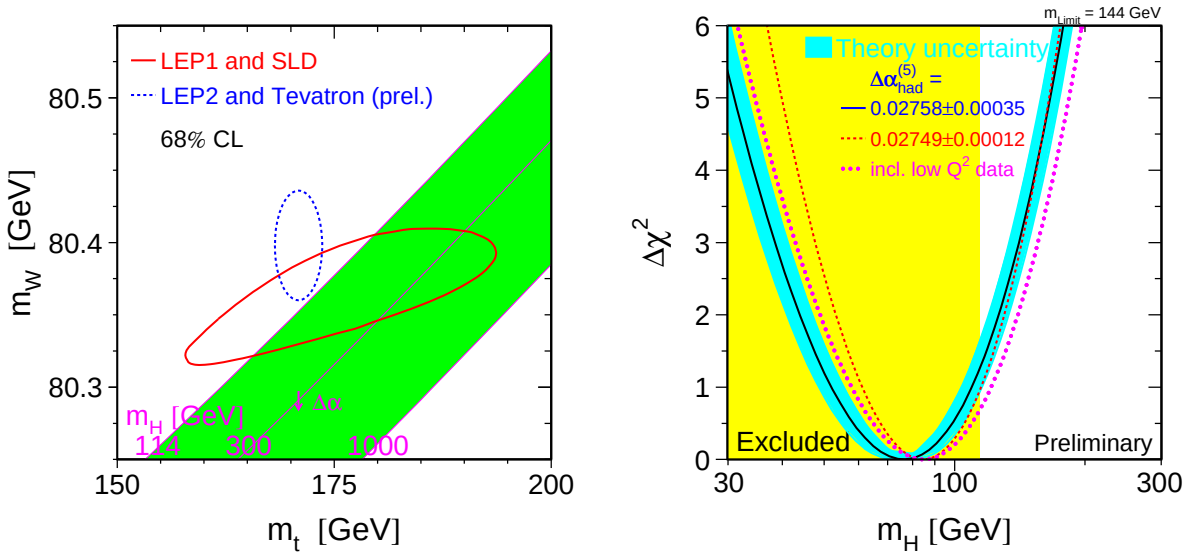

Figure 2.4: Left: W mass versus top quark mass. The ratio of W mass and top quark mass depends on the Higgs mass. The violet lines indicate lines at constant Higgs boson masses. The blue dotted curve shows the experimentally determined regions (68% confidence level). Right: χ^2 of a SM fit to electrowaek measurements as a function of the Higgs boson mass. The yellow region is excluded by the direct search ([13] May 2007).

bosons, which then decay leptonically, set demands on the transverse momentum resolution of the tracking devices and on muon identification.

SUSY Search If R-parity is conserved, then the produced sparticle pairs cannot decay completely to SM particles. If lightest and hence stable sparticles is neutral, it will leave the detector undetected, similar to the SM neutrinos, leading to large missing transverse energies. This clear signature in combination with the large expected cross sections for SUSY processes would typically lead, already with few fb^{-1} of data, to indications of R-parity conserving SUSY at the TeV level. The missing energy measurement requires good hermeticy of the hadron calorimeter.

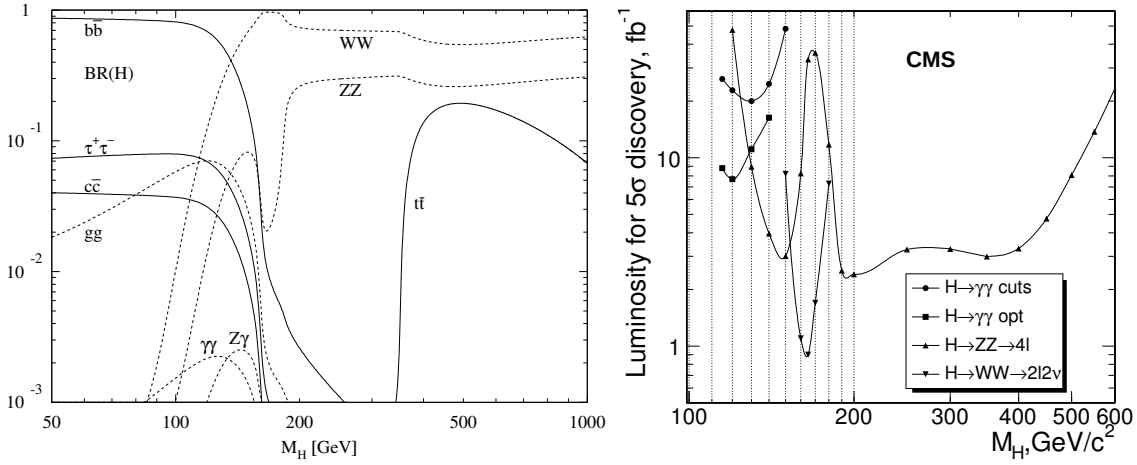

Figure 2.5: Left: Branching ratio for Higgs boson decay as a function of the Higgs boson mass. Right: Discovery potential for different searches as a function of the Higgs boson mass [7].

Chapter 3

The Compact Muon Solenoid Detector (Draft 1)

The **C**ompact **M**uon **S**olenoid detector is a 4π multi-purpose detector. The innermost part is the silicon tracking detector, measuring charged particle trajectories in the magnetic field and hence their momenta. The tracker is enclosed by the electromagnetic calorimeter, which measures the energy of electrons and photons. Behind the electromagnetic calorimeter is the hadron calorimeter, which measures the energies of strongly interacting particles. The coil of the superconducting solenoid magnet encloses the previous detectors. The magnet stores more energy in the magnetic field, than any magnet ever built before. The magnet parameters are listed in table 5.1. Behind the coil is the muon system which is used for muon identification and measurements of their momentum. The muon system is embedded in the iron yoke of the magnet.
An overview of the CMS is given in figure 3.1. The coordinate convention is such that the z-direction is parallel to the beam line, the y-direction is vertical, and the x-direction is horizontal and points to the center of the LHC ring. The center of the detector is the origin of the coordinate system.
The detector components are described in more detail in the following sections, starting from the inner tracking devices which are explained in more detail, since this thesis concentrates on their calibration and radiation hardness.

Field	4 T
Inner Bore	5.9 m
Length	12.9m
Stored Energy	2.7 GJ
Current	19.5 kA

Table 3.1: Parameters of the superconducting magnet.

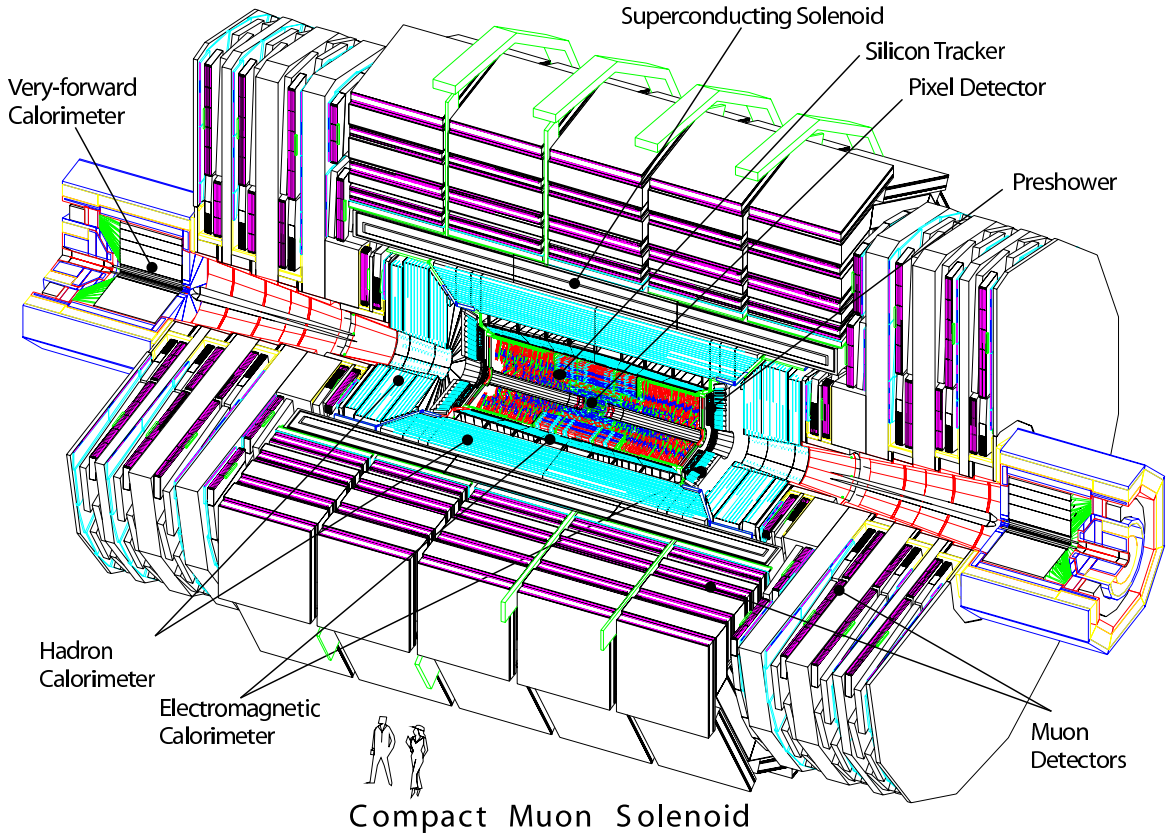

Figure 3.1: An exploded view of the CMS detector [2].

3.1 Silicon Tracking Detector

The CMS silicon tracker [14] has been designed to be able to cope with the high particle flux expected at the LHC experiments. In order to ensure an effective pattern recognition, it has been designed such that the occupancy of the silicon sensor channels is small, ranging from 10^{-4} for pixel sensors to the percent level for strip sensors. The granularity of the detectors decreases with the distance to the interaction point, since the particle flux decreases, too.
Another requirement has been a small relative error of the transverse momentum (p_t) measurements. At 1 TeV it should be about 10%. A simplified Glückstein-formula [15], which is neglecting material interaction and assuming the same resolution for all sensors, shows how this demand translates into design parameters:

$$\left(\frac{\sigma(p_t)}{p_t}\right) = \frac{\sigma_{hit}}{0.3BL^2}\sqrt{\frac{720}{N_{hit}+4}}, \tag{3.1}$$

where B is the magnetic field in Tesla and L corresponds to the radial extension of the tracker in cm. σ_{hit} is the sensor's resolution and N_{hit} the number of hits per track. The formula shows that large radial extension and a high magnetic field are key ingredients for a good energy resolution.
A further aspect of tracker design is its material budget. The aim is to minimize the radiation length of the material crossed. For the central region the radiation length is about 0.4 X_0, as can be seen in figure 3.2. The rather large amount of material in the tracker leads to significant energy loss, multiple scattering for electrons, and to photon conversions.

In the following the mechanical layout of the tracker is described, including the laser alignment system. Afterward the default algorithm for track reconstruction and important performance parameters are presented.

3.1.1 Detector Layout

The tracker consists of about 25000 silicon sensors which have altogether a surface of 210 m^2. It is the largest silicon tracker built up to now, having a diameter of 2.4 m and a length of 5.4 m (figure 3.3). The sensors are generally mounted such that a overlap with the neighboring sensors in the order of a mm exists. However, the pixel sensors do not overlap with their neighbors in the z direction. The different substructures of the tracker are described in the following.

Pixel Detector

The pixel detector is divided into the Pixel Barrel (PB) and the Pixel Endcaps (PE) as is shown in figure 3.4. The PB is composed of an upper (y+) and a lower (y-) half barrel. The radial position of the layers are 4.4 cm, 7.3 cm, and 10.2 cm. The layers

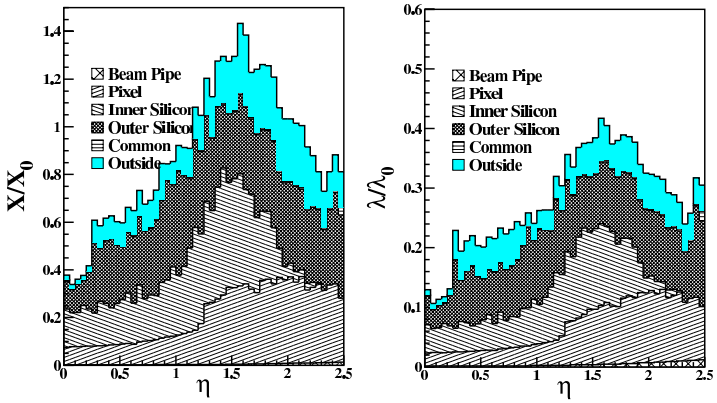

Figure 3.2: The material budget of the tracker and the beam pipe as a function of η [2]. Left: Radiation length as a function of η. Right: Interaction length as a function of η.

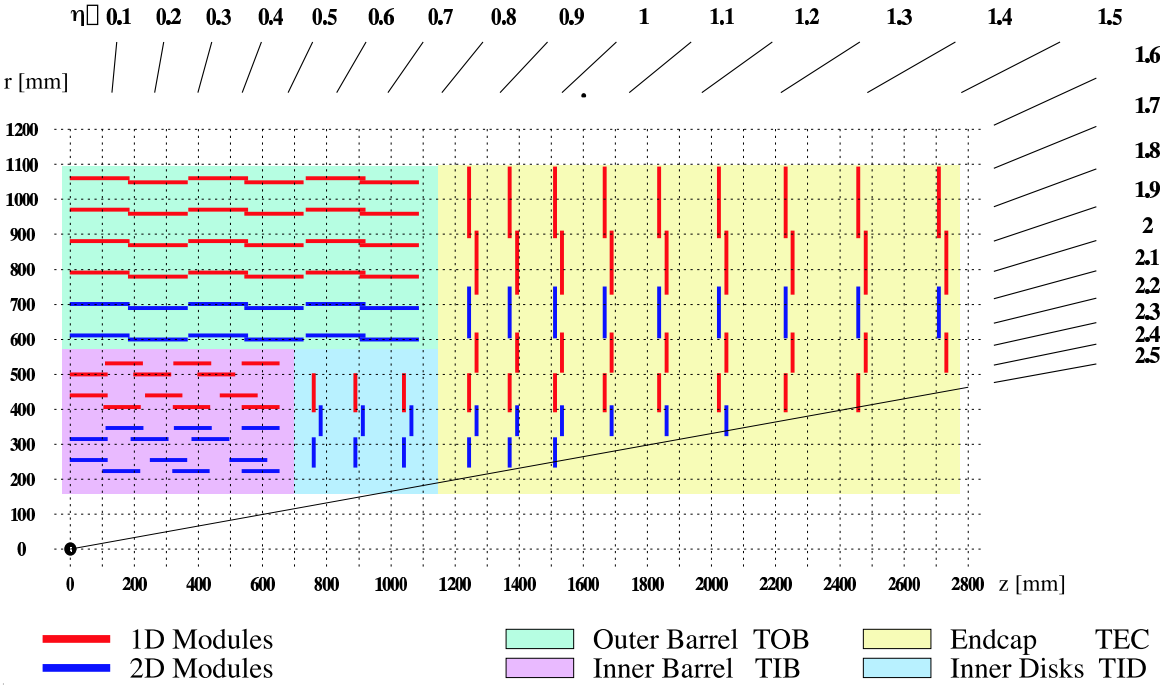

Figure 3.3: Layout of one quarter of silicon tracker in the r-z projection with η coverage indicated.

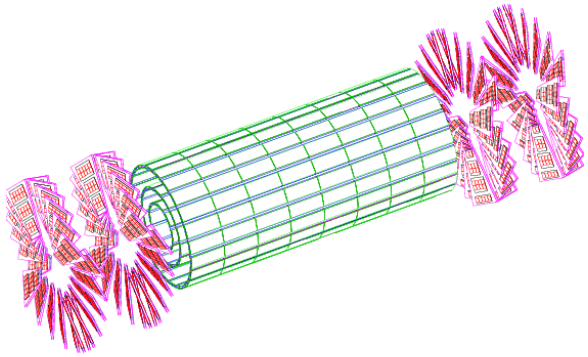

Figure 3.4: Schematic illustration of the pixel detector.

are composed of ladders, which include 8 pixel sensors each.
The Pixel Endcaps (PE) have two end disks each, which extend from 6 to 15 cm in radius and are placed on each side at $|z| = 34.5$ cm and 46.5 cm. The disks consist of blades which are assembled in a turbine-like geometry. The blades are tilted by 20° with respect to the disk plane, this leads to an improvement of the resolution by charge sharing due to the Lorenz drift. If not tilted, the blades surfaces would be perpendicular to the magnetic field. Each blade holds 24 pixel modules.
The pixel sensor parameters are listed in table 3.2. The resolution in rϕ is about 10 μm, while the resolution in the other measured direction is about 20 μm [16]. The small pixel size leads to an occupancy of only 10^{-4} at nominal luminosity, despite of the small distance to the interaction point.

part	number	thickness [μm]	mean pitch [μm]
PB	768	285	100 × 150
PE	672	285	100 × 150
TIB	2724	320	81,118
TOB	5208	500	122,183
TID	816	320	97,128,143
TEC 1-4	2512	320	96,126,128,143
TEC 5-7	3888	320	143,158,183
all	16588	-	-

Table 3.2: Geometric properties and numbers of silicon modules.

Silicon Strip Tracker

The silicon strip tracker is composed of several sub-detectors, namely the Tracker Inner Barrel (TIB), the Tracker Outer Barrel (TOB), the Tracker Inner Disks (TID),

and the Tracker Endcaps (TEC). Figure 3.3 shows an schematic overview of one quarter of the tracker in the r-z projection and the pseudo-rapidity coverage.

Both, TIB and TOB, consist of half barrels which are separated along the z coordinate into a $z+$ and a z- part. The first two layers of the half barrels are equipped with stereo modules. Each of the four layers of a TIB half barrel consist of two half shells, which separate the layer in a lower and an upper part. Small strings, with three modules each, are directly mounted on these half shells. The TOB half barrels do not have a mechanical layer support structure, however it effectively consists of six layers of sensors. Support structures called rods, carrying six modules lined up along the z direction, are directly mounted into the solid carbon half barrel frame. The TID is composed of three disks and fills the gap between TIB and TEC. Both TECs have nine disks, with 16 petals mounted on each disk. The petals divide into eight front petals and eight back petals which are placed on different sides of the disk. The number of modules per petal depends on the disk and ranges from 17 to 28 modules. The modules have been assembled directly onto the petals. There are seven rings in the TEC, the innermost ring is labeled ring 1. The term ring is convenient, but rings are not a physical support structures. Pictures of the supporting structures can be found in appendix A.

The number of modules of the detector components and their most important geometric properties are listed in table 3.2. The strip pitch increases for sensors further apart from the beam line and ranges from 81 μm to 183 μm. The resolution ($\approx$ pitch/$\sqrt{12}$) ranges therefore from 23 μm to 53 μm. The endcap sensors are wedge shaped and the strips on the sensors point to the beam line. A picture of such a sensor, mounted on a test beam support structure, can be seen in figure 4.8. The last layers are equipped with modules composed of two sensors which are bonded together, extending the module length. A picture of such a module is shown in figure 4.13. The stereo modules indicated in figure 3.3 are built of two sensors which are slightly rotated (100 mrad) with respect to each other. The typical resolution of stereo modules in the precisely measuring coordinate is 30 μm to 55 μm, while the less sensitive coordinate is measured to 230 μm to 530 μm. The large area covered by a single strip ($\sim$10 mm^2 - 36 mm^2) leads to an occupancy at the percent level at nominal luminosity.

Laser Alignment System for the Tracker

A Laser Alignment System (LAS) is integrated into the silicon strip tracker. Some of the silicon detectors in the TEC are transparent for the infra red laser beam light. The beam position can be measured by the sensors to a precision of 10 μm. Each back petal has a transparent sensor in ring 4 and 6. The two TECs, the TIB, and the TOB are connected with each other via a laser beam which penetrates ring 4 modules. Some light is reflected toward standard sensors on the last TIB layer and the first TOB layer. A schematic overview of the beam guidance is shown in figure 3.5

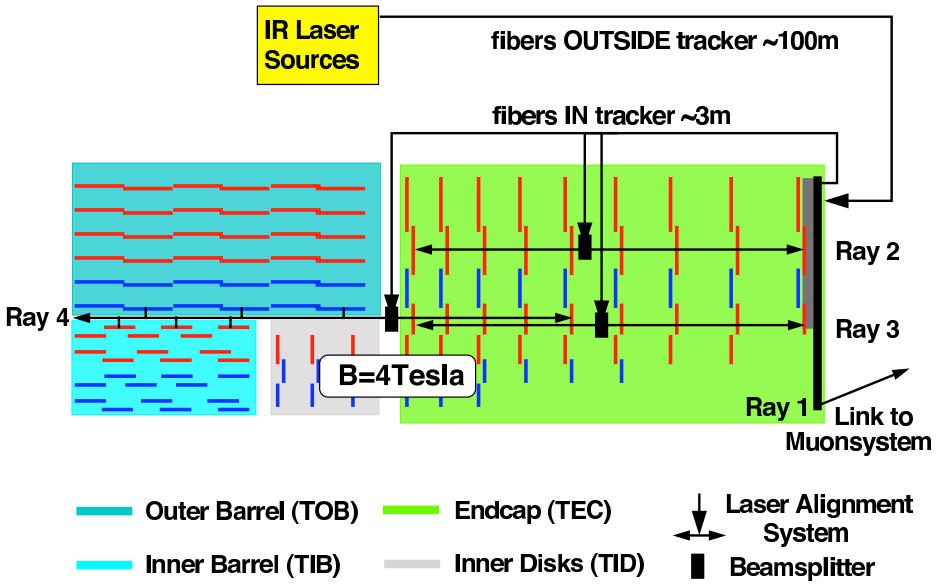

Figure 3.5: Layout of one quarter of beam guidance for the LAS in the r-z projection.

in a r-z projection. The pattern illustrated in the figure is repeated for the 8 back petals per disk. A dedicated description and simulation studies of the LAS system can be found in [17] and [18].

3.1.2 Performance

The performance of the tracker is mainly determined by its design, however also the reconstruction algorithms have an impact on the final quality of the measurements. The default track reconstruction of the CMS framework ORCA [19] is used in this thesis. A detailed description can be found in [20].

In the first phase the initial trajectory candidates, called seeds, are constructed for each pair of hits in the pixel detector, compatible with a given beam spot and a minimum transverse momentum requirement of 600 MeV. This initial candidate is then propagated out-wards via a Kalman Filter method, collecting new hits on each layer. For each hit in a layer, which is compatible with the trajectory, a new trajectory is introduced. In addition, a trajectory without a hit in this layer is introduced. Tracks that have large χ^2 or many missing hits are rejected in this process. Only a single trajectory is finally selected per seed and hits are only assigned to a single track. The procedure is called the Combinatorial Kalman Filter (CKF) and described in full detail in [20]. Finally, a track fit is performed with the associated hits. The final track fit includes a forward and backward Kalman Filter procedure and a final smoothing step. This procedures results in a set of optimal trajectory parameter estimates at every measured point along the track, with all

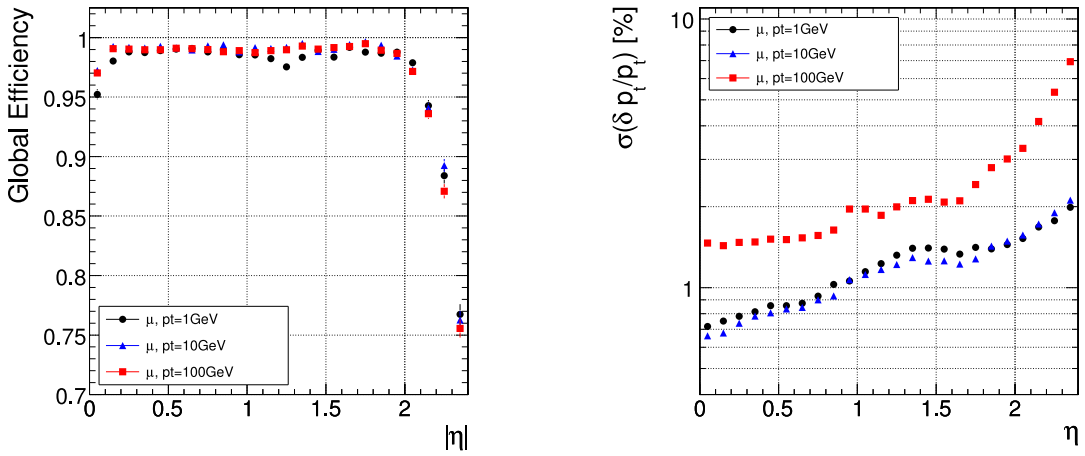

Figure 3.6: Left: The track reconstruction efficiency as a function of η. The dip at $\eta = 0$ is due to the pixel seeding used. Right: Relative error of transverse momentum measurements of tracks as a function of η.

measurements taken into account.

For single muons the reconstruction efficiency is about 98% for $\eta < 2$ and decreases for larger η (figure 3.6 left). The relative uncertainty of the transverse momentum measurement as a function of η is shown in figure 3.6 (right). The dependence of the relative transverse momentum measurement precision on the transverse momentum for the barrel region is shown in figure 3.10 (left) and for the endcap region in figure 3.10 (right). The design goal to keep the relative error below 10% at 1 TeV is reached. The relative uncertainty of tracks, typically used in this thesis, with a transverse momentum of 50 GeV is about 1%. The resolution of the point of closest approach to the beam line is about 10 μm in r and ranges from 10 μm to 40 μm in the z direction, depending on η [2].

3.2 Electromagnetic Calorimeter

For a Higgs boson mass below 130 GeV the process $H \rightarrow \gamma\gamma$ is the decay with the highest discovery potential for a SM Higgs boson, hence high demands were set on the performance of the ECAL. The electromagnetic calorimeter is made of lead tungstate scintillating crystals. The light is gathered with silicon avalanche photo-diodes. The 22 mm $\times$ 22 mm surface of the barrel crystals is similar to the Moliere radius which is typically 22 mm. It translates to a 1° (0.017 rad) coverage in ϕ and η. The depths translates to a radiation length of 25.8 X_0. The numbers for the endcap crystals are similar. All crystals approximately point toward the interaction point with an offset of 3°, minimizing energy loss if a particle transverses exactly between two crystals. The geometry and η coverage of the subcomponents are illustrated in figure 3.7. The

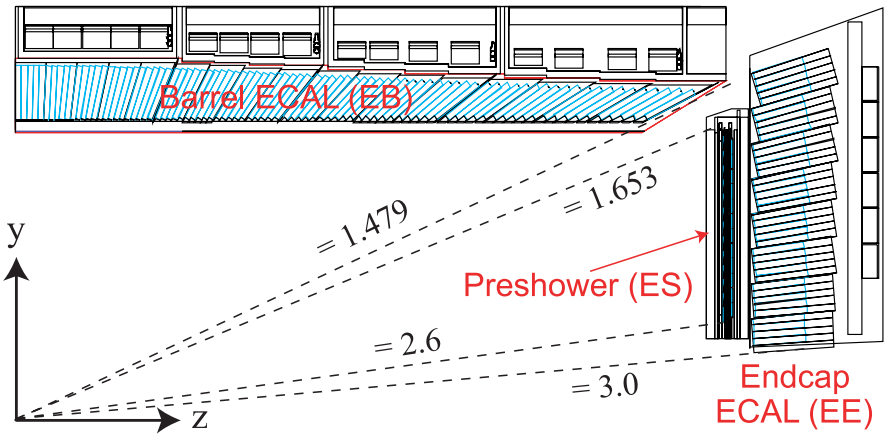

Figure 3.7: Layout of one quarter of electromagnetic calorimeter in the r-z projection [22].

crystals are fast detectors emitting 80% of the light in the first 25 ns.
The endcap regions are equipped with preshower detectors which consists of lead shower material and silicon detectors. The preshower detectors allow to determine the spatial position of photons more precisely, in oder to separate photon stemming from mesons and single photons.
The energy resolution of the calorimeter can be parametrized as:

$$\left(\frac{\sigma}{E}\right)^2 = \left(\frac{S}{\sqrt{E}}\right)^2 + \left(\frac{N}{E}\right)^2 + C^2, \tag{3.2}$$

where S is the stochastic term, N the noise and C the constant term [21]. Figure 3.8 (left) shows a fit of the function the measurements obtained in a beam test. A relative error of $\sim$0.5% was achieved at an energy of 100 GeV. In addition, the high spatial granuality allows to seperate a cluster in the particle dense envirement of CMS.

3.3 Hadronic Calorimeter

The hadron calorimeter [23] (HCAL) design was strongly influenced by the decision to place the calorimeter inside the coil, leading to little space for the detector. It is built in a classical sandwich like structure with brass as absorber material and plastic scintillator with wavelength-shifting fibers. Scintillators behind the coil of the magnet built the Hadron Outer(HO) detectors and effectively increase the calorimeter thickness to 10 interaction lengths. The HCAL splits into the Hadron Barrel (HB, $|\eta|$ <1.4) and the Hadron Endcap (HE, 1.4 < $|\eta|$ <3.0). The Hadron Forward (HF) covers the $|\eta|$ region between 3 and 5 and is built of a steel absorber and fiber which point to the interaction point. It is placed in $\pm$ 11 m in z. The large η ensures to collect most transverse energy in order to determine the missing transverse energy which

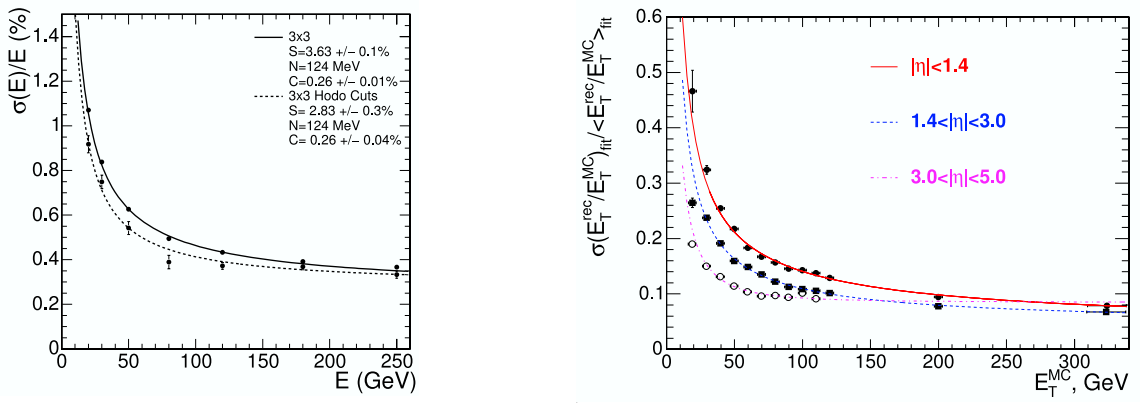

Figure 3.8: Left: Relative energy resolution of the ECAL as a function of the energy. Function 3.2 has been fitted to the data points. Right: Relative transverse energy resolution of the HB ($|\eta| < 1.4$), the HE ($1.4 < |\eta| < 3.0$), and the HF ($3.0 < |\eta| < 5.0$) as a function of the transverse energy.

is especially interesting in searches for R-parity conserving SUSY, since the lightest "sparticle" would leave the detector without interactions, if uncharged. The transverse energy resolution of the different hadron calorimeters is presented in figure 3.8.

3.4 Muon System

The muon system is built in a sandwich like structure with absorber material, which serves as the return yoke of the magnet, and gaseous detectors used to measure and identify the muons [24]. The concept is similar to previously built muon chambers, like for example the H1 muon chambers. The muon flux, the neutron radiation, and magnetic field properties vary with η. This leads to different technology decisions for the barrel and endcap region.

The barrel region has four layers of Drift Tube Chambers (DT). Each chamber has a resolution of about 100 μm in rϕ and of 1 mrad in ϕ.

The endcaps are equipped with Cathode Strip Chambers (CSC), each CSC having a spatial resolution of typically 200 μm (100 μm for first layer) and an angular resolution of rϕ of 10 mrad. In addition Resistive Plate Chambers (RPC) cover a —η—-region up to 1.6. The RPCs are very fast but less precise detectors and are predominately intended to be used for trigger purposes. A schematic overview of the muon system is given in figure 3.9.

The most important measurement for a standalone (no tracker information) determination of the transverse momentum is the direction of flight behind the magnet coil. This vector in combination with a beam spot constraint dominates the standalone transverse momentum measurement precision. However, for muons with less than 200 GeV, multiple scattering does not allow to propagate the muon track from chambers to the beam spot with sufficient precision. Up to 100 GeV the transverse

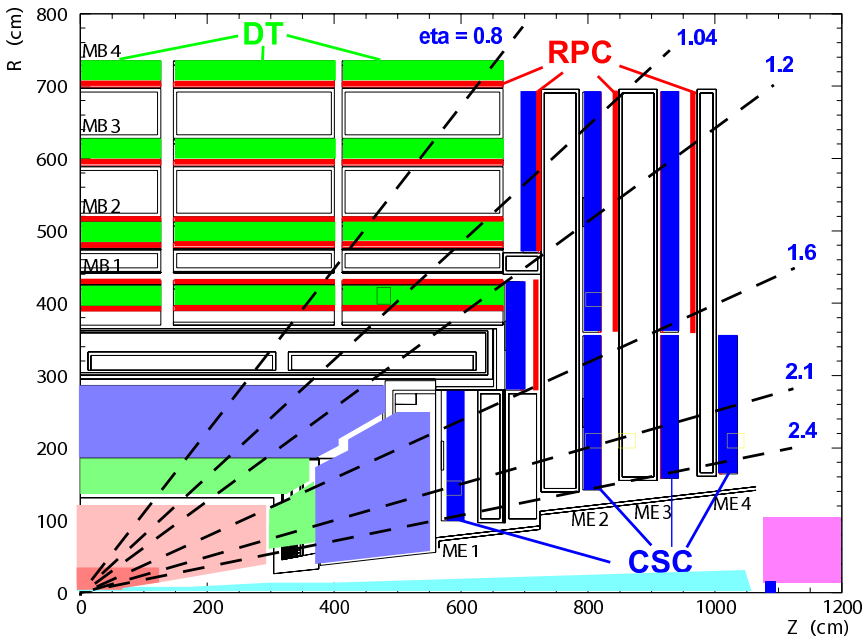

Figure 3.9: Layout of one quarter of the CMS muon system for initial low luminosity ($\sim 10^{33}\mathrm{s}^{-1}$) phase [2] in the r-z projection.

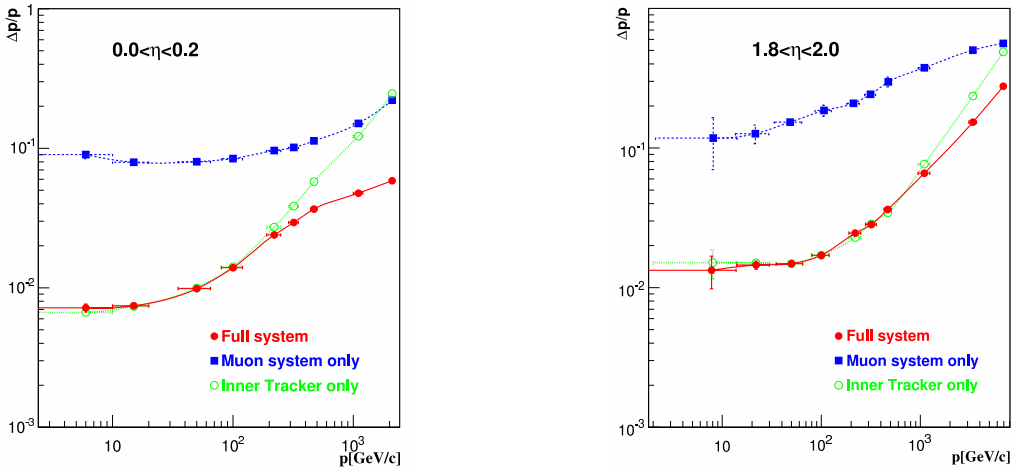

Figure 3.10: Relative transverse momentum resolution of muons as function of the transverse momentum, using measurements of the muon system only, the tracker only or both detectors. Left: Central region $0 < \eta < 0.2$. Right: Forward endcap region $1.8 < \eta < 2.0$.

momentum measurement does not even improve by adding muon chamber hits to the inner tracker detector hits. For very large momenta the muon chambers effectively improve the muon momentum measurement, as can be seen in figure 3.10 (left) for the barrel region and in figure 3.10 (right) for the endcap region.

Chapter 4

Test of Irradiated Modules

The high nominal luminosity at the LHC of 10^{34} cm^{-2}s^{-1} and high energies of 7 TeV per proton lead to an extreme radiation environment for the tracker modules. To investigate the changes of their performance during the course of the experiment is of vital importance. In a test beam at DESY the performance of irradiated modules was tested. The modules were irradiated to a level comparable to the expected dose after 10 years of LHC. The complete modules with the final readout electronics were irradiated with protons at the Forschungszentrum Karlsruhe.
Before the actual measurements are described, a brief introduction to silicon sensors and irradiation damage is given.

4.1 Working Principle of Silicon Sensors

Silicon sensors are composed of differently doped material layers within the same silicon bulk. The silicon bulk consist of a p-type and a n-type part (pn-junction). In the vicinity of the border between p-type and n-type material, the loosely bounded electrons of the donors diffuse into the p-type material and can combine with the holes of acceptors. Holes diffuse from the p-type to the n-type. Thus a certain space is depleted of free charge carriers. The electrons diffusing to the p-type and the holes diffusing to the n-type, lead to non zero space charges, hence an electric field builds up. An schematic illustration of this process is given in figure 4.1. This electric field can be increased by applying an external bias voltage with the same polarity as the initial potential. The required voltage V_{depl} to deplete a whole sensor is:

$$V_{depl} = \frac{ed^2}{2\epsilon_{Si}\epsilon_0}|N_{eff}|, \tag{4.1}$$

where $|N_{eff}|$ is the effective doping concentration, ϵ_{Si} dielectric constant of silicon, ϵ_0 the permittivity of vacuum, e the electron charge, and d the thickness of the sensor. Charged particles transversing the silicon bulk produce electron-hole pairs by ionization. These charge carriers start drifting through the material due to the electric field thus leading to a small current which can be measured. In the case of CMS, the p-type

material is separated in strips or pixels, allowing to resolve the spatial position of the induced charges.

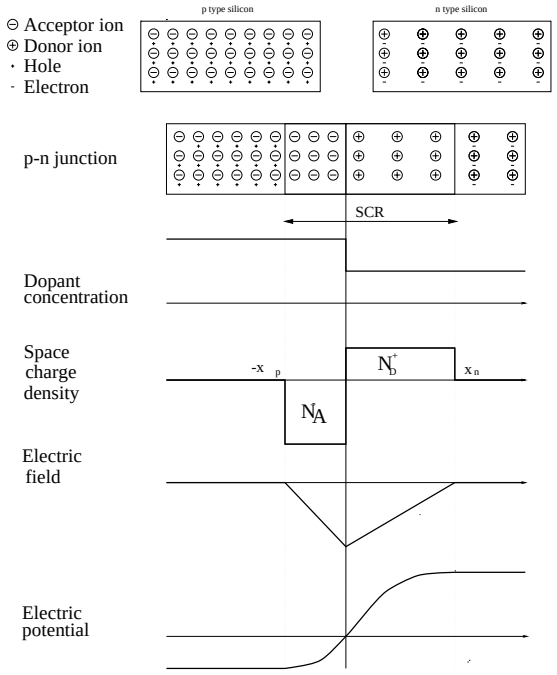

Figure 4.1: Illustration of the basic processes at a pn-junction [25]. Illustrated are the doping concentration, the space charge density, the electric field and the electric potential.

4.2 Irradiation Damage

A high energy particle transversing the silicon can displace an atom in the lattice. A vacancy and an interstitial are produced (*Frenkel pair*) which both can combine with impurities of the silicon bulk, thus forming defects. The displaced atom can be energetic and loose its energy along the path by ionization and further displacements of atoms. In this case dense agglomerates of defects are produced. The silicon bulk damage will be the dominating source for the degradation of the silicon sensors performance at the LHC.
The macroscopic effects are a change of the effective doping concentration, an increase of the leakage current and a degradation of the charge collection efficiency.

Depletion Voltage: Typically donors are deactivated by radiation induced vacancies while new deep acceptor levels are produced. This changes the effective doping

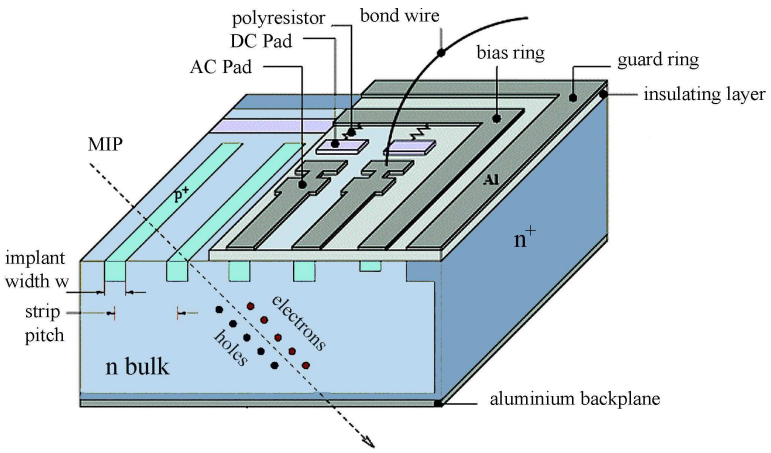

Figure 4.2: Schematic illustration of the design of a CMS sensor.

concentration. For the n-type bulk sensors of CMS, this leads to a type inversion. The depletion voltage is proportional to the absolute value of the effective doping concentration (equation 4.1) and hence the voltage is dependent on the irradiation fluence as shown in figure 4.3 for the CMS modules.
Even if not further irradiated, the effective doping changes with time t due to thermal effects (annealing). This change ΔN_{eff} can be split into three parts:

$$\Delta N_{eff}(\Phi, t) = N_A(\Phi, t) + N_Y(\Phi, t) + N_C(\Phi), \tag{4.2}$$

where Φ is the radiation fluence and $N_A(N\Phi_{eq}, t)$ is the "beneficial annealing" which increases the effective negative doping. It is also called "short term" annealing and $N_A(\Phi_{eq}, t)$ decreases exponentially with time. $N_Y(\Phi_{eq}, t)$ is called reverse annealing and increases the positive doping concentration on the long term. $N_C(\Phi_{eq})$ is the stable damage. The annealing can be suppressed by cooling.

Leakage Current: Defect levels generated by radiation can emit electrons and wholes leading to free carries in the depleted region and hence a current. The leakage current can be reduced by decreasing the operation temperature of the sensor.

Charge Trapping: Defect level can trap the drift charges leading to a state with a short lifetime. Since the lifetime is much longer than the readout time of the electronics (25 ns) for the CMS detectors, the charge collection efficiency is decreased.

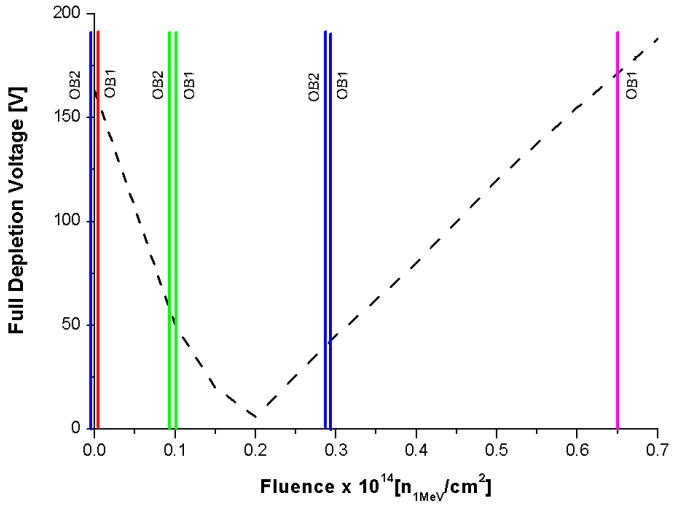

Figure 4.3: Depletion voltage as a function of the fluence. The lines indicate the irradiation doses of the tested modules.

4.3 Irradiation Doses

Two distinct sources are mainly contributing to the radiation. First, the secondaries from the *pp* collisions or particles of their decay, as well as further particles due to material interaction. This dose decreases with $\frac{1}{r^2}$. The charged hadron fluence is generally largely dominated by this source. Secondly, there are albedo particles of the electromagnetic calorimeter. They are the most intense source of neutrons. The albedo particle fluence is z dependent, since the endcaps of the electromagnetic calorimeter will be a major source of radiation. The dependence on z and r of the radiation doses, as well as an estimate of the dose are shown in figure 4.4. A dedicated radiation dose estimate can be found in the appendix of the Tracker TDR [14].

The irradiation dose for the outer barrel after 10 years of LHC is around 0.4 $\times 10^{13}$ N.E. cm^{-2}, where the unit Neutron Equivalent (N.E.) cm^{-2} is chosen such that it corresponds to a fluence of neutrons with an energy of 1 MeV. At a radius of 41 cm the dose due to fast hadrons is 6.22×10^{13} N.E. cm^{-2}, which is close to the irradiation of the tested OB1 module of 6.5×10^{13} N.E. cm^{-2} [14]. At 58 cm the expected dose after 10 years is 3.5×10^{13} N.E. cm^{-2}. The other doses for the test modules were chosen such that they are shortly before and after the inversion of the sensor material, as can be seen in figure 4.3.

The irradiation doses of the tested modules as well as the most important sensor parameters are listed in table 4.1. After irradiation in Karlsruhe the sensors were annealed for 80 minutes at 60°C and then stored in a freezer to avoid reverse annealing. The sensors were manufactured by ST Microelectronics [27], except one W5 sensor,

type	pitch μm	thickness μm	doses N.E. cm^{-2}			
OB1	183	500	0	1×10^{13}	2.9×10^{13}	6.5×10^{13}
OB2	122	500	0	1×10^{13}	2.8×10^{13}	
W5H	126-156	500	0			
W5S	126-156	500	0			

Table 4.1: Irradiation doses and parameters [26] of tested sensors.

which was produced by Hamamatsu Photonics [28]. Effects of ionizing irradiation on the readout have previously been studied [29] and shown to be a non-critical subject.

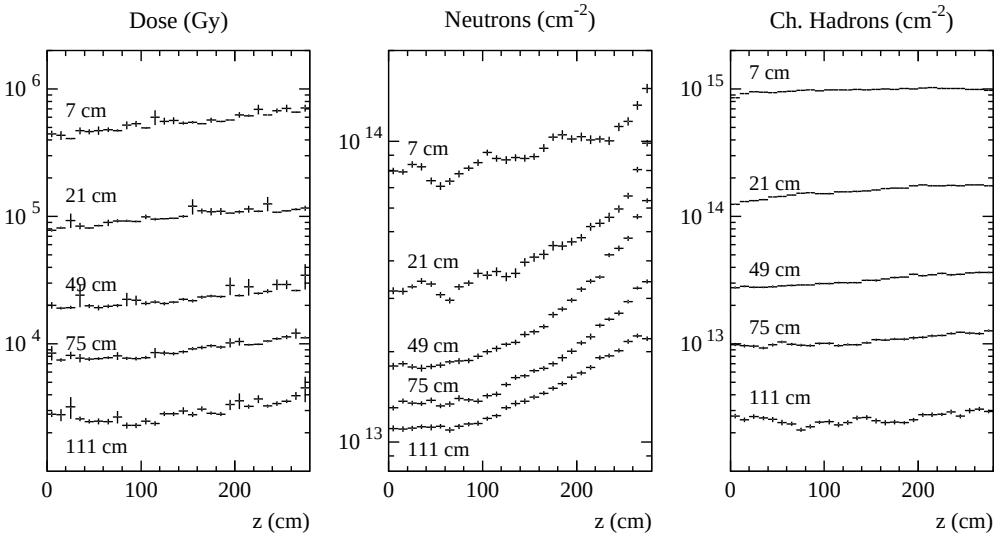

Figure 4.4: Radiation levels for different radii [14]. All values correspond to an integrated Luminosity of 5×10^5 pb^{-1} (expected integrated luminosity after 10 years). The error bars indicate only the simulation statistics.

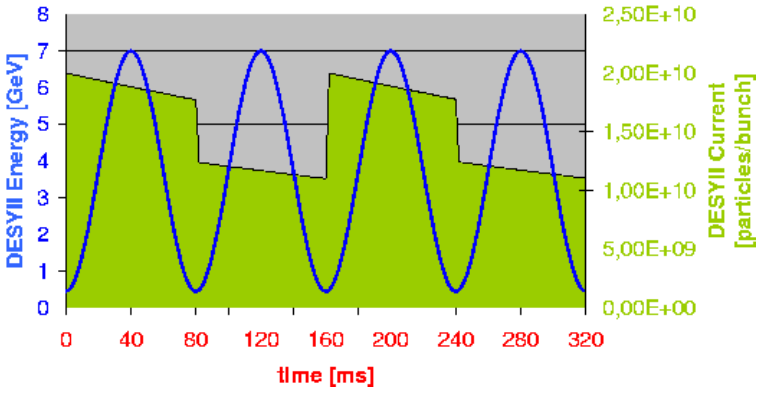

Figure 4.5: DESY II beam energy and current as a function of time.

4.4 Test Beam Setup

The setup at the test stand at the electron beam included a trigger system, a telescope for tracking, a cooling box for the tested module, and a xy-table to precisely move the module.

Electron Beam: Beam line 22 of the DESYII electron/positron synchrotron was used for the test beam. DESYII accelerates and decelerates one bunch of 2 $\times 10^{10}$ electrons or 6 $\times 10^{9}$ positrons in sinusoidal mode with a frequency of 12.5 Hz (= 80 ms period) from 450 MeV up to 7 GeV, as shown in figure 4.5. The revolution frequency is 1 MHz and the bunch length is around 30 ps [30]. The 1 MHz frequency of one acceleration cycle is not synchronized to the next acceleration cycle. Therefore, every 80 ms the phase of the 1 MHz frequency is shifted. Also every 80 ms the synchrotron can be refilled with bunches by a linear accelerator. The beam for the beam line 22 is generated via bremsstrahlung. A 10 μm thick carbon fiber in the circulating beam serves as target. The photons are converted to electron/positron pairs with a metal plate. Then the beam is spread out into a horizontal fan with a dipole magnet. The final beam is cut out of this fan with a collimator. The magnetic field can be varied to select the energy of the electrons passing the collimator. A schematic overview is given in figure 4.6.

Telescope: A precision telescope [31] to reconstruct the tracks of the test beam electrons and an according trigger are available for beam line 22 (figure 4.7). The telescope was originally installed to test the Micro-Vertex-Detector (MVD) sensors of the ZEUS experiment [32]. The telescope consist of three planes. Each plane is composed of two orthogonally mounted silicon strip sensors. Each sensor has an active area of 32$\times$32 mm^2. The strip pitch is 25 μm, only every other strip is read out via AC coupling. The distance between the sensors is 2 mm and the thickness of each sensor is 300 μm. The intrinsic spatial resolution of the sensors had been determined to be

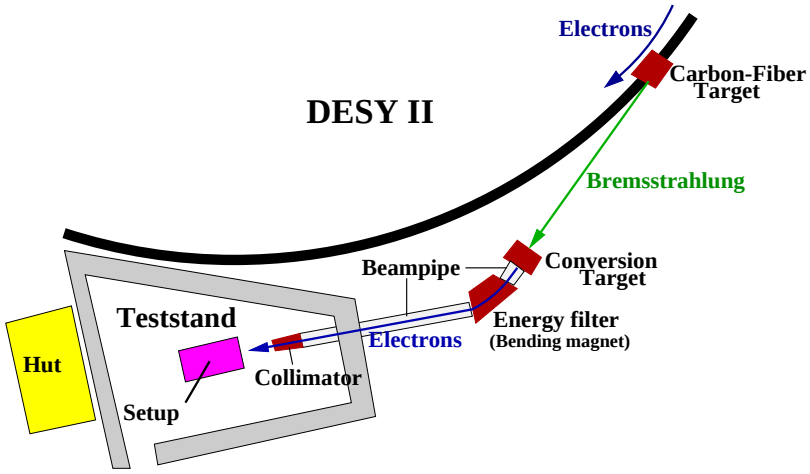

Figure 4.6: Overview of DESY II test beam area.

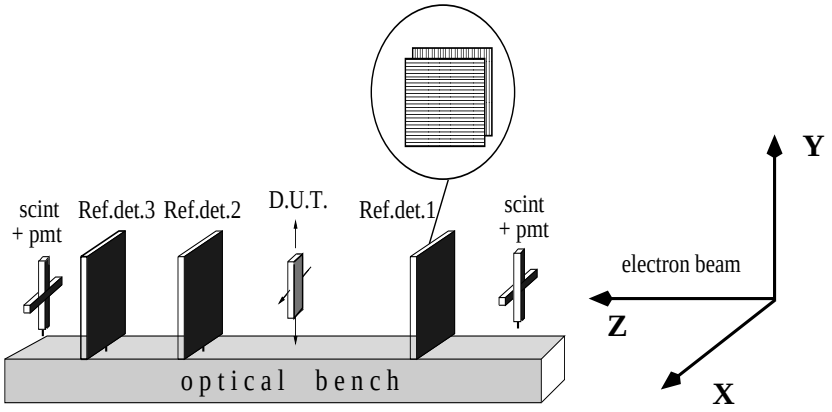

Figure 4.7: Schematic layout of the telescope.

~ 3 μm [33]. The dominating effect degrading the resolution of the expected impact position on the device under test is multiple scattering. The state of the telescope at the time of the test beam was investigated in cooperation with the preceding test beam user. The telescope turned out to be properly working [25].

Cooling System: The operating temperature at the LHC will be about -15° C. Furthermore the irradiated sensors have very strong leakage currents at room temperature and cannot be operated. A cooling system allowed to operate the tested sensors at low temperatures. A Lauda Klein Kryomat cooling machine could refrigerate the cooling liquid down to -65° C. A Temperature sensor (PT 100) was attached centrally to the sensors material via a small plastic clamp. The sensors were mounted on a

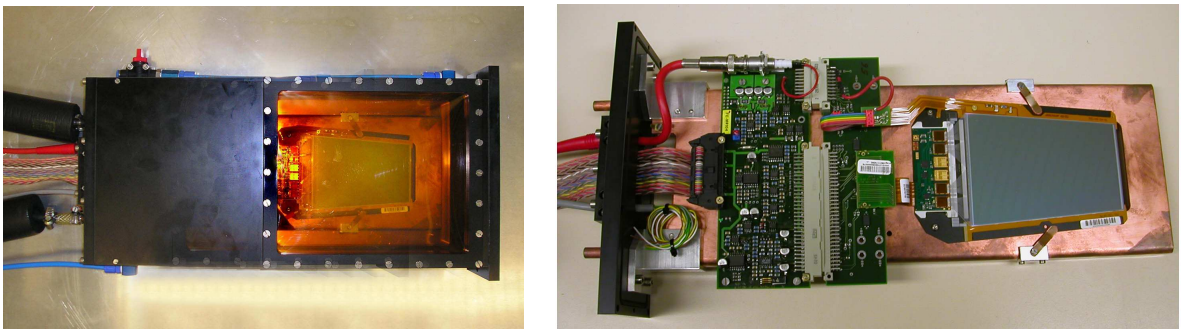

Figure 4.8: Left: The cooling box with the supply cables and pipes. Right: Copper inlet of the cooling box with a mounted module and readout electronics.

copper plate within a box (figure 4.8). The copper plate was connected with the cooling coil. A cooling liquid temperature of about -35° C was required to cool the sensor material to -15° C. The copper behind the sensor was left out in order to reduce multiple scattering. The box had windows with 100 μm kapton foils for the electron beam. In addition the kapton foil was covered with a light-proof black foil during operation. The box was flooded with nitrogen to avoid the formation of ice crystals. A relative humidity of below 7 % was acieved during operation.

XY Table: The CMS modules could be precisely moved and rotated during test beam operation. The cooling box was mounted on a XY table and could therefore be moved in the directions transverse to the electron beam. The XY table consists of two orthogonally mounted M505 [34] linear position systems. The precision of the translation is 1 μm per 10 cm. The cooling box could also be rotated to a precision below 1×10^{-3} radian. The rotation axis was parallel to the strips of the CMS modules, allowing to change the inclination angle of the electrons with respect to the precisely measuring coordinate of the sensors. The rotation plate and the XY table are shown in figure 4.9. A solid flange was built in order to attach the cooling box to the rotation motor.

Trigger: The trigger consists of two scintillator layers, one in front of the first telescope plane and the other behind the last telescope layer (figure 4.7,4.9). Each scintillator plane has two orthogonally mounted scintillator strips with a width of 9 mm each. The triggered beam width is therefore 9 mm in both transverse directions, which is smaller than the beam size. This did not reduce the trigger rate, since the rate is dominated by the dead-time of the CMS module readout.

4.5 Data Acquisition

The tested modules were equipped with the final Analogue Pipeline Voltage (APV)[35] readout chip. In contrast to the final LHC operation, the chip was read out via the

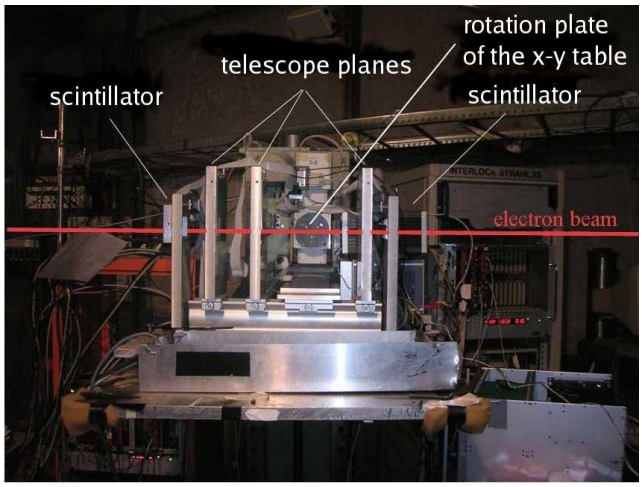

Figure 4.9: Picture of test beam setup.

APV Readout Controller (ARC) board [36]. The trigger and the external clock for the APV had to be adapted to the test beam.

Test Sensor Readout: The APV readout chip was directly connected to the APV Readout Controller (ARC) board via a 1m long shielded twisted pair broad band cable. The ARC board was developed for quality assurance of the CMS modules [37]. The ARC Software (ARCS) is Labview based and has its advantages in easy usability and online visualization of the taken data. ARCS also interfaces a high voltage board, which supplies the modules with the bias voltage. The voltage can be varied from 0 V to 600 V and also the leakage current can be monitored. The leakage currents resolution varies with the leakage current and is 0.25/2.5/25 nA for 10/100/1000 μA, respectively. The APV operates with 40 MHz frequency, which is predetermined by the bunch crossing frequency at LHC. The ARC system usually supplies the APV with an ARC internal clock. An ARC external clock can also be given to the APV via the ARC board. This is needed to synchronize the APV clock with the DESYII machine clock. The ARC software generally can be used to take data, since it is able to write an ASCII file with all relevant readout information, namely the header and the digitalized measurement of each strip. The Analogue Digital Converter (ADC) of the ARC system has half of the granularity of the readout system intended to be used at LHC operation. In a private version of ARCS, a time stamp with a granularity of one ms was added to each measurement in the raw data ASCII file. This was added to crosscheck the merging procedure of telescope and CMS module data. The ARC board can be fed with a trigger and produces a busy signal, allowing to halt data taking until the ARC board is able to take new data. Unfortunately, the Labview based ARCS is much slower than the board and the busy signal had to be stretched to 70 ms via a delay module. Still sporadic cases occurred, where the ARC system

was not yet ready to take new data after these 70 ms. The beam structure leads to a train of filled bunches of a certain energy every 80 ms. Only every 160 ms the beam is refilled, yielding the maximum current (figure 4.5). To trigger several events within 80 ms, the dead time would have to be reduced to the order of μs. The maximum event rate was 12.5 Hz. Depending on the beam quality, the trigger rate typically varied between 5 and 10 Hz.

Telescope Readout: The same readout system of the telescope was used as for previous test beams [33, 25]. A time stamp for each event was added to the raw data, allowing to check the offline merging procedure of the two separate data streams, the test module and the telescope modules data streams, respectively.

DESYII and APV Clock Synchronization: The high bunch crossing rate at LHC requires a time resolution of 25 ns for the CMS modules to suppress signals of the previous bunch crossings. This sets tight demands on the synchronization of the DESYII clock and the clock given to the APV. An offset of a few ns would rapidly decrease the signal.
Two different readout options are available for the modules.

- The peak mode simply reads the height of the amplified and shaped signal at a certain time offset from the trigger. Its time resolution is around 50 ns. The pulse seen is a convolution of the detector signal and the response function $h(t)$ of the preamplifier and CR-RC shaper. For equal time constants τ ($\sim$50 ns) of the preamplifier and the shaper the response function is:

$$h(t) = \frac{t}{\tau} e^{-\frac{t}{\tau}}$$

- The deconvolution mode, however, reverses this convolution to some extent and its signal shape is closer to the original detector signal. This is needed since the high bunch crossing rate at LHC (40MHz) demands fast readout times. For this purpose three subsequent measurements of the pulse are summed up with different weights, as shown in figure 4.10. The weights are dependent on the timing constant τ and the sampling time (25 ns). The calculation shown in [38] leads to:

$$w_1 = 0.45 \quad w_2 = -1.47 \quad w_3 = 1.21$$

  The detector signal length is typically far below the sampling time of 25 ns. The effective time resolution of the deconvolution mode is 25 ns. The shapes of the signals are depicted in figure 4.11. The deconvolution mode will be default in LHC operation and was therefore chosen as default for the test beam.

The DESYII clock has a frequency of 1 MHz and every 80 ms the clock pauses and restarts with an arbitrarily shifted phase. This demanded also a new synchronization

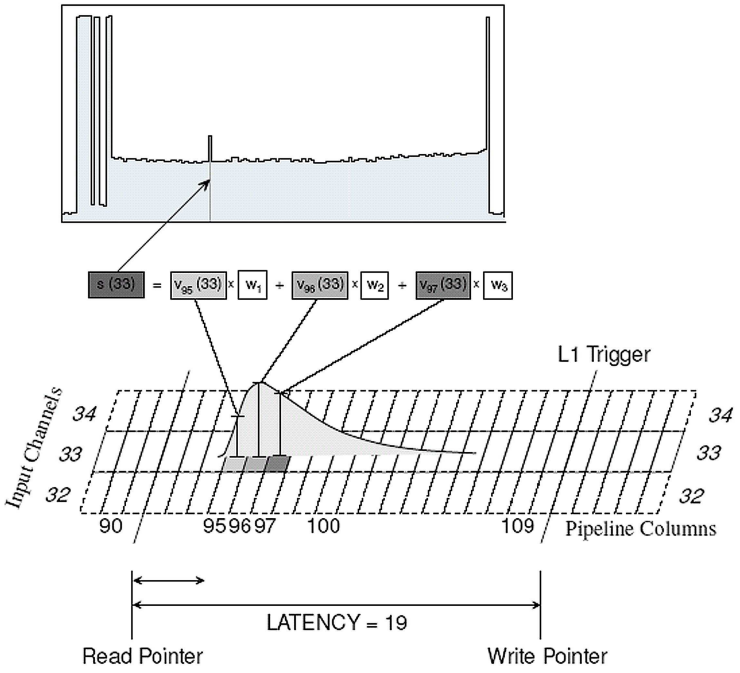

Figure 4.10: Illustration of deconvolution signal calculation and trigger latency.

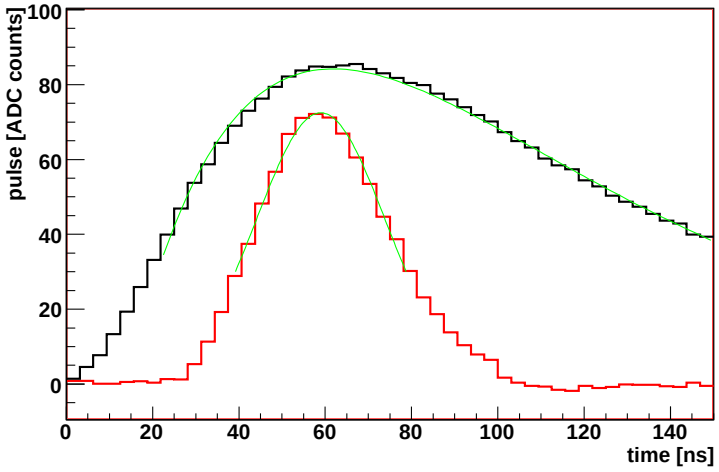

Figure 4.11: Red: deconvolution mode, Black: peak mode, Green: fits to theoretically expected pulse shape. Data from the calibration pulse recorded with the ARC system.

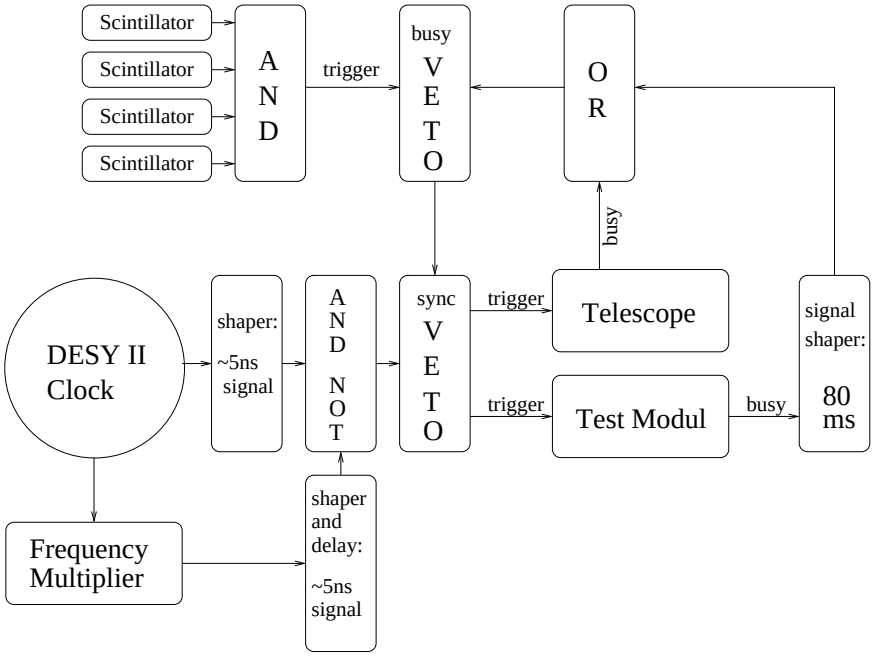

Figure 4.12: Schematic illustration of trigger logic.

of the APV clock to the DESYII clock every 80 ms. In addition the 1 MHz frequency had to be increased to the 40 MHz frequency required by the APV. For this purpose a frequency multiplier was custom built for this test beam, a demanding project, since the frequency was not allowed to fall below 38-39 MHz or rise above 41-42 MHz. The APV would fail otherwise. The synchronization worked well for most cases, however a trigger veto was introduced if the APV clock and the DESYII clock were shifted by more than 5 ns. For this purpose the clock signal was stretched to a length of 5 ns. This stretched signal was brought in coincidence with the clock for the APV. If no coincidence occurred the trigger was vetoed (figure 4.12). However, in very rare cases the clock offset was exactly 25 ns (one clock tick), causing the coincidence unit to fire.

Trigger Logic: The trigger was composed of four scintillators, as described in the previous chapter. If the scintillator signals were in coincidence, a trigger signal was given. Furthermore, there were the two vetoes described above, which could halt the trigger. The logic was based on NIM crates and is depicted in figure 4.12.

4.6 Measurements

The emphasis of the measurements was the performance of the irradiated modules at different working conditions, such as temperature and bias voltage. In addition, tests

	events	telescope	modes	parameters
Latency Scan	3×10^3	no	peak & dec	default
Pedestal Run	10×10^3	no	peak & dec	no beam
Voltage Scan	5×10^3	no	peak dec	450 V 50, 100, 200, 300, 550 [V] knee in 50 V steps
Temperature Scan	5×10^3	no	peak & dec	-10°C, -15°C, -20°C
Energy Scan	10×10^3	yes	peak dec	3, 6 [GeV] 1.6, 3, 4.6, 6 [GeV]
Angle Scan	10×10^3	yes	peak dec	20°, 40°, 60° 10°, 20°, 30°, 40°, 50°, 60°, -40°, -60°
XY Scan	$20\text{-}50 \times 10^3$	yes	peak	Pos 1,2,3,4,5

Table 4.2: The test beam program. Default parameters are 450 V bias voltage and 6 GeV beam electron energy. For a description of the XY scan position see figure 4.13.

of edge effects were performed for some modules. Different energies and inclination angles are used to study different of cluster algorithms for the hit position determination. The different measurements are listed in table 4.2. The default bias voltage was chosen to be 450 V. A lower voltage would lead to a slightly broader spread of the induced charges and hence a higher probability of charge charing between strips, which would be beneficial to the resolution. However, the rather high voltage has been chosen to ensure depletion also for irradiated modules. 450 V is significantly higher than the expected depletion voltage, even for the maximally irradiated module.

Latency Scan The time difference between the trigger signal and the module signal had to be determined to gain the optimal signal to noise ratio (figure 4.10). The latency was scanned first in 25 ns steps, by reading out different buffers of the pipeline, which stores the hit information for 4.8 μs. In addition the phase of the Phase Look Loop (PLL) of the APV chip electronics could be adjusted in ∼ns steps [35], effectively resulting in a 1 ns granularity of the latency scan. A simple algorithm was used to evaluated the signal height for the different time settings.

Pedestal Run The pedestal run was performed without beam electrons. The internal ARC trigger was used. An algorithm running on the raw data produced control plots, testing the basic properties, namely if pedestals, noise and the common mode corrected noise seemed reasonable. The dataset produced can also be used for the evaluation of the pedestals and noise in the offline analysis, with the advantage of the absence of signals.

Voltage Scan The modules were tested with different bias voltages. The scan is done in 100 V steps and in 50 V steps in the vicinity of the depletion voltage. The maximal applicable bias voltage will be 550 V with the power supplies provided for LHC operation.

Temperature Scan The leakage current increases with irradiation and decreases exponentially with temperature. The irradiated modules can only be operated if cooled. Their performance was tested for temperatures of -10° C, -15° C and -20° C.

Energy Scan The energy scan was conceived to be used for resolution studies, making use also of the telescope. The resolution of the predicted position σ on the CMS module extrapolated from hits of the telescope detectors is dominated by multiple scattering. Measurements at different energies allow to disentangle intrinsic resolution σ_{intr} and the degrading of the resolution due to multiple scattering. The resolution degradation due to multiple scattering, σ_{ms}, is proportional to the inverse of the square of the electron energy E ($\sigma_{ms}^2 = \frac{c}{E^2}$). The residual width σ_{eff} between the extrapolated tracks and the module measurement depends on the energy as follows.

$$\sigma_{eff} = \sqrt{\sigma_{intr}^2 + \sigma_{ms}^2} = \sqrt{\sigma_{intr}^2 + \frac{c}{E^2}}$$

Angle Scan The main purpose of the angle scan is to optimize cluster algorithms for the hit position determination at large inclination angles. Therefore, the angle scan was done with combined telescope read out. The inclination angle of the electron beam with respect to the normal of the sensor was varied in 10° steps from 0° to 60° and in 20° steps from 0° to -60°. The rotation axis was parallel to the strips of the CMS sensors. The dominating uncertainty of the angle was the initial angle, which was known to 1° precision.

XY Scan The XY scan is intended to examine edge effects. The position of the beam was varied such that the edge of the sensor was illuminated at several points as shown in figure 4.13. The chosen statistics were high with up to 50k events, since edge effects are expected to occur only on a few strips close to the edge. The telescope data was read out in order to be able to study systematic shifts of the measurements at the edges. The signal performance as a function of the distance to the side which is closer to the read out electronics was studied. For modules consisting of two sensors, such as OB1 and OB2 modules, a slightly smaller signal has been found in previous test beams for hits in the far sensor with respect to the readout electronics.

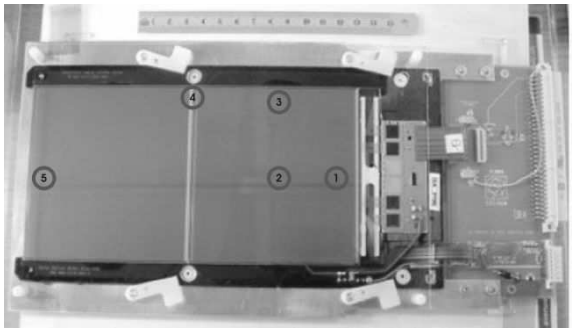

Figure 4.13: Position of the xy scan.

4.7 Data Analysis

The analysis[1] splits into three parts: the CMS module hit reconstruction, the reconstruction of the tracks in the telescope, and the merging of both.

4.7.1 CMS Module Analysis

The analysis was divided into raw data processing, including the pedestal calculation and common mode subtraction, and into more dedicated analysis like cluster recognition as well as signal to noise calculations.

Raw Data Processing

The data is analyzed to calculate the pedestal, noise and the common mode noise. In rare cases events are dismissed due to wrong headers and other peculiar features, see [41] for more details.

Pedestals The pedestal for each strip is determined by fitting a Gaussian function to the measurements accumulated during an electron run. Figure 4.14 shows the pedestal determination for an individual strip and the pedestals of all strips. A structure due to the different APVs with their 128 channels each, is clearly visible. During data taking a mixture of noise and signal measurements is expected for the strips within the area illuminated by the beam. However, this did not have a significant impact on the pedestal determination [41]. This was checked by comparing the pedestals of a dedicated pedestal run to the pedestals determined during data taking. The pedestals were slightly different, but the difference did not depend on whether a strip was within the illuminated area.

[1]The custom made ROOT[40] based software can be downloaded from http://cms-desytb04.web.cern.ch/cms-desytb04.

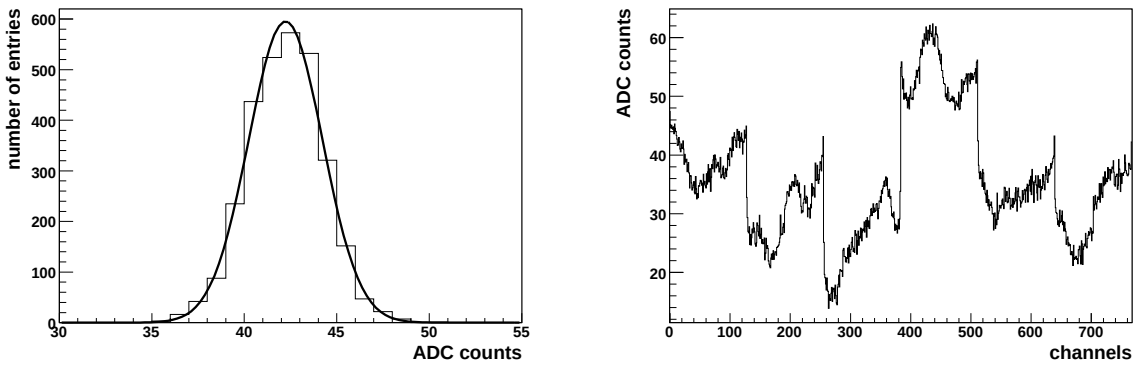

Figure 4.14: Pedestal plots. Left: Gaussian fit to an individual channel. Right: Pedestal values vs. the strip number.

Common Mode Noise The common mode noise is an additional noise component to the random noise of each individual strip. The common mode noise occurs on an event basis, mainly due to electronic pick up or slight power supply variations of the preamplifiers. The common mode noise is the average noise for a block of N neighboring strips. The analogue input to an APV is grouped in four blocks with 32 channels each. Therefore the corrections are also calculated in blocks of 32 channels. The common mode noise must be determined for each event, hence it must be insured that the signals due to electrons transversing the sensor do not effect the calculation of the common mode noise. Therefore the three largest and the three smallest ADC values of a common block are neglected for the common mode noise calculation. The common mode noise for a certain block is therefore determined by:

$$CMN = \frac{1}{N-6} \sum_{i=j}^{i=j+N} \delta(i \in min)\delta(i \in max)(ADC_{iraw} - ADC_{iped})$$

Where $\delta(i \in min)\delta(i \in max) = 0$, if i is an element of the strips with the three smallest or largest ADC counts. ADC_{iraw} and ADC_{iped} are the ADC counts of the raw data and the pedestal of strip i, respectively, and j is the strip number of the first strip of the block.

All further analysis are based on pedestal and common mode noise corrected values. Figure 4.15 (left) shows the beam profile, which is expected to as wide as the triggered beam width. The beam profile width of about 70 strips (122 μm strip pitch) translates to the 9 mm width of the trigger scintillators. In figure 4.15 (right) a typical signal is presented.
Bad channels are defined by cuts on the noise and the pedestal of a strip, they are not regarded in the following analysis. Typically less than 1% of the strips were rejected, a detailed description of the procedures can be found in [41].

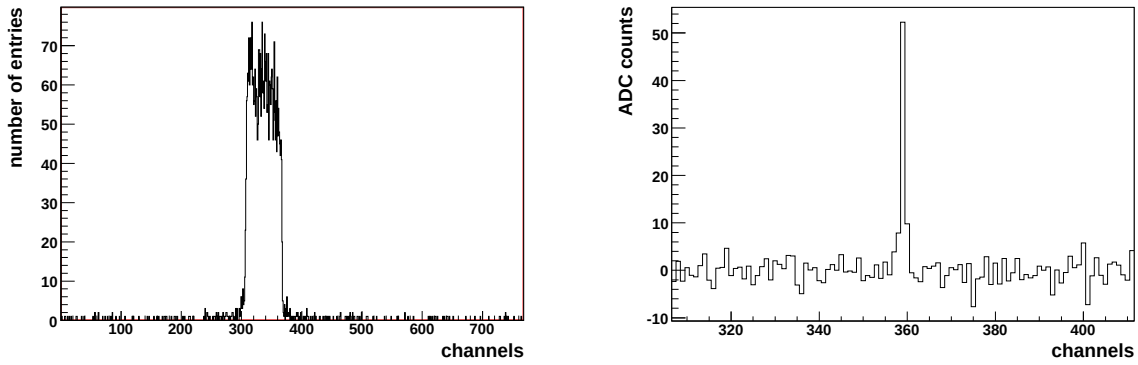

Figure 4.15: Basic control plots. Left: The beam profile. For each channel the numbers of the events, where the signal on the channel was the highest, is shown. Right: ADC counts versus the strip number for a typical signal from an electron.

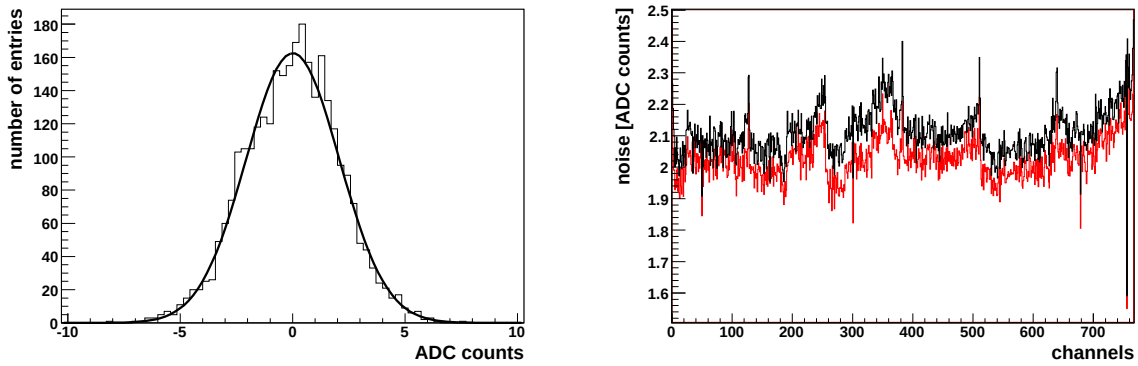

Figure 4.16: Noise plots. Left: Gaussian fit to an individual channel. Right: Initial noise (black) and common mode corrected noise (red).

Noise The noise was determined for each run, fitting the pedestal and common mode corrected ADC counts of a strip with a Gaussian function. The sigma of the Gaussian function was taken as the noise value for the strip. In figure 4.16 typical noise values are shown. The peaks, which occur every 128 channels in the noise distribution, correspond to channels close to the APV borders.
Again, the fit was not significantly effected by the occasionally occurring signal measurements, which tended to be many standard deviations away from the mean. This can be seen by comparison of the non-illuminated regions to the illuminated, as well as comparing the noise values of the pedestal runs to the runs taken with beam trigger.

Cluster Recognition The merging of single strip signals to clusters is undertaken similar to previous test beams, such as the TEC test beam 2004 [42], and to the CMS reconstruction frameworks, which are ORCA (old) [19] and CMSSW (current) [43]. Initially strips above a certain threshold are considered as candidates for seeds of a cluster. The signal to noise ratio of a seed candidate has to be above four, where the noise of the individual strip is taken for the ratio calculation. A neighboring strip is added to the cluster if its signal to noise ratio is above three. The sum of the signals of a cluster divided by the quadratic sum of the individual noise-values defines the signal to noise ratio. A cluster is required to have at least a signal to noise ratio of five. These definitions have been chosen in order to be consistent with CMSSW. The previous measurement and the default reconstruction in ORCA used cuts of three for the seed and two for the neighboring strips. A typical distribution of the number of strips per cluster is shown in figure 4.17.

Signal and Noise The signal to noise ratio is fitted with a convolution of a Landau-function with a Gauss-function. The most probable value of this fit is called the signal to noise ratio in the following. The fit was performed over a limited range. Ghost-hits and hits with small signals due to wrong timing contribute to a peak at small values of the distribution and should be neglected. The fit range was set from 0.3 to 0.65 $\times$ the signal to noise ratios mean. A typical fit is illustrated in figure 4.17. The average signal was determined likewise. The values were determined for the strips of each individual APV as well as for the whole sensor. In principle the gain of different APVs could be different, but the APV dependence turned out to be marginal and all strips were used for the following plots.

Inter-Strip-Coupling Inter-strip-coupling causes signals on the neighboring strips of a centrally hit strip. The strips are coupled via their capacity. In addition the signal is not proportional to the amplitude of the signal in deconvolution mode, but also sensitive to the shape of the signal, leading effectively to an increase of the inter-strip-coupling. Inter-strip-coupling is an important parameter in simulations and should also increase with radiation damage. This is due to the charge trapping, which increases with radiation. Generally charges are induced on the neighboring strips, as soon as the electrons and holes start drifting in the sensor material. These charges on

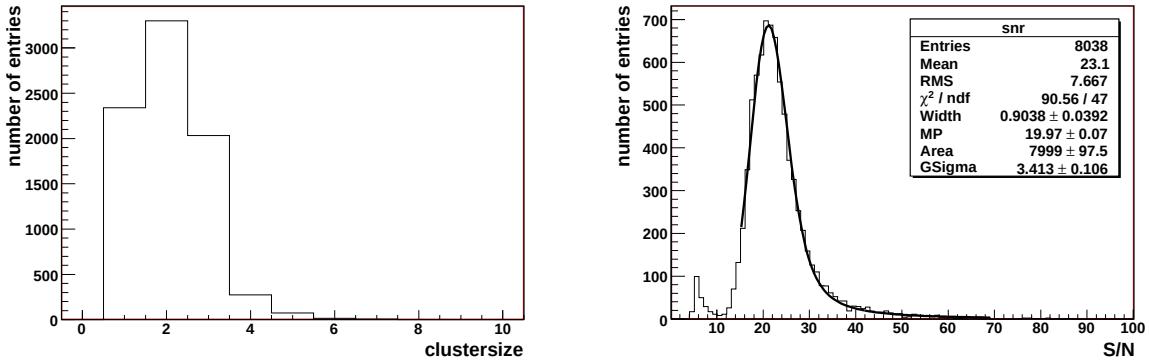

Figure 4.17: Cluster size and signal to noise ratio of clusters. Left: Number of strips per cluster. Right: Landau ⊗ Gauss convoluted fit to signal to noise ration.

the neighboring strips compensate the electric field produced by the drifting charges. The remaining charge after the electrons and holes have drifted out of the n-type material is naturally zero again. If drifting charges are trapped, this would lead to a remaining net charge on the neighboring strips and therefore to an increased signal. For the determination of the inter-strip-coupling the fact, that the charges produced by the ionizing particles only spread very locally, is used. The spread of the induced charge due to diffusion is in the order of a few μm, while the distance between strips are of the order of 100 μm. Therefore the spread of the drifting charges to both neighboring strips is largely suppressed, if the flight direction of a ionizing particle is perpendicular to the sensor. If both neighboring strips measure similar signals this can therefore be interpreted as purely due to cross talk between the strips. Figure 4.18 shows the sum of both neighboring strips signals and the difference of the neighboring strips signals divided by the total signal in a two dimensional plot. Even if the signals of the neighbors are equal they are not close to zero which leads to the conclusion that coupling occurs. The sum of the neighboring strip signals clearly shows a peak (figure 4.18). The mean of the peak represents the average ratio of the signal due to inter-strip-coupling and the total signal. A fitting procedure determines the mean and the width of this peak. A Gauss function is fitted to the distribution, ranging from -0.1 below the highest bin to 0.1 above it. The result of the fit is the ratio between the signal collected via inter-strip-coupling on the neighboring strips and the total signal.

Hit Position For the hit reconstruction the same algorithm was implemented as is used in ORCA for clusters with less than 4 strips. The hit position r is determined as follows:

$$r = \left(i + \frac{w_r - w_l}{w_l + w_r + w_c} \right) p$$

where w_l, w_c, and w_r are the measurements of the left neighbor, the seed and the right neighbor strip. If neighboring strips are below the threshold, they are set to zero. i

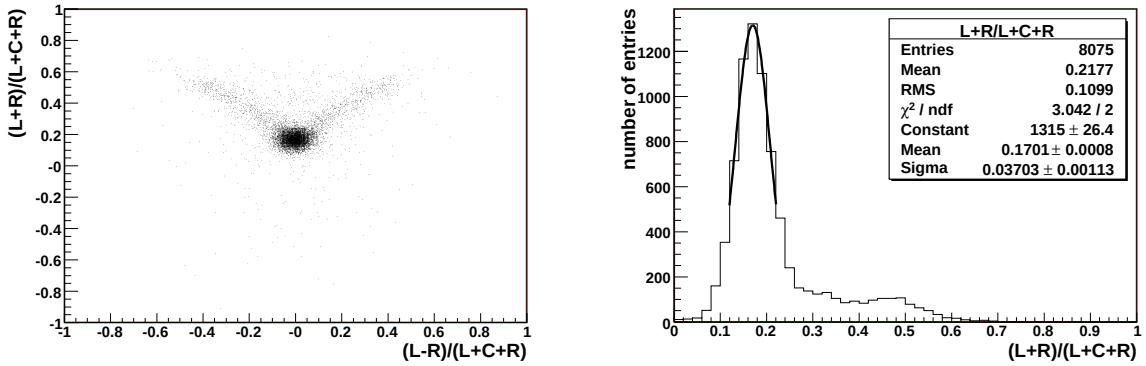

Figure 4.18: Inter-strip-coupling, Left: ADC counts of neighboring strips to cluster ADC counts ratio vs. difference of ADC counts of neighboring strips to cluster ADC counts ratio. Right: Fit of Gaussian function within a limited range of the ADC counts of neighboring strips to cluster ADC counts ratio. The right illustration is also the projection of the left illustration to the y-axis.

is the strip number of the seed and p the strip pitch. Different dedicated algorithms will be studied in [44].

4.7.2 Combined Analysis

The combined analysis also incorporates the telescope measurements. For track reconstruction in the telescope a separate software (TELA) has been developed in cooperation with the previous test beam user and is described in [25]. In addition, a framework to merge the data and reconstruct full tracks was developed (see appendix B).
In a few cases events in the CMS module data are missing, therefore merging of the data is a rather tedious procedure. Timing information and geometric matching of the tracks measured with the telescope have been used in addition. By comparing the predicted hit position from the track and the measured position it is shown that compliance is achieved (figure 4.19). However the reconstruction and merging procedures are not sufficiently automatized to be applied to all data and further development of the analysis utilizing the track information are ongoing and will be published in [44].

4.7.3 Error Estimation

The test beam especially focuses on the dependence of module properties on the irradiation levels. Correlated errors shifting all measured values are therefore of less concern than uncorrelated errors.

Uncorrelated Errors The fits which determine the measurement values have statistical uncertainties which are plotted as errors in the following plots. Nevertheless

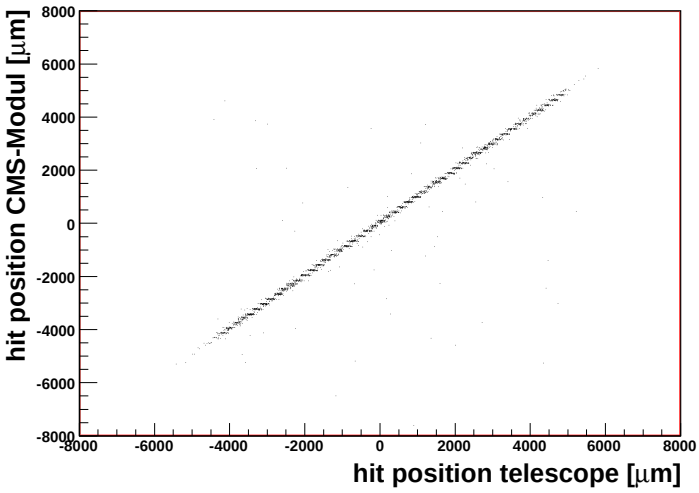

Figure 4.19: Matching of telescope and CMS module data. Predicted hit position of the telescope vs. hit measurement of the CMS module.

other errors could influence the measurements. Especially the temperature does affect the measured values, as can be seen in figure 4.23. This results in an additional error of the size of the fit uncertainty. The uncorrelated errors can also be estimated by independently remeasuring several times. This effectively happens when the energy scan is done, since the energy deposition is close to constant for electrons within an energy range of 1.6 GeV to 6 GeV. Also the known increase of the collected charge with different angles can be used to crosscheck the error estimates. The χ^2/ndof of the according fits (figure 4.24 and 4.25) suggest that the purely statistical error estimates are reasonable. Still, additional uncorrelated errors can be concluded to be of the order of the statistical error.

Correlated Errors The fitted values can depend on the chosen fit range. Therefore the fit range was varied and effects on the results studied, as can be seen in table 4.3. The fit turned out to be very stable with respect to the range. Different cuts for the cluster definition vary the absolute results significantly. Obviously the signal decreases if the cut for the neighboring strips is increased. The signal to noise ratio generally increases if the neighboring strip cut is increased. This is due to the noise calculation, which quadratically adds the noises of the cluster strips. Adding a new strip therefore increases the noise. Table 4.4 shows the absolute changes for a OB1 module and also the ratio of the non-irradiated OB1 module to the maximally irradiated module. Although the absolute value of the signal and signal to noise ratio is therefore dependent of the cluster definition, the ratio of the measurements of different modules is constant to the % level which is an order of magnitude smaller than the effects expected due to irradiation.

S/N	upper limit [× mean S/N]	lower limit [× mean S/N]
21.13 ± 0.09	0.7	0.3
21.19 ± 0.08	0.6	0.3
21.17 ± 0.08	0.65	0.3
21.10 ± 0.10	0.65	0.25
21.18 ± 0.08	0.65	0.35

Table 4.3: Sensitivity of signal to noise ratio to the fit range.

	S/N ratio	signal ratio	cuts [σ]: neighbor, seed, cluster
$OB1_{2,3,5}/OB1_{3,4,5}$	1.11	0.93	2,3,5/3,4,5
$OB1_{2,3,5}/OB1_{4,5,5}$	1.23	0.84	2,3,5/4,5,5
$OB1_{\text{not irrad.}}/OB1_{\text{irrad.}}$	1.11	1.13	4,5,5
$OB1_{\text{not irrad.}}/OB1_{\text{irrad.}}$	1.10	1.15	3,4,5
$OB1_{\text{not irrad.}}/OB1_{\text{irrad.}}$	1.11	1.19	2,3,5

Table 4.4: In the first two columns the ratios between the values obtained with different cluster cuts are listed using the same not irradiated module. The latter columns show the ratio between values obtained with a not irradiated module and the maximally (6.5 $\times 10^{13}$ N.E. cm^{-2}) irradiated one.

4.8 Results

The irradiated modules operate properly at conditions similar to the LHC operation. The decrease of the signal to noise ratio for the maximally irradiated module to a non-irradiated one is ∼10% (Table 4.4). The module, which was irradiated to 10 years LHC equivalent, still works properly. The signal to noise ratio is well above the current default values, which is 11 for this module type [2].
The signal to noise ratio of the Hamamatsu module and the ST module are similar. The measured values are consistent with previous test beams, such as the May 2004 TEC test beam [42]. In the following the results of the different scans are presented.

Voltage Scan The signal and signal to noise ratio of the W5 modules are illustrated in figure 4.20. The measured values are quite similar. Nevertheless the Hamamatsu module accumulates more charge, but has slightly higher noise. The signal to noise ratio of the ST module is a bit higher.
The OB1 modules with different irradiation doses are compared in figure 4.21. As expected, the non-irradiated module performs best and the maximally irradiated has the lowest charge accumulation and signal to noise ratio. Although the inter-strip-coupling should slightly increase with irradiation, no clear evidence for this can be found within the errors in this data. The width of the fitted peak for inter-strip-

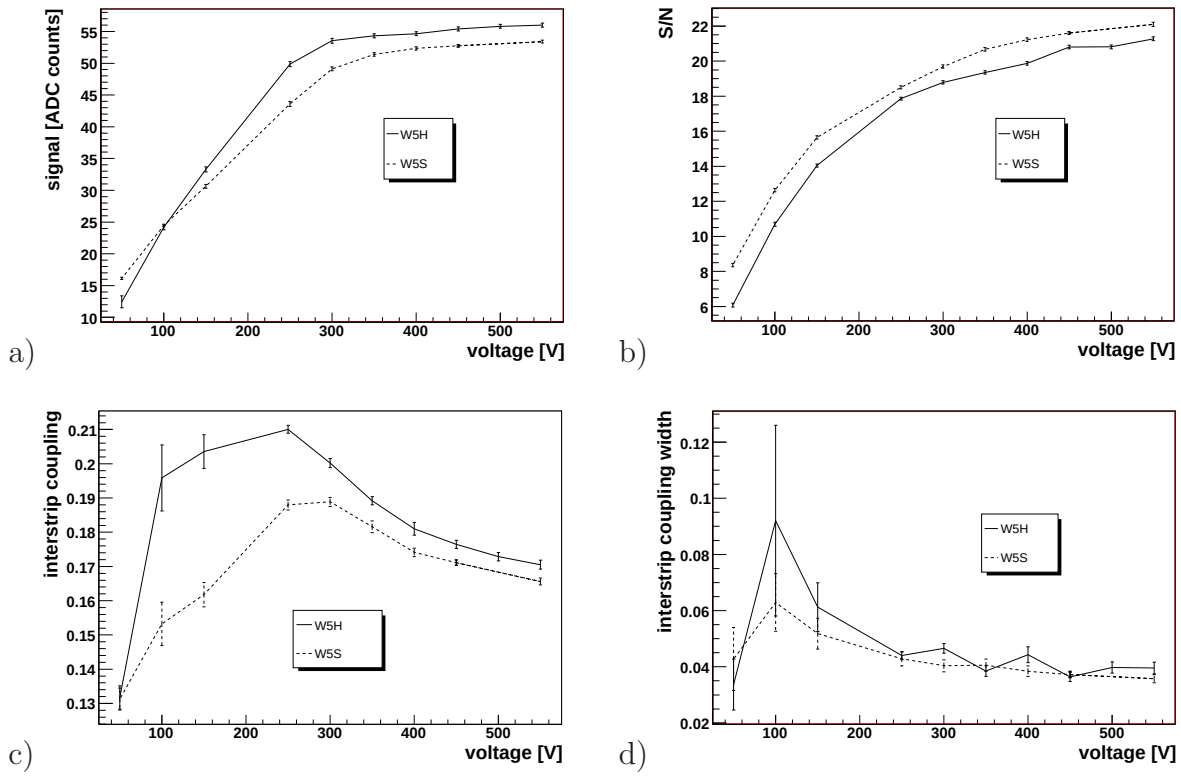

Figure 4.20: Comparison of Hamamatsu (W5H) and ST (W5S) sensors. a: signal, b: signal to noise ratio, c: inter-strip-coupling, and d: inter-strip-coupling width.

coupling (figure 4.18) is considerable. It should correctly be implemented in simulations, which is currently under investigation in CMS.
The results for the OB2 modules are presented in figure 4.22. The charge accumulation is very close to OB1 modules. The signal to noise ratio is slightly higher and the inter-strip-coupling is slightly smaller. This is due to the larger strip pitch of these modules. The inter strip capacity is reduced and therefore also the noise and the inter-strip-coupling.

Temperature Scan The signal, the signal to noise ratio, and the inter-strip-coupling depend significantly on the temperature. The signal increases by about 0.2 ADC (or 0.4%) counts per degree Celsius (figure 4.23). The signal to noise ratio grows by about 0.2 per degree Celsius. The inter-strip-coupling decreases significantly. The performance of the modules generally improves at low temperature. Even the most irradiated module could still be operated at -10° C with a signal to noise ratio of 16.2.

Angle Scan The signal increases with increasing inclination angle, since the ionization path is extended. The increment should be proportional to $1/\cos(\alpha)$, were alpha

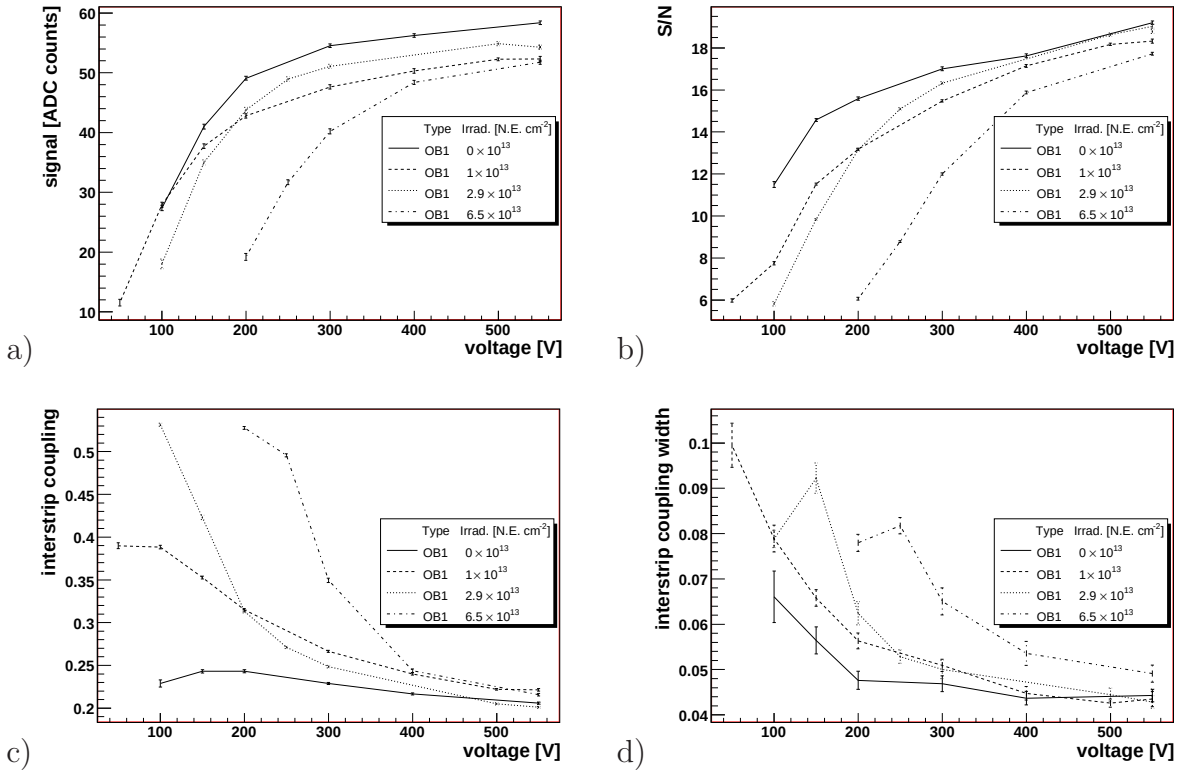

Figure 4.21: Voltage scan for OB1 modules with different irradiation. a: signal, b: signal to noise ratio, c: inter-strip-coupling, and d: inter-strip-coupling width.

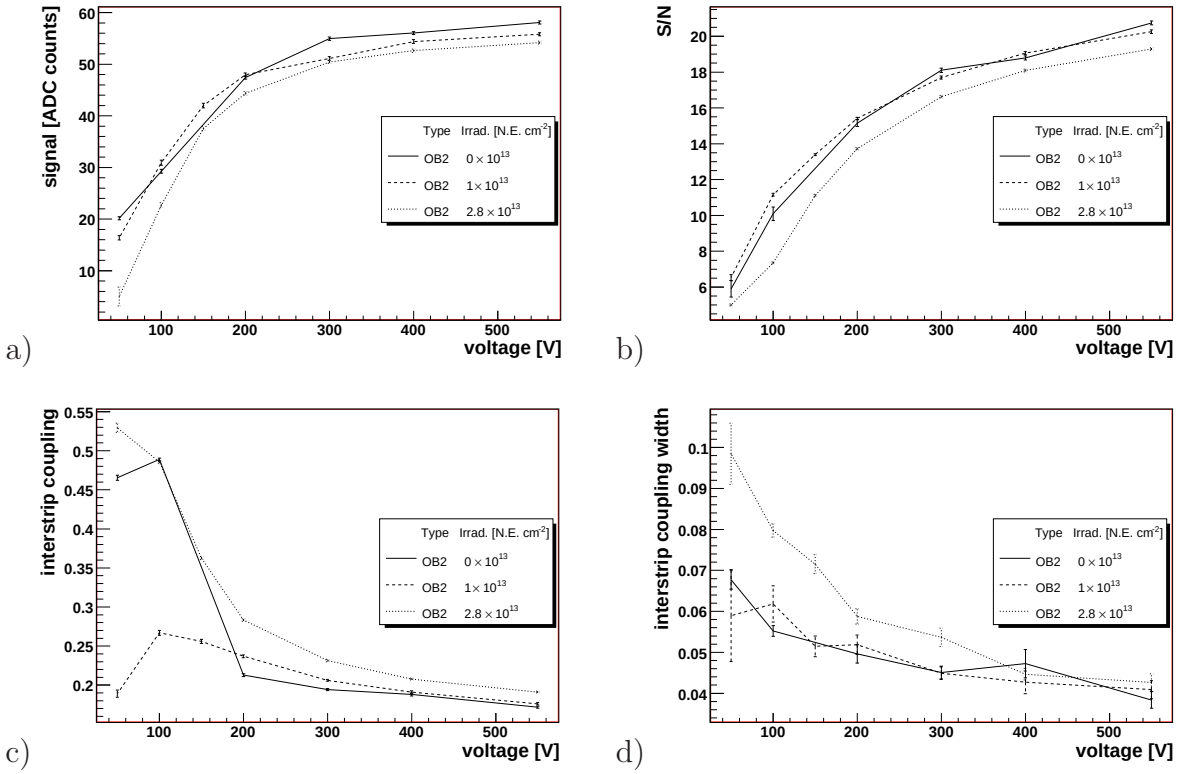

Figure 4.22: Voltage scan for OB2 modules with different irradiation. a: signal, b: signal to noise ratio, c: inter-strip-coupling, and d: inter-strip-coupling width.

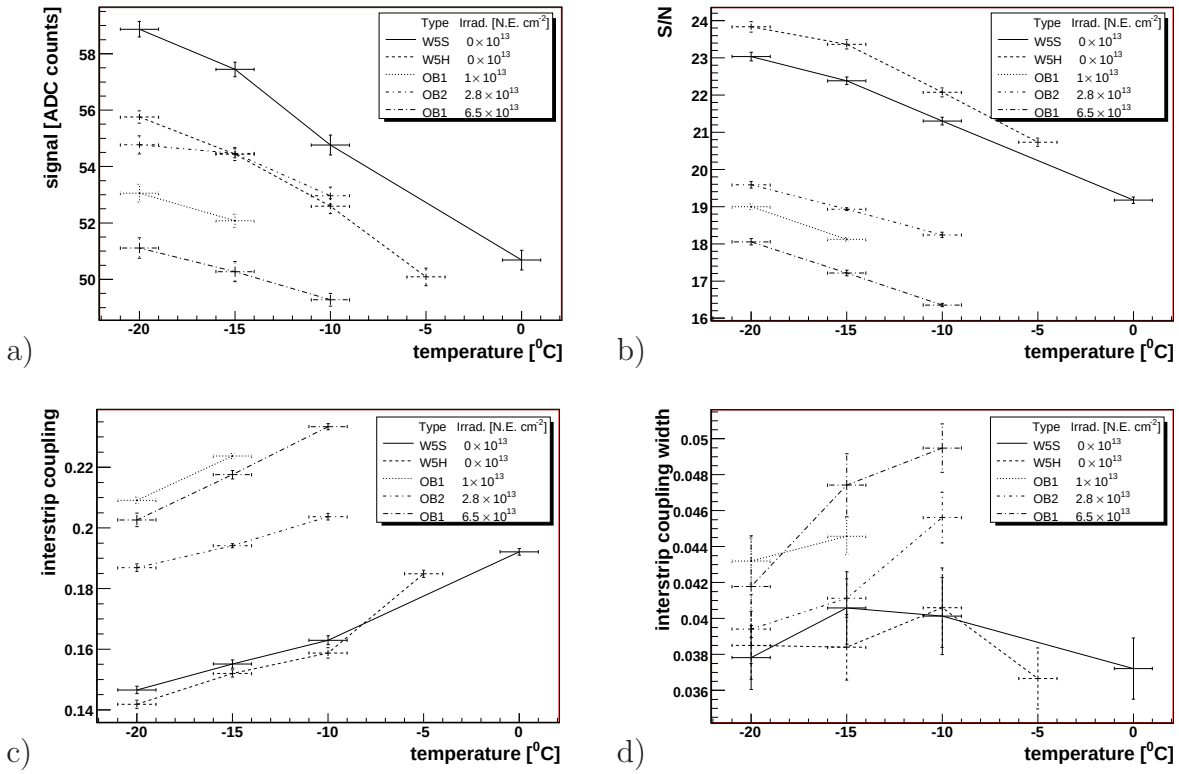

Figure 4.23: Temperature scan. Not all modules are included for better visibility. a: signal, b: signal to noise ratio, c: inter-strip-coupling, and d: inter-strip-coupling width.

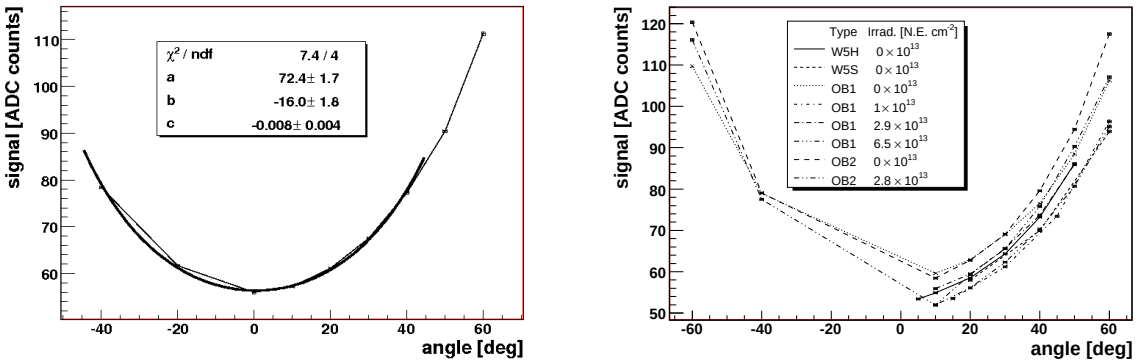

Figure 4.24: Angle scan. Left: fit of a angle scan with theoretical prediction, Right: angle scan for many modules.

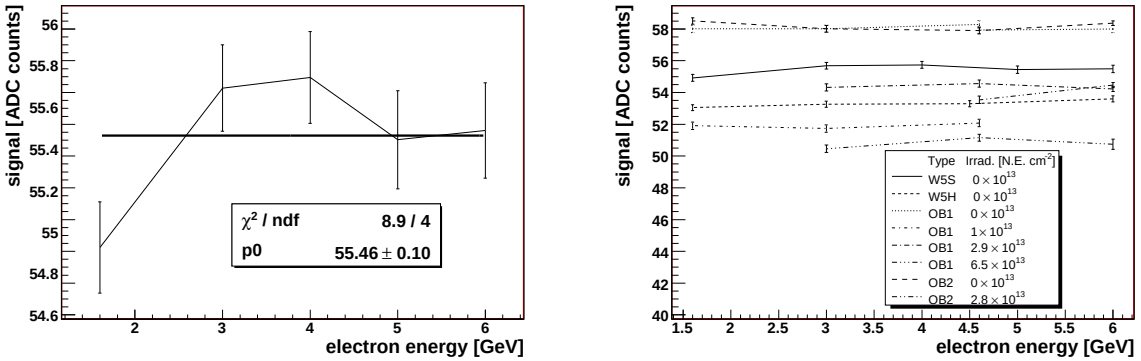

Figure 4.25: Energy scan. Left: fit to theoretical expectation, Right: energy scan for many modules.

is the inclination angle. The signal can be parameterized as follows.

$$s = \frac{a}{\cos(\alpha + c)} + b$$

Where $a - b$ is the signal for perpendicular tracks and c the angle offset. The angle offset should be small, since the mounting precision was about 1 degree. In figure 4.25 a fit of the signal measurement to the function s is shown. The signals at inclination angles above 45^0 tended to be slightly too small. The angle offset is 0.4^0 and therefore within the expectation. A plot of the signal measurement against the angle for all other modules is shown in figure 4.25. All modules behave as expected.

Energy Scan The measurements of the signal and noise should be independent of the electron energy in the present energy interval. As can be seen in figure 4.25, this agrees with the data. The plots are also used to estimate the additional error contributions other than the purely statistical errors used in the plots.

type	irradiation	1	2	3	4	5
OB1	0	30.5	28.8	28.8	28.4	26.4
OB1	6.5 $\times 10^{13}$ n.e. cm^{-2}	24.4	-	24.0	23.5	22.1

Table 4.5: Signal to noise ratio for the different points of th XY scan.

XY Scan The results for the XY scan for the OB1 modules are summarized in table 4.5. The module with the maximum irradiation and the non-irradiated module show similar behavior. The signal to noise ratio decreases with the distance to the read out end of the sensor. The relative difference between the signal to noise ratio of the hits at the far end (point 5, see figure 4.13) and the hits close to readout bonds (point 1) is about 10% for the non-irradiated and the irradiated module. Such behavior has also been seen at previous test beams [42]. The signal to noise ratios in the XY scan are higher than in the previously shown scans, since peak mode was used here.

Summary All the performed scans show that the irradiated modules will operate properly at various running conditions. The decrease of the signal to noise ratio by 10% due to irradiation was simular to the estimate in the Tracker TDR Addendum [1] and therefore gives confidence in the estimations made. Hence, it can be concluded that the silicon strip tracker irradiation is not a critical issue for the first ten years of *pp* collision data taking. However, the pixel sensors, which are closer to the interaction point, will have to be replaced after approximatly three years of operation.

Chapter 5

Alignment

In this chapter an introduction to alignment is given and the tools used for alignment are summarized. This includes the alignment algorithms as well as the definition of alignment parameters. First the alignment challenge for the CMS tracker is described and brought into perspective to previous experiments. Afterward the desired ingredients of an alignment strategy are presented. Then the currently investigated algorithms are presented. Finally the chosen algorithm is explained in detail and the misalignment simulation is described.

5.1 CMS Tracker Calibration/Alignment Challenge

The alignment of the CMS tracker is challenging in many ways. A big challenge is to obtain alignment corrections to a precision that insures that the performance of the tracker is not compromised. In addition, the alignment procedure must be feasible with a limited use of CPU time and memory. The CPU time needed should be in the order of hours and the necessary memory should not exceed several GBs.

Alignment Precision Challenge With the CMS tracking detectors, track parameters can be determined to very high precision, leading to high demands on the calibration. To avoid any effect due to misalignment, the positions of detectors should be known to the order of a few μm, which is an order of magnitude smaller than the typical intrinsic resolution of the sensors. However, even displacements of a few μm can have an effect on track parameter measurements, if the displacements are correlated.
The Laser Alignment System and the survey and mounting precision information lead to an uncertainty of $O(100)$ μm. Only track based alignment will be able to reduce the position uncertainty to the μm level.

Dataset Challenge As in any calibration procedures, a good standard reference is of major importance.

"Purpose of instrument calibration: Instruments calibration is intended to eliminate or reduce bias in an instrument's readings over a range for all continuous values. For this purpose, ***reference standards with known values*** *for selected points covering the range of interest are measured with the instrument in question. ..."* [57]

The availability of a good standard reference varies a lot for the different high energy physics experiments. There is a major difference between lepton colliders and hadron colliders: Lepton colliders typically have a well defined center-of-mass energy of the colliding leptons and the center of mass frame and the experimental frame are identical (eg. LEP experiments) or at least the transformation between the frames is well known (eg. BARBAR). The annihilation of the accelerated electrons and a subsequent production of a muon pair is an ideal source of reference tracks. The muons are exactly back to back and have a *known momentum* value.
Hadron colliders do not have such a standard reference to calibrate to, making the task of aligning them much more complicated. The H1 experiment, for example, used cosmic muon data without magnetic field. Their straight tracks can be interpreted as *infinite momentum* reference tracks.
For CMS the masses of decaying particles can be used, but unfortunately even particles with high masses are boosted and the width of the heaviest particle of the standard model decaying to two muons (Z^0) is large. The idea of using magnetic field-off data was discussed, but unfortunately the expected deformations of the tracking detectors, when turning on the 4T magnetic field, are rather large.

Computational Challenge With 13252 silicon modules[1], the CMS tracker is by far larger than silicon trackers and vertex detectors built up to now. About 50000 alignment parameters are necessary for the whole tracker, which is an order of magnitude larger than the alignment problems in high energy physics so far. Simply applying well established alignment algorithms such as Millepede I [58] algorithm would result in numerical and computational problems (see chapter 5.3). A new version of the Millepede (Millepede II), which was especially developed to minimize the memory and CPU time usage, is used in this thesis.

In conclusion, the size of the detector, the lack of "golden datasets", and the high precision demands make the alignment of the CMS tracker a very challenging task.

[1] Stereo modules are counted as one module.

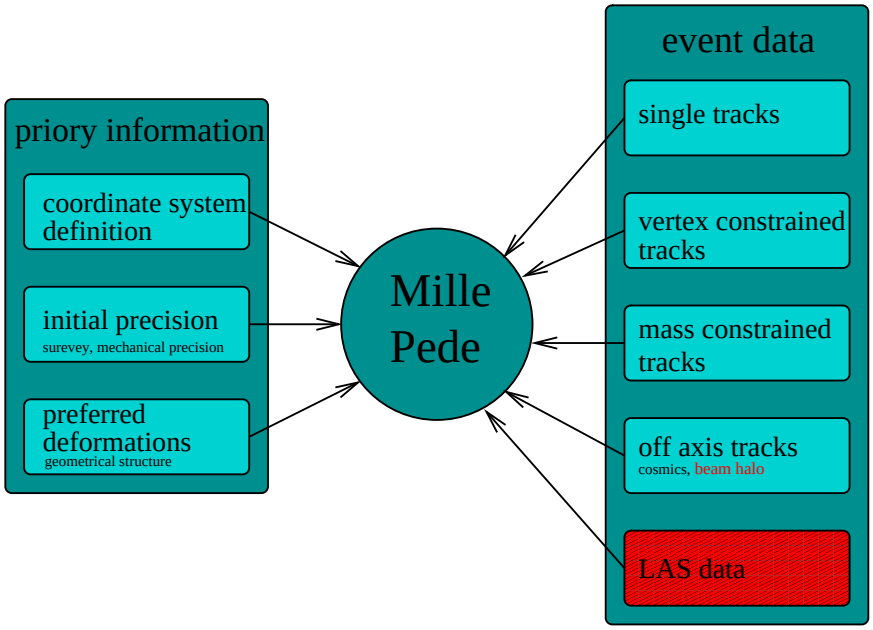

Figure 5.1: Schematic illustration of the alignment strategy. All elements of this strategy have been used except the Laser Alignment System (LAS) and beam halo data which have not yet been available.

5.2 Introduction to Alignment

The aim of track based alignment procedures is to reduce the χ^2 of track fits and to reduce the bias and uncertainty of the fitted track parameters. The reduction of the χ^2 of track fits is important to ensure track and vertex recognition. The small χ^2 of track fits allows to identify hits which would increase the χ^2 and hence do not belong to the track. However, even with the χ^2 of track fits minimized and pattern recognition well working, it is still possible to end up with biased measurements of track parameters due to misalignment. Correlated displacements of sensors which introduce a track parameter bias, but do not change the mean χ^2, are the core problem of alignment/calibration. The basic problem is the lack of good standard references for the calibration task.
Given this situation, it is mandatory to develop a sophisticated alignment strategy. The most important ingredients are complementary datasets. Off beam axis trajectories like beam halo and cosmics connect different tracker parts via tracks, effectively reducing displacements of these parts with respect to each other. The biases of track parameter measurements in these connected parts are forced to be small or at least similar. Tracks from a common vertex also connect different tracker parts and known masses of decaying particles, like the Z^0 can be used as a reference. Interesting datasets are:

- Tracks from pp collisions.
- Cosmic ray muon tracks.
- Z^0 mass constraint.
- Vertex constraint.
- Beam halo muons, laser beam trajectories and survey measurements[2].

Another key ingredient are apriory known uncertainties of the sensor positions and correlations between the errors of the sensor position, which are introduced via the mechanical support structures of the tracker. The information stems from:

- Mechanical mounting and survey precision.
- Hierarchy of mechanical support frames.

However the use of this initial knowledge requires a good understanding of the mechanical properties and the time evolution of the position. Generally the information extracted from event data is to be preferred. In addition to the complementary datasets certain symmetries of the track parameter distributions can be used to extract information of the sensor positions. Such symmetries are for example:

- Same transverse momenta spectra for μ^+ and μ^- of particle decays ($Z^0 \to \mu\mu$).
- Independence of the transverse momenta of the azimuthal angle ϕ.

Naturally, it is important to optimally use these pieces of information. An alignment algorithm should be able to fulfill the following demands:

- Inclusion of all correlations between position parameters.
- Incorporation of equality constraints between position parameters.
- Incorporation of survey measurements.
- Fast turn around time and computational feasibility.
- Outlier treatment.

The algorithm used in this thesis, Millepede, and other proposed algorithms for CMS are briefly described in the next section. An overview of the alignment ingredients used is given in figure 5.1.

[2]No datasets available yet.

5.2.1 Alignment Algorithms

Most track based algorithms are based on the χ^2 minimization principle. At CMS a track typically consist of about 20 independent measurements such that the five parameters of a helix track are well overdetermined in principle (see section 5.5 for more details). The recorded measurements u_m can be compared to predictions of the track model. The predicted measurements u_p from the track model depend on the track parameters $\boldsymbol{\tau}_j$ and parameters $\mathbf{p}$, which describe the position, orientation and deformation of the detectors. The normalized residual z_{ij} between the predicted hit position and the recorded measurement of hit i is given by:

$$z_{ij} = \frac{u_{im} - u_{ip}(\boldsymbol{\tau}_j, \mathbf{p})}{\sigma_i}, \tag{5.1}$$

where σ_i is the uncertainty of the measurement. Seeking optimal agreement between the track model and the data, translates to a minimization of a function which depends on the normalized residuals.
Most commonly the function

$$\chi^2(\boldsymbol{\tau}, \mathbf{p}) = \sum_j \sum_i z_{ij}^2(\boldsymbol{\tau}_j, \mathbf{p}), \tag{5.2}$$

is minimized, where $\boldsymbol{\tau}$ is the vector of all track parameters. This function will be referred to as χ^2-function[3]. Generally, all overdetermined parameters from objects which are reconstructed in the tracker can be used for alignment. Examples are laser beams from the Laser Alignment System or tracks with a common vertex. The above definition neglects correlations between the measurements, but the measurements of different sensors are generally not significantly correlated. Significant correlations only occur in the CMS tracker if measurements from different sensors are combined into a single measurement or if the interactions of particles with material are a major source of uncertainty, which is only the case for low momentum tracks.

Algorithms in CMS There are standard methods to minimize a χ^2-function. If possible, the χ^2-function minimization problem is linearized [59]. Linear equality constraints can be implemented via Lagrangian multipliers. This procedure leads to optimal results as well as correct error estimation of the fitted parameters and the correlations of the parameters. Iterations are eventually needed to reduce errors due to linearization or to improve outlier rejection.

- The Millepede [58] algorithm, which is used in this thesis, follows this standard procedure. All demands on an alignment algorithm presented in the beginning of this section are fulfilled. The large number of parameters requires a scheme to reduce the matrix size reduction and fast solvers of matrix equation. A more

[3] χ^2-function is high energy physics terminology.

detailed description can be found in section 5.3.

Alternative algorithms pursued in CMS avoid the standard minimization procedure, since the amount of fitted parameters in minimization is very large.

- The HIP algorithm [63] minimizes a χ^2-function for each sensor individually with all the track parameters fixed (which the global χ^2-function does depend on) and hence ignores all correlations between the alignment parameters. In the next step new track parameters are calculated using the improved alignment parameters. These two steps are applied iteratively. Since correlations are ignored, it is not possible to give correct uncertainty estimates of the fitted parameters and the procedure might converge slowly or not at all.
- The most recently proposed alignment procedure is a Kalman Filter algorithm [64], where alignment parameters are updated after each track. It is able to incorporate correlations between alignment parameters, however not all correlations can be included, since the memory and CPU time needed in that case would exceed the available computing resources.

	Millepede II	Kalman	HIP
method	one go	sequential	iterative
correlations	all	some	none
correct uncertainty estimates	yes†	no	no
equality constraints	yes	no*	no*
survey measurements	yes	no*	yes

Table 5.1: Basic properties of algorithms proposed within CMS. yes†: not all uncertainties can be calculated for CPU time reasons. no*: no method implemented, but not theoretically impossible.

5.3 Global Linear χ^2 Minimization with Constraints (Millepede II)

As explained in the previous section the alignment algorithm minimizes the χ^2-function. The first step in the minimization is to linearize the minimization problem. This translates into a linearization of the normalized residuals z_i in the χ^2-function:

$$\chi^2 = \sum_j \sum_i z_{ij}^2(\mathbf{p}, \boldsymbol{\tau}_j) \simeq \sum_j \sum_i \frac{1}{\sigma_i^2}\big(u_{mi} - u_{pi}(\mathbf{p_0}, \boldsymbol{\tau_{j0}}) + \frac{\partial u_{pi}}{\partial \mathbf{p}}\delta\mathbf{p} + \frac{\partial u_{pi}}{\partial \boldsymbol{\tau}_j}\delta\boldsymbol{\tau}_j\big)^2, \quad (5.3)$$

where $\mathbf{p_0}$ are the initially assumed geometry parameters and $\boldsymbol{\tau}_0$ the initially assumed track parameters. The geometric correction parameters $\delta\mathbf{p}$ are referred to as alignment parameters $\mathbf{a}$ in the following. The alignment parameters are also called global parameters, since they are not specific to a single track or event. The track parameter corrections for a track are specific only for a single event and hence the parameters $\delta\boldsymbol{\tau}$ are called the local parameters. The local parameters $\delta\boldsymbol{\tau}$ do not always need to be track parameters but can also be other parameters like the vertex position of an event.

5.3.1 Matrix Reduction

The minimization of the function $\chi^2(\mathbf{a}, \boldsymbol{\tau})$, leads to a system of linear equations [59]. The number of track (local) parameters $\boldsymbol{\tau}$ can be in the order of millions and hence the matrix has millions of rows. In addition, there are ∼50k equations for the alignment parameters. However the nature of the local parameters yield a special structure of the matrix:

$$\left(\begin{array}{c|c|c|c} \sum \mathbf{C}_j & \dots & \mathbf{G}_j & \dots \\ \hline \vdots & \ddots & 0 & 0 \\ \hline \mathbf{G}_j^T & 0 & \boldsymbol{\Gamma}_j & 0 \\ \hline \vdots & 0 & 0 & \ddots \end{array}\right)\left(\begin{array}{c} \mathbf{a} \\ \hline \vdots \\ \hline \delta\tau_j \\ \hline \vdots \end{array}\right) = \left(\begin{array}{c} \sum \mathbf{b}_j \\ \hline \vdots \\ \hline \beta_j \\ \hline \vdots \end{array}\right),$$

which can be exploited to reduce the matrix size. The sub-matrices $\boldsymbol{\Gamma}_j$ include only derivatives with respect to local parameters. The matrices $\mathbf{G}_j$ include derivatives with respect to local and global parameters. Only derivatives with respect to global parameters are found in the matrices C_j. $\mathbf{b}$ includes products of global derivatives

and the normalized residuals, and β_j local derivatives and the normalized residuals. A matrix $\mathbf{C}'$ and a vector $\mathbf{b}'$ can be defined as follows:

$$\mathbf{C}' = \sum_i \mathbf{C}_i - \sum_i \mathbf{G}_i \mathbf{\Gamma}_i^{-1} \mathbf{G}_i^T \qquad \mathbf{b}' = \sum_i \mathbf{b}_i - \sum_i \mathbf{G}_i (\mathbf{\Gamma}_i^{-1} \beta_i) \tag{5.4}$$

This leads to a smaller equation system as is described in [59] and [60], which needs to be solved to determine the alignment parameters $\mathbf{a}$:

$$\begin{pmatrix} & \mathbf{C}' & \end{pmatrix} \begin{pmatrix} \mathbf{a} \end{pmatrix} = \begin{pmatrix} \mathbf{b}' \end{pmatrix} \tag{5.5}$$

Using this matrix size reduction in the context of a χ^2 minimization of the alignment problem is the core idea of the Millepede algorithm.
In the course of the matrix size reduction (last term in equation 5.4), correction parameters for each track $\delta\tau_j$ are calculated:

$$\delta\tau_j = \mathbf{\Gamma}_j^{-1} \beta_j \tag{5.6}$$

This is essential in order to extract the χ^2 and the number of degrees of freedom of the track fit for a given geometry.

5.3.2 Constraints

A set of linear equality constraints can be expressed by a matrix equation:

$$\mathbf{A}\mathbf{a} - \mathbf{m} = 0$$

Linear equality constraints on the alignment parameters $\mathbf{a}$ can be applied via Lagrangian Multipliers. This leads to the following matrix equation [59]:

$$\left(\begin{array}{c|c} \mathbf{C}' & \mathbf{A}^T \\ \hline \mathbf{A} & 0 \end{array}\right) \left(\begin{array}{c} \mathbf{a} \\ \hline \lambda \end{array}\right) = \left(\begin{array}{c} \mathbf{b}' \\ \hline \mathbf{m} \end{array}\right)$$

If Lagrangian multipliers are used, then the matrix is not positive definite any more, which has to be kept in mind while choosing methods to solve the equation system.

5.3.3 Survey Measurements

Survey measurements can be implemented just like hit measurements. The normalized residual of the measurement m, namely the residual between the expected measurement from the initial geometry and performed measurement divided by the measurement uncertainty, need to be expressed as a function of the position parameters:

$$m(\mathbf{p}) \sim \sum_k \frac{\partial m}{\partial a_k} \delta a_k, \tag{5.7}$$

where k is the index of the vector component $\mathbf{a}$. The derivatives and the residual of the measurement are simply incorporated like the measurements from tracks.

5.3.4 Linear Equation Solvers

The size of the linear system of equations 5.4 is equal to the number n of alignment parameters. In the case of the CMS tracker, these are about 50000 parameters, hence the straight-forward procedure of inversion of the matrix $\mathbf{C}'$ is technically impossible with the currently available computing power. However, there are algorithms solving linear equations much faster than an inversion method, if the corresponding matrix is sparse. These algorithms do not modify the matrix $\mathbf{C}$ during the solution; they require only the product $\mathbf{C}\cdot$vector, which can be very fast for a sparse matrix. Several different methods are implemented in Millepede II to be able to solve also large linear equation systems.

Inversion The CPU time needed for inverting a $n \times n$ matrix scales with n^3 and the memory needed to store the matrix with n^2. Therefore it is not applicable for very large systems. The inverted matrix is also the covariance matrix for the parameters and includes information like correlations and error estimations.

Diagonalization The computing requirements even exceed the inversion method. However the eigenvectors and eigenvalues which are determined can be physically interpreted. Eigenvectors with small eigenvalues have little impact on the overall χ^2 and are therefore not well determined. This can be used for diagnostics of the alignment problem.

Variable Band Cholesky Cholesky decomposition can be used to solve a system of linear equations which can be represented by a symmetric matrix. If the matrix is a symmetric variable[4] band matrix, this method is very fast. Only the matrix elements within the band need to be stored. However, the matrix which is built in the course of the χ^2 minimization is not a band matrix. Ignoring the elements outside the chosen band means ignoring correlations due to common tracks between alignment parameters, which are further apart than one bandwidth from each other within the matrix. Still, even parameters which are far apart in the matrix are not completely uncorrelated, since they are correlated via other parameters to each other. This is reflected by the fact that the inverse matrix (covariance matrix) of the band matrix is not a band matrix.
So, the solution obtained via the band Cholesky method ignores some correlations and is therefore only an approximate solution, hence iterations are required. The band width can be varied within the matrix, however the band width $\mathbf{m}$ is set to a constant value for the matrix $\mathbf{C}'$, which is the matrix including the equations from

[4]The bandwidth can be varied within the matrix.

methods	memory space required [8 byte words]
inversion	n+n(n-1)/2
diagonalization	n+n(n-1)/2+n^2
band Cholesky	nm
GMRES (sparse)	n+qn(n-1)3/4

Table 5.2: Memory requirements for the matrix C‘: n is number of global parameters, m the band width for the Choleskey band method and q the matrix density. The space needed for equality constraints is not included.

the χ^2 minimization without constraints. For the rows which are added in order to incorporate the linear equality constraints, the full rows are taken into account. This allows to enforce the constraints when using the Cholesky method (see fig. 5.2).
The band Cholesky method is also used to implement a HIP like algorithm. The original HIP algorithm translates to ignoring all elements of the matrix $\mathbf{C}'$, except the block diagonal matrices $\mathbf{C_j}$ for each individual sensor (see fig. 5.2). The version of the HIP algorithm implemented in Millepede II allows to apply constraints on the alignment parameters. The iterations if the HIP algorithm is used are done within Millepede, since the track refits are done within Millepede. Thus the number of iterations on reconstruction level within the CMSSW framework can be reduced significantly, if this HIP version is used.

GMRES (Sparse Matrices) If the matrix $\mathbf{C}'$ is sparse (contains many zero elements) the memory demand can be reduced by storing only non-zero elements. Each stored element (eight bytes) needs additionally a pointer (four bytes) to store its position within the matrix. The memory need in comparison to other methods is shown in table 5.2. For example, two GB memory are needed if the matrix density of $\mathbf{C}'$ is 15% for the CMS tracker. If only tracks from the interaction point are used, the density of the matrix is about 1%. Trajectories which cross several detector parts, which are usually not crossed by a single track from the interaction point lead, to a denser matrix. If tracks are refitted with a common vertex and cosmic muons and beam halo muons are used, then the matrix density easily exceeds 10%.
Millepede II incorporates the GMRES method [65]. It is a more generically applicable version of the MINRES algorithm [66], which can only be applied to positive definite matrices.
The speed of convergence and precision can be improved if the matrix equation is multiplied by an approximated solution of the inverse of the matrix, which is called preconditioning. Preconditioning can be done with the variable band Cholesky method.

$$\left(\begin{array}{cccccc|c} c_{11} & \dots & c_{1m} & 0 & \dots & 0 & \\ \vdots & \ddots & 0 & \ddots & \ddots & \vdots & \\ c_{m1} & \ddots & \ddots & \ddots & \ddots & 0 & \mathbf{A}^T \\ 0 & \ddots & \ddots & \ddots & \ddots & c_{(n-m)n} & \\ \vdots & \ddots & \ddots & \ddots & \ddots & \vdots & \\ 0 & \dots & 0 & c_{n(n-m)} & \dots & c_{nn} & \\ \hline & & & \mathbf{A} & & & 0 \end{array}\right) \qquad \left(\begin{array}{ccccc|c} \mathbf{C}_1 & 0 & \dots & \dots & 0 & \\ 0 & \mathbf{C}_2 & 0 & \ddots & \vdots & \\ \vdots & 0 & \ddots & \ddots & \vdots & \mathbf{A}^T \\ \vdots & \vdots & \ddots & \ddots & 0 & \\ 0 & \dots & \dots & 0 & \mathbf{C}_k & \\ \hline & & \mathbf{A} & & & 0 \end{array}\right)$$

Figure 5.2: Matrices representing the linear equation system which are solved with the band Cholesky method. Left: The variable bandwidth allows to include the linear constraints by including the full sub-matrix $\mathbf{A}$. Right: Schematic illustration of a matrix with the block diagonal structure of the HIP algorithm.

5.3.5 Outlier Rejection

The minimization of the χ^2-function is only optimal if the distributions of the errors are Gaussian, but due to wrongly assigned hits or simply due to non-Gaussian hit reconstruction errors this assumption is not correct. In a χ^2-minimization the influence of a normalized residual z_i increases linearly with its absolute value. Recorded hits (outliers) which are many standard deviations away from the expected hit position have therefore a large impact on the result. To improve the performance, tracks with outliers can be rejected or hits reweighted. Millepede internal iterations become necessary in the course of this procedure.

Track rejection The local refit (formula 5.5) within Millepede allows to determine the χ^2 and the number of degrees of freedom (ndof) for each track fit. A cut χ^2/ndof is applied to reject badly reconstructed tracks. However, in the first iteration the χ^2 is generally large, since the sensors are misaligned and therefore soft cuts need to be applied. The cuts are then tightened with each iteration, since the χ^2 decreases with the improved alignment precision. However, the χ^2/ndof values of corrupted tracks remain large, hence they are rejected.

Hit Weighting The impact of outlier hits can be reduced by down-weighting their influence to the minimization problem. A standard method (M-estimates) is not to minimize the χ^2-function but a different function F of the normalized residuals.

$$F(\tau_{\mathbf{i}}, \mathbf{a}) = \sum_i f(z_i(\tau_{\mathbf{i}}, \mathbf{a}))$$

where f can be the *Huber function* or the *Cauchy function* (see table 5.3).
If the Huber-function is used the influence of the normalized residuals z, which are larger than C_H, remains constant. A standard value for C_H is 1.345, which would

function f(z)	influence(z)=$\frac{df}{dz}$	weight factor(z)=$\frac{df}{dz}\frac{1}{z}$
$\chi^2 \rightarrow \frac{z^2}{2}$	z	1
Huber $\rightarrow \begin{cases} \frac{z^2}{2} & \text{if } \lvert z\rvert < C_H \\ C_H(\lvert z\rvert - \frac{C_H}{2}) & \text{if } \lvert z\rvert > C_H \end{cases}$	z C_H	1 $\frac{C_H}{\lvert z\rvert}$
Cauchy $\rightarrow \frac{C_C^2}{2}\ln(1+(\frac{z}{C_C})^2)$	$z/(1+(\frac{z}{C_C})^2)$	$1/(1+(\frac{z}{C_C})^2)$

Table 5.3: Influence function and weight factor function derived from different functions $f(z)$.

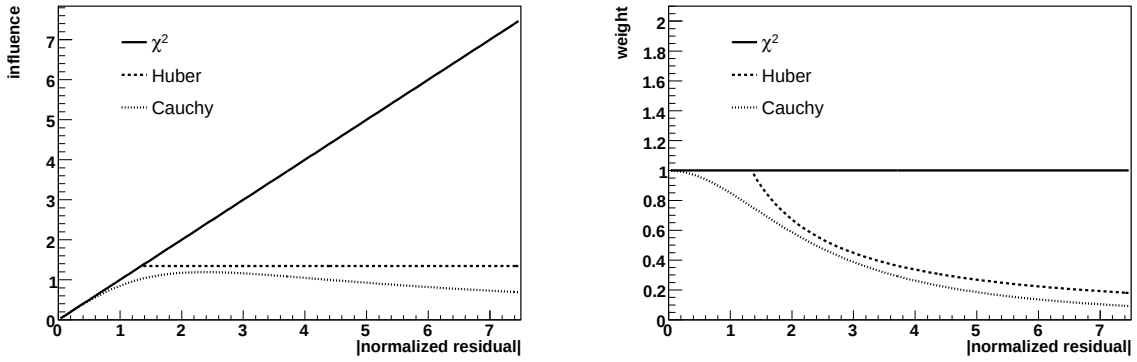

Figure 5.3: Left: The influence functions for χ^2, Huber and Chauchy methods. Right: Weight factor functions.

result in an increase of the parameter uncertainty of 5%, if the error destributions are Gaussian. If the Cauchy-function is used the influence even decreases for very large normalized residuals.
The track (local) fit is done iteratively when using the reweighting method, since the new weights lead also to new track parameters. For the first two iteration the Huber-function is used and the Cauchy-function for the following iterations.
If the average weight of the hits of a track is small, then this indicates that a number of hits are incorrectly measured. Hence, it is reasonable to reject tracks with a small average weight. Note that it is strictly speaking not correct to speak of a χ^2 minimization anymore, if reweighting is applied.

5.3.6 Computational Layout

An important aspect of alignment is the time used for analysis. Therefore the information used by Millepede have to be collected in an efficient way. Collecting the necessary derivatives and measurements from the data within the CMS framework is a relatively slow process, especially since the simulated misalignment requires refits of

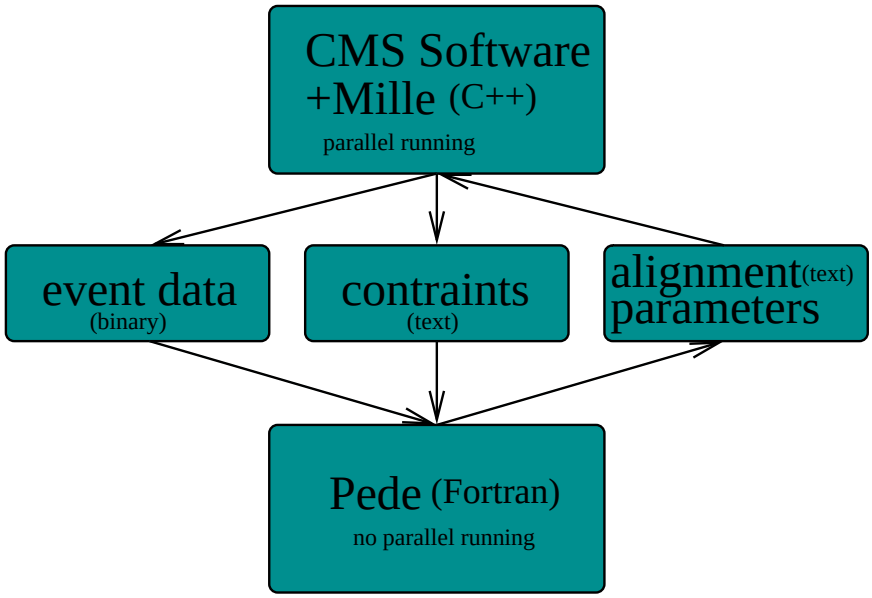

Figure 5.4: Schematic illustration of the computational layout.

all used tracks. This process can be parallelized and the results are stored in binary files. Millepede II is split into two parts, one part (Mille) accumulates the derivatives and measurements and stores them in binary files. This part needs to be interfaced to the CMS software. The data accumulation can be parallelized. The other part (Pede) determines the alignment parameter from the binary files and is a standalone FORTRAN program. This clean cut between the CMS software and Pede makes it possible to use Pede easily in other experiments as well. The output of Pede are the alignment parameters stored in an text file, which is then read by the CMS software. The scheme is illustrated in figure 5.4.

5.4 Alignment Parametrization

First an overview is given, describing how the geometry of the CMS-tracker is used. Afterward alignment parameterizations for different detectors are explained.

5.4.1 Local Coordinate Systems and Transformations

For each sensor a local coordinate system is defined. A vector in the local system is denoted as $\mathbf{q}$ with components u, v, and w defined with respect to the center of the sensor. The u-axis is defined along the precisely measuring coordinate of the sensor, the v-axis is orthogonal to the u-axis and in the sensor-plane. The w-axis is normal to the sensor-plane. Except for a sign ambiguity, the precise coordinate of a sensor translates to the global $r\phi$ coordinate. This holds also true for sensors which measure two dimensions. The hit measurements are done in the local frame and need to be transformed to the global frame. The transformation of a local vector $\mathbf{q}$ to a vector $\mathbf{r}$ in the global coordinate system is given by:

$$\mathbf{r} = \mathbf{R}^T\mathbf{q} + \mathbf{r}_0 \tag{5.8}$$

The position of the sensor is $\mathbf{r}_0$ and the rotation-matrix $\mathbf{R}^T$ defines its orientation.

5.4.2 Alignment Parameters for Individual Sensors

The alignment procedure determines a correction to the initial transformations (5.8) by an incremental rotation $\Delta\mathbf{R}$ and a translation $\Delta\mathbf{q}$.

$$\mathbf{r} = \mathbf{R}^T\boldsymbol{\Delta}\mathbf{R}(\mathbf{q} + \boldsymbol{\Delta}\mathbf{q}) + \mathbf{r}_0 \tag{5.9}$$

The alignment parameters for translations are the components of $\Delta\mathbf{q}$, namely Δu, Δv and Δw. The corrections are preferably expressed in the local coordinate system, since they correspond to the properties of the measurements on the individual sensor. The precise and the insensitive coordinates are naturally separated, simplifying the separation of potentially indeterminable corrections. As an example, the parameter $\Delta\mathbf{v}$ will be hardly determined for one dimensional measuring sensors and can be ignored. The rotation matrix $\boldsymbol{\Delta}\mathbf{R}$ can be reduced to three angles. The angles chosen are the rotation around the u-axis, the new v-axis and the new w-axis. The angles are denoted as α, β and γ. All rotation axes cross the center of the sensor, otherwise a rotation would also result in a shift of the sensor center.
So each sensor has a vector of six alignment parameters:

$$\mathbf{a} = \begin{pmatrix} \Delta u \\ \Delta v \\ \Delta v \\ \alpha \\ \beta \\ \gamma \end{pmatrix} \tag{5.10}$$

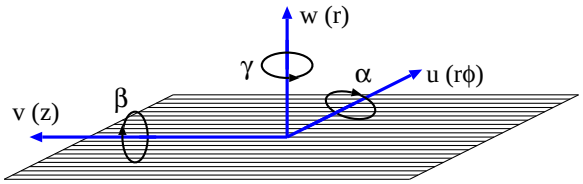

Figure 5.5: Schematic illustration of the alignment parameter definition.

The individual rotation correction matrices are:

$$\Delta\mathbf{R}_\alpha = \begin{pmatrix} 1 & 0 & 0 \\ 0 & \cos\alpha & \sin\alpha \\ 0 & -\sin\alpha & \cos\alpha \end{pmatrix} \quad \Delta\mathbf{R}_\beta = \begin{pmatrix} \cos\beta & 0 & -\sin\beta \\ 0 & 1 & 0 \\ \sin\beta & 0 & \cos\beta \end{pmatrix}$$

$$\Delta\mathbf{R}_\gamma = \begin{pmatrix} \cos\gamma & \sin\gamma & 0 \\ -\sin\gamma & \cos\gamma & 0 \\ 0 & 0 & 1 \end{pmatrix}$$

The rotation correction matrix for the complete rotation is then:

$$\Delta\mathbf{R} = \begin{pmatrix} \cos\beta\cos\gamma & \cos\alpha\sin\gamma + \sin\alpha\sin\beta\cos\gamma & \sin\alpha\sin\gamma - \cos\alpha\sin\beta\cos\gamma \\ -\cos\beta\sin\gamma & \cos\alpha\cos\gamma - \sin\alpha\sin\beta\sin\gamma & \sin\alpha\cos\gamma + \cos\alpha\sin\beta\cos\gamma \\ \sin\beta & -\sin\alpha\cos\beta & \cos\alpha\cos\beta \end{pmatrix} \tag{5.11}$$

In practice it might occur that $\Delta\mathbf{R}$ is given and the alignment parameters α, β and γ need to be calculated. This can be necessary if simulation truth and calculated alignment corrections are compared. If β is chosen such, that the absolute value is smaller than $\pi/2$, than the Euler angles can be uniquely determined:

$$-\pi/2 < \beta < \pi/2 \qquad \beta = \arcsin r_{13}$$

$$\alpha = \begin{cases} \tan^{-1}\frac{-r_{32}}{r_{33}} & (r_{33}\cos\beta > 0) \\ \tan^{-1}\frac{-r_{32}}{r_{33}} + \pi & (r_{33}\cos\beta < 0) \end{cases} \qquad \gamma = \begin{cases} \tan^{-1}\frac{-r_{21}}{r_{33}} & (r_{11}\cos\beta > 0) \\ \tan^{-1}\frac{-r_{21}}{r_{33}} + \pi & (r_{11}\cos\beta < 0) \end{cases},$$

where r_{ij} are the elements of correction matrix $\Delta\mathbf{R}$.
It should be kept in mind that translations and rotations are not commutative, since the rotation axes are changed by translations and the translation directions are changed by prior rotation corrections. These are second order effects though and can therefore be neglected.

5.4.3 Global Derivatives for Sensor Parameters

The derivatives of the residuum with respect to the alignment parameters are input for the χ^2 minimization and therefore of vital importance. In correspondence to global

parameters the derivatives are called global derivatives. The residual ζ between the measured hit position on the sensor $\mathbf{q}_m$ and the hit position $\mathbf{q}_p$ predicted by the fitted trajectory in the sensor plane is given by:

$$\zeta = \begin{pmatrix} u_r \\ v_r \end{pmatrix} = \begin{pmatrix} u_m \\ v_m \end{pmatrix} - \begin{pmatrix} u_p \\ v_p \end{pmatrix} \tag{5.12}$$

The w coordinate is neglected, since the hits are always on the sensors surface. For one dimensional sensors the residuum is reduced to the difference in the sensitive coordinate. Since the alignment corrections are small, the fitted trajectories can be linearly approximated in the vicinity of the detector plane. The size of the region, where the linear approximation is done, is determined by the alignment uncertainty, which is expected to be at most a few hundred μm. Therefore the curvature of the track is actually not needed to calculate the global derivatives. The correction angles α, β and γ are assumed to be of the order of few mrad, so the linearization of the rotation corrections is entirely valid. When determining the derivative, one has to consider the translation due to the applied corrections of the sensor position and orientation. Additionally, the hit position is constrained to be on the trajectory and on the sensor surface. The complete calculation can be found in Appendix C.1. The derivative is calculated at the point where all alignment parameters are zero. This is the natural choice for the linearization point, since no corrections are assumed prior to the alignment:

$$\frac{\partial \zeta}{\partial \mathbf{a}} \Big|_{\mathbf{a}=0} = \mathbf{P} \begin{pmatrix} -1 & 0 & \frac{du_p}{dw} & -v_r \frac{du_p}{dw} & u_r \frac{du_p}{dw} & -v_r \\ 0 & -1 & \frac{dv_p}{dw} & -v_r \frac{dv_p}{dw} & u_r \frac{dv_p}{dw} & u_r \end{pmatrix} \tag{5.13}$$

The projection matrix $\mathbf{P}$ reduces the matrix to one row, if only one dimension is measured.

5.4.4 Composite Detectors

Composite detectors are detector components which consist of several subcomponents. Between sensor and the full tracker three composite structure levels are implemented. Sensors are mounted on small supporting structures, like rods in the outer barrel. These are mounted on layers, and the layers are assembled on the largest subcomponents of the tracker, such as a half barrel for example. There are several reasons why composite detectors should be assigned additional alignment parameters. Alignment parameters of composite structures are necessary to implement the knowledge from survey measurements and mounting precisions in form of prior error estimates for the alignment parameters of such structures.
For simplified alignment studies it turned out to be very useful to have the opportunity to test alignment with composite detectors. Since their sensitive surface is much larger, fewer events are needed to have sufficient information for each aligned object. The reduced number of alignment parameters also allows to use CPU intensive methods, such as inversion. This way the covariance matrix is calculated and

the alignment problems can be better understood. Furthermore, during data taking it might be useful to align only composite detectors, if the sensors position on these detectors are already known to sufficient precision. The movement of larger structures could be monitored with little statistics.

5.4.5 Alignment Parameters of Composite Detectors

To each composite structure a local coordinate system is assigned. The origin of a composite object is generally defined in this thesis as the mean of the origins $\mathbf{r}_{i0}$ of the subcomponents. The orientation is defined in analogy to the definition of the sensors coordinate systems. Therefore, the local u direction is along the precisely measured coordinate, which is generally the global $r\phi$ direction. The local coordinate w is normal to the plane and points to the CMS tracker's surface, rather than to its center. This definition might be undetermined for some structures, such as half barrels for example. In those cases, the orientation of the global coordinate system is used. The definition of the alignment parameters $\mathbf{a}_c$ is equivalent to the definition of the sensor parameter in section 5.4.2. An alignment correction $\mathbf{a}_c$ can be translated in alignment corrections $\mathbf{a}_i$ of its subcomponents i. These transformations can be done via a matrix multiplication with matrices $\mathbf{C}_i$. The calculation of $\mathbf{C}_i$ can be found in the Appendix C.2.

$$\mathbf{a}_i = \mathbf{C}_i \mathbf{a}_c \tag{5.14}$$

To calculate the derivative of the residuum with respect to the composite alignment parameters, the chain rule can be applied:

$$\frac{\partial \mathbf{r}}{\partial \mathbf{a}_c} = \frac{\partial \mathbf{r}}{\partial \mathbf{a}_i} \frac{\partial \mathbf{a}_i}{\partial \mathbf{a}_c} = \frac{\partial \mathbf{r}}{\partial \mathbf{a}_i} \mathbf{C}_i \tag{5.15}$$

5.4.6 Simultaneous Alignment of Composite Detectors and Subcomponents

If composite detectors and their sub-detectors are simultaneously aligned, the χ^2 minimization has no unique solution. Obviously, the composite detectors can be moved and all its subcomponents can be moved in the exactly opposite way, which results in no movement of any sensors. Additional parameters without additional information, such as parameters of composite detectors, naturally produce rank-defects of the linear equation matrix. To avoid this, for each composite alignment parameter, a new constraint has to be introduced. In the previous section, it has been shown how composite alignment parameters translate to the parameters of their components. This can be reversed:

$$\mathbf{a}_c = \sum_{i=0}^{i=n} \mathbf{C}_i^{-1} \mathbf{a}_i \tag{5.16}$$

An equality constraint is required to allow only linear combinations of the subcomponent alignment parameters, which leave the composite object alignment parameters invariant:

$$0 = \sum_{i=0}^{i=n} \mathbf{C}_i^{-1} \mathbf{a}_i \tag{5.17}$$

These constraints also change the interpretation of the subcomponent's alignment parameters. They do not represent anymore the absolute corrections, which are needed to be applied to a subcomponent. These parameters correct only the misplacement of the subcomponents on the composite structure. Composite structures can also be defined recursively. The corrections needed due to the misplacement of a composite structure can be calculated with the corresponding matrices $\mathbf{C}$. The total corrections applied to sensor i are then:

$$\mathbf{a} = \mathbf{a}_i + \mathbf{C}_{ij}\mathbf{a}_{cj} + \mathbf{C}_{jk}\mathbf{a}_{ck} + ...$$

where j,k, ... are the composite structures indices.

5.4.7 Possible Extensions

Deformations, like a twist of a barrel, are currently not introduced as an alignment parameter. To introduce such a parameter, the corresponding transformation matrices $\mathbf{C}_i$ need to be calculated. The twist is simply a common rotation correction γ for all rods within the barrel for example:

$$\mathbf{a}_{twist} = \sum_i \gamma_i$$

All deformations of composite structures which seem likely should be implemented, especially if survey information on the deformations is available.

5.5 Parametrization of Trajectories

The global linear χ^2 minimization also includes as free parameters the (local) parameters of the reconstructed objects like tracks. The initial fits are generally not linear and need to be linearized. The parametrization of the different refitted objects is described in the following subsection.

Single Track Parameterization and Derivatives Tracks of charged particles are the most commonly used reconstructed object for alignment. Their trajectories in a constant magnetic field, as in the CMS tracker, are helices. Five helix parameters and a reference surface can describe a helix. The track parameters $\boldsymbol{\tau}_j$ chosen are the

impact coordinates on a reference surface, u_p and v_p in local coordinates, the tangents $\frac{du}{dw}$ and $\frac{dv}{dw}$ in local coordinates, and the signed curvature κ.

$$\boldsymbol{\tau}_j = \begin{pmatrix} u_p \\ v_p \\ \frac{du}{dw} \\ \frac{dv}{dw} \\ \kappa \end{pmatrix} \tag{5.18}$$

Since the five helix parameters change along the track due to interaction with material a unique reference plane has to be defined, which is by default the first sensor crossed by the track. The initial track parameters τ_0 are taken from the reconstruction software of CMS. The residuals ζ in the global χ^2 minimization are the differences of measurements and the hit positions predicted by a helix propagation [45] with the initial track parameter τ_0 from the reference plane. Also the uncertainty of the propagation due to material interaction effects is propagated to the corresponding sensors [45]. This uncertainty is added to the intrinsic resolution of the sensors. The result is an effective resolution, which incorporates the effects of interaction with the material. The impact of interaction with material on the effective resolution increases with the distance and the material between the sensor and the reference surface. It can therefore be useful to chose a different reference plane than the first sensor surface in some cases.
The derivatives of the hit position on a sensor from the propagation with respect to the track parameters are also taken from the propagators documented in [45].

Parameterization of Decaying Particles If two tracks can be assumed to originate from the decay of a single particle, the tracks can be combined to a single object which is refitted within Millepede. The free parameters of the refit are the secondary vertex position, the signed momentum and the mass of the initial particle and two angles in the rest frame of the initial particle. This amounts to nine parameters in contrast to ten parameters if the tracks were refitted individually. The mass parameter can be constrained by an initial value (particle mass) and an uncertainty (width). Again, predicted hit positions, their derivatives with respect to the parameters as well as material interaction effects need to be determined. A detailed description can be found in [62].

5.6 Utilizing Linear Constraints and Presigmas

Constraints are used to define the coordinate system and to implement initial knowledge about the misalignment. Presigmas are the initial uncertainties given to individual alignment parameters. By default this uncertainty is defined with respect to the last iteration within Millepede. Hence also alignment corrections significantly larger than the presigma of an alignment parameter can still occur in the final iteration.

5.6.1 Global Coordinate System Definition

A coordinate system needs to be defined, otherwise all the tracks as well as the whole tracker could be moved and rotated without any influence on the χ^2-function. The origin of the coordinate system can be defined as the spatial center of a set of sensors. In this thesis, the center of pixel barrel sensors has been chosen. The sum of all barrel sensor translations in global coordinates is constrained to be zero. If the pixel sensor alignment parameters are defined with respect to the half barrel, then the sum of the translations of the half barrels need to be zero. The orientation is defined by the constraint that the sum of the rotation parameters of the half barrels is zero.
It is easily overlooked that when comparing the results of the alignment procedure to the simulation truth, it has to be kept in mind that the simulation truth is expressed in a different coordinate system. Therefore, the simulation truth has to be transformed into the coordinate system defined by the constraints.

5.6.2 Implementing Prior Alignment Parameter Uncertainties

An initial uncertainty can be assigned to each alignment parameter by a presigma. The given uncertainty can be understood as the mounting precision or survey precision of a sensor position. However, it is important to note that this procedure does not include correlations between the errors of alignment parameters. For example, if the sensors of a rod are displaced since the whole rod was displaced, then the displacements of the sensors are highly correlated. Applying χ^2-penalties on parameters, which represent the global displacement of the sensors would ignore this correlation. If the alignment parameters represent the sensor position with respect to the rod position, then the alignment parameter errors are not correlated and therefore no correlations are ignored. Such a parametrization has the advantage that the mounting precision is typically known with respect to a supporting structure like a rod and not with respect to a global frame, hence the alignment parameter uncertainty is known for parameters which are defined with respect to the next supporting structure. The same is also true for survey measurements, which typically measure the position of sensors within a supporting structure and not with respect to the global frame.
The presigma can be defined such, that the deviation to the alignment parameters of the previous iteration are constrained or they can be defined with respect to the initial alignment parameters. Both methods are supported in Millepede II. In this thesis the difference to the previous iteration is used.

5.6.3 Preferring Parameters of Composite Objects

An example motivates the concept of giving preference to alignment parameters of composite objects. A simple telescope could consists of two sub telescopes with three sensors each, as shown in figure 5.6. One alignment parameter is assigned to each

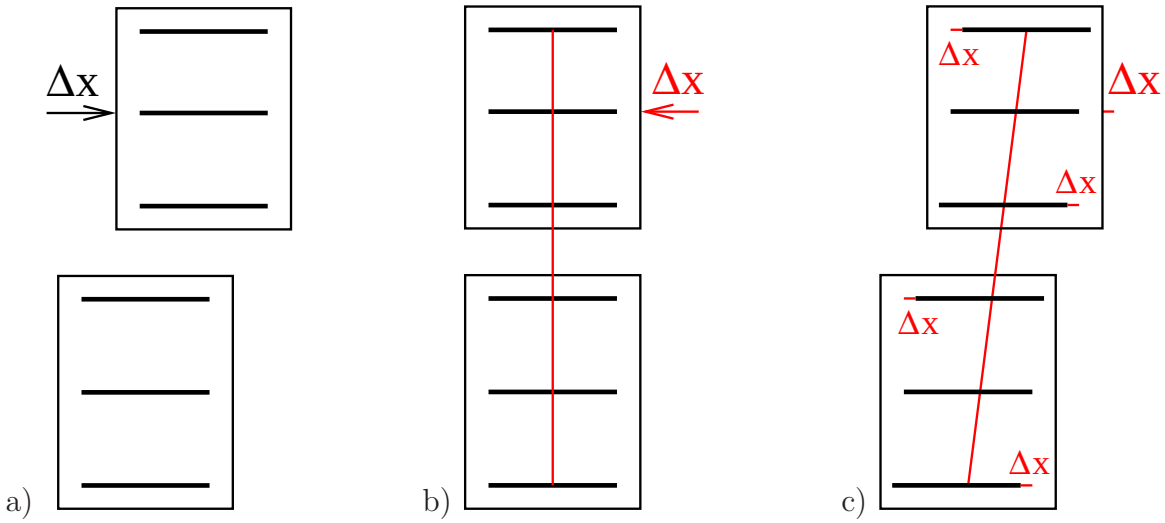

Figure 5.6: a: Illustration of misalignment of a telescope consisting of two parts. b) Resulting positions if alignment parameters of sub-telescopes are preferred. c) Resulting positions if alignment parameters of sensors are preferred.

sensor and the sensor position is defined with respect to the sub telescope. In addition, a parameter is introduced for each sub telescope. Constraints have to be used to introduce the sub telescope parameters as explained in previous sections. One sub telescope is fixed in order to constrain the transition of the whole telescope, still the shearing of the telescope cannot be determined by a track based alignment procedure using straight tracks.

If an relatively small initial uncertainty is assigned to the sensor alignment parameters, the preferred solution would be the one that can be reached using predominately the alignment parameters of the sub telescopes as illustrated in figure 5.6,b. If only small initial uncertainties are assigned to the sub telescope parameters, a solution where the sensors are moved would be preferred as is shown in figure 5.6,c.

Therefore, the deformation and translation parametrized via composite objects alignment parameters can be preferred to other deformation by reducing the initial uncertainty estimates of the subcomponents parameters.

If a relative alignment parametrization and the initial knowledge is used as described in the previous section, the preference of composite objects alignment is already present to some extent. However, the position uncertainty of a sensor with respect to a rod can be as large as 200 μm. Intrinsic deformations which would result in a small average displacement $O(10\ \mu\text{m})$ of the sensors are therefore effectively not constrained. It has to be kept in mind that each sensor position is typically determined from hundreds or thousands of measurements with a resolution of the order of 10 μm to 50 μm. The initial uncertainty is a single measurement of the order of 100 μm, hence the influence on properly determined degrees of freedoms in minimal.

When the term *preferring plausible deformation* is used in this thesis, it means that few larger structures are expected to be shifted instead of all its subcomponents in

a correlated fashion. This is done using a presigma for subcomponent parameters, which is smaller than the uncertainty estimated due to survey measurements or mechanical mounting precisions.
When using this method it becomes an important task to parametrize all deformations of composite objects which are likely to occur, such as twists and shearings. In should also be clear that preference of plausible deformations should only be applied if the χ^2 minimization does otherwise not constrain all deformations.

5.7 Symmetry Corrections to Track Parameters

Some symmetries of average track parameters can be assumed to be conserved, such as a symmetric distribution of the average transverse momentum with respect the azimuthal angle ϕ or the same average momentum distribution for positive and negative muons in the decay of Z^0s. Misalignment can distort these symmetries. As shown in section 8.1.2, the corresponding asymmetries can be measured in real data. These asymmetries can be corrected with an iterative procedure. Asymmetry corrections $\delta\boldsymbol{\tau}_{asym}$ are given to a track. The derivative of a asymmetry correction $\delta\boldsymbol{\tau}_{asym}$ for a track with respect to the corresponding local parameter (track correction parameter $\delta\boldsymbol{\tau}_j$) is obviously one. The "residuum" of the asymmetry correction is simply the correction $\delta\boldsymbol{\tau}_j$ itself. The uncertainty given to the asymmetry correction has to be roughly estimated, however it can be chosen to be rather large since the asymmetry corrections are typically added to many tracks. Given the "residuum", derivatives, and uncertainty, the asymmetry correction can be technically incorporated just like an additional measurement for the track. Different asymmetry corrections to the track parameters can be applied for each track, for example depending on the ϕ value of the track.
This could also be used to include measurements of other detector components like the muon chambers or the electromagnetic calorimeter. The difference of the track parameter measured in these components to the measurements of the tracker could be used as initial correction to the track parameters of the tracker. However, this thesis concentrates on tracker standalone calibration.
In principle the conservation of symmetries could also be introduced more directly into the χ^2 minimization, but in that case the input to Millepede would need to be changed, since the input of the Millepede[5] version used does not include the values of the track parameters, which are essential to identify asymmetries.

5.8 Simulation of Misalignment

A realistic simulation of the misalignment is the basis for all alignment studies prior to the start of the experiment. In this section, estimates on the expected misalignment

[5]The most recent (April 2007) Millepede version does support such input [67].

are given. The misalignment simulation procedure and the misalignment typically used are presented.

5.8.1 Misalignment Estimate

Given the complexity of the CMS tracker, it is obviously a challenging task to obtain realistic estimates for the expected displacements of tracker modules with respect to their nominal values. Before first data taking the misalignment of the tracker is determined by the mechanical mounting precision, survey measurements, and the information obtained from the laser alignment system.

Mounting Precision The silicon modules are built as follows: The sensors are automatically glued onto carbon frames using a precision robot (gantry). The typical mounting precision of sensors on the modules is between 10 μm and 25 μm. The relative displacement of sensors with respect to each other on a module is of the order of a few μm. The misplacement of the sensors is monitored in the production centers. This aimed precision has generally been achieved. The precision of the modules with respect to their support structures ranges from 50 μm (TEC) to 200 μm (TIB). Layers and half Barrel mounting precisions are expected to range from 100 μm to 500 μm. The outer barrel has the unique feature, that the rods are directly mounted on the half barrels. A summary of estimated position uncertainties can be found in the tables 5.4 and 5.5.

Laser Alignment System (LAS) The LAS will provide accurate information about the relative misalignment of the inner barrel (TIB) to the outer barrel (TOB) and to the end caps (TEC). The LAS can also be used to align the TEC discs with respect to each other. No information about TIB and TOB internal misalignments can be obtained from the LAS. The pixel barrel (TPB), the pixel endcaps (TPE) and the inner discs (TID) are completely out of the reach of the LAS.

Hit Position Uncertainty due to Misalignment The placement uncertainties together with the formulas presented in [47] are used to calculate the expected accuracy after the use of the LAS system. The combination of these sources of alignment information lead typically to position uncertainties in the order of 100 μm.
This level of misalignment does not jeopardize an effective pattern recognition. This is achieved by increasing the uncertainty estimates of the hit measurements on the individual sensors, reflecting the uncertainty of the sensor positions. Using this increased hit position uncertainty, the efficiency degradation for track reconstruction is negligible, as shown in [3].

hierarchy	$\Delta[\mu\text{m}]$ TEC	$\Delta[\mu\text{m}]$ TIB	$\Delta[\mu\text{m}]$ TOB
sensor vs. module	10	10	10
module vs. petal/rod	**50**-100	200	100
petal/rod vs. disc/layer	**100**-200	**100**-500	-
disc/layer vs. disc/layer	100-**500**	100-**500**	-

Table 5.4: Estimates of the position uncertainties for the silicon strip tracker before the LAS is used [46]. The highlighted numbers correspond to the more probable values.

hierarchy	$\Delta[\mu m]$ TPB	$\Delta[\mu m]$ TPE	$\Delta[\mu m]$ TID
sensor vs. module/disc blade	30 in 2D	25 in 2D	5 in 2D
module vs. ladder/ring	100	50	100 in 2D
ladder/ring vs. half disc/half layer	100	50	300
optical survey: sensor vs. half disc	-	yes 25	-
half disc/half layer vs. half barrel	100	50	400
half barrel vs. half barrel	250	300	500

Table 5.5: Estimates of the position uncertainties for the innermost detectors [46]. Uncertainties in 2D refer to uncertainties in the sensor plane.

5.8.2 Misalignment Implementation

The implementation of the misalignment includes a simulation of alignment, as well as a definition of standard misalignment scenarios.

Simulation Misalignment can be simulated within the CMS software [19]. Rather than implementing a misaligned geometry to the detector response simulation [48], it has been decided to carry out the displacements on reconstruction level. The misalignment is implemented via the transformations from the local coordinate system of the individual sensors to the global frame, effectively shifting the hit position in the global frame. Since the hits are only shifted, no hits can be removed or created in this simulation. However, given the estimated position uncertainties, only minor migrations of hits from one sensor to another sensor due to misalignment are expected. Even the sensor overlap, which is of the order of several mm, should not be significantly affected. The advantage of the misalignment at reconstruction level is the rather small amount of CPU time needed for the simulation of different misalignment scenarios. Only tracks of interest need to be refitted with the displaced hits.

Misalignment parameters The parameters representing the applied misalignment are the same as for the alignment procedure (section 5.4.2). The alignment parameters used in CMS are the six rigid body parameters. To reflect the correlated nature of misalignment, the misalignment simulation is done in hierarchies, as illustrated in figure 5.7. If a higher level structure, such as a half barrel, is shifted, all its subcomponents are shifted accordingly. Therefore, the mechanical position uncertainties of the different structures with respect to each other are reflected correctly in the simulation. Note that currently the smallest structure in the misalignment simulation are modules, which are partially composed of two sensors.

5.8.3 Misalignment Scenarios

Certain misalignment scenarios are currently used to estimate systematic uncertainties on physics analysis, but also as starting points for alignment procedures. A default misalignment also ensures a fair comparison of different alignment procedures. Three misalignment scenarios have been introduced in CMS: The *survey only* scenario, the *first data* scenario, and the *long term* scenario.

Survey Only The *survey only* scenario is based on the mechanical mounting precision and survey measurements. It is used as starting point for studies with the laser alignment system. These studies lead to estimates used in the *first data* scenario.

First Data The first data scenario assumes that LAS alignment has already been performed. The remaining uncertainties are listed in table 5.6. The misalignment is

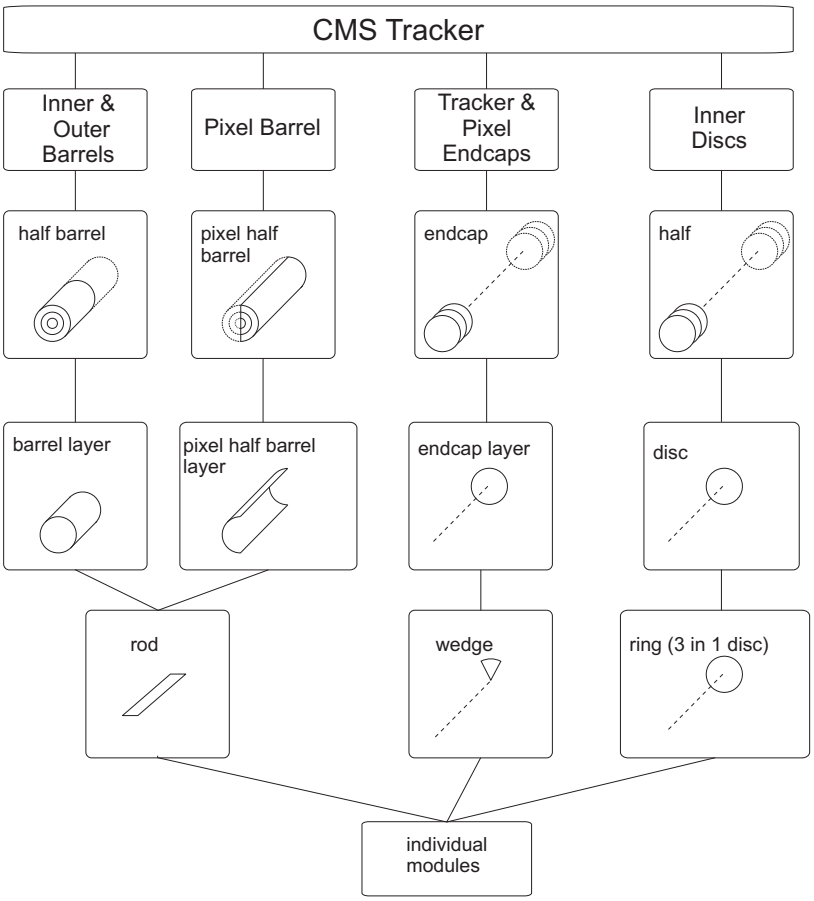

Figure 5.7: Illustration of the hierarchies used for the misalignment simulation. They closely follow the hierarchies of the mechanical structures.

hierarchy	shift	TPB	TIB	TOB
half barrel vs. global	Δx [μm]	10	105	67
	Δy [μm]	10	105	67
	Δz [μm]	10	500	500
	Δrot$_z$ [μrad]	10	90	59
ladder/rod vs. half layer/layer	Δx [μm]	5	200	100
	Δy [μm]	5	200	100
	Δz [μm]	5	200	100
modules* vs. rod/ladder	Δx [μm]	13	200	100
*only applied, if also	Δy [μm]	13	200	100
aligned to module level	Δz [μm]	13	200	100

Table 5.6: Simulated misalignment of the barrel region in the *first data* scenario [46].

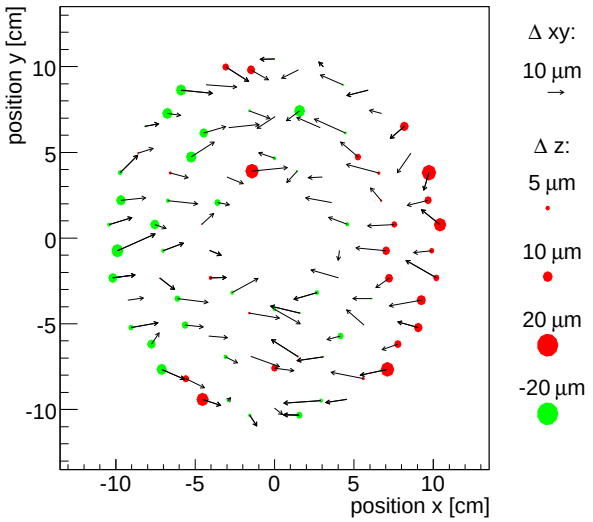

Figure 5.8: Illustration of misalignment of ladders from three layer of the pixel detector with the *first data rod level* scenario. The arrows indicate the displacements in the xy-plane. The circles illustrate the displacement in z.

diced from Gaussian distributions with widths according to the uncertainties. This is the scenario predominately used in this thesis.
In the *first data rod level* scenario the modules are not misaligned with respect to the rods. The misalignment generated for the barrel in this scenario is illustrated in figures 5.8, 5.9, and 5.10. The displacement of the rods is clearly dominated by the displacement of larger structures, as can be seen in figures 5.9 and 5.10.

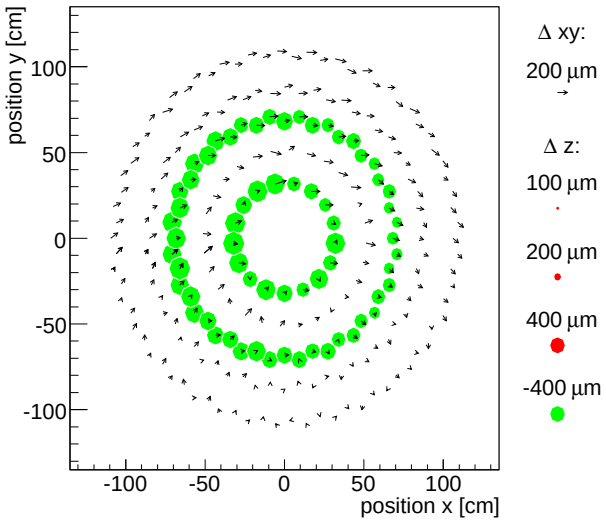

Figure 5.9: Illustration of misalignment of the rods for the barrel (+side) with the *first data rod level* scenario. The arrows indicate the displacements in the xy-plane. The circles illustrate the displacement in z. Only every other layer is plotted.

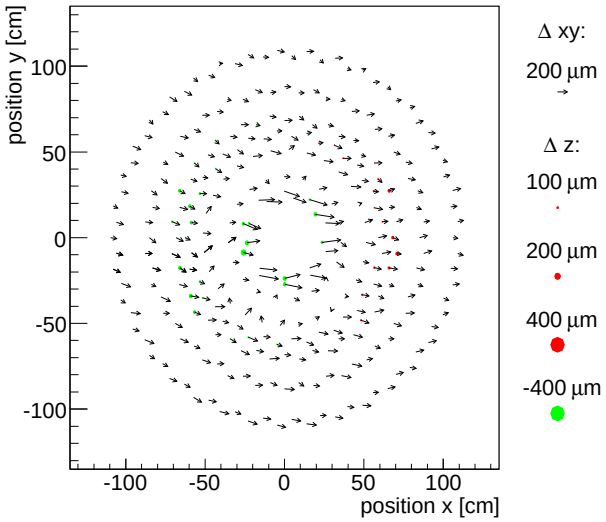

Figure 5.10: Same as in figure 5.9, but for the (-) half.

Long Term The *long term* scenario is a first guess of the remaining misalignment after taking a significant amount of data. The silicon strip modules are assumed to be an order of magnitude better aligned than in the *first data* scenario. The hierarchical structure of the misalignment and the random generation of the individual alignment parameters are the same as for the *first data* scenario. Note however, that the random generation of parameters and the hierarchical structure is realistic, only if track based alignment has not been performed yet. The misalignment remaining after a track based alignment procedure is of different nature, though, as will become clear in the course of this thesis. Results of studies with the above misalignment scenario therefore have to be interpreted with care.

Chapter 6

CMS Tracker Barrel Alignment Studies

In this chapter studies of different aspects of the alignment task are presented and the datasets used are described. These studies concern the impact of Z^0 decays, of cosmic muons, and of prior knowledge about the initial position uncertainties. All these will then be used in the alignment strategy (chapter 7) and are included also for the final results (chapter 8). In order to use all methods supported by Millepede and since a fully functioning Millepede II version was just recently available all studies were performed on rod and ladder level in the barrel region only. By default the *first data* misalignment scenario on rod level, which is described in section 5.8.2, is applied. For alignment, four alignment parameters, namely u, v, w, and γ, are assigned to two-dimensional measuring detectors. The parameter v is not aligned for one-dimensional measuring detectors. The impact of the alignment parameters α and β on the hit measurement are small for high transverse momentum tracks, which are close to perpendicular to the sensors surface in the rϕ-plane, and therefore neglected The chosen alignment parameters and their interpretation in the global frame are shown in table 6.1. By default the inversion method of Millepede was used and 5 internal iterations have been done in order to suppress the impact of outliers. Tracks with large standard deviations have been rejected. The cuts correspond to 27, 9, 5.2, 3, and 3 standard deviation for the respective iterations.

type	number	alignment parameters	corresp. global coordinates
strip half barrels	4	u, v, w, γ	x, y, z, rot$_z$
pixel half barrels	2	u, v, w, γ	x, y, z, rot$_z$
rods	1340	u, v(2D), w, γ	rϕ, z(2D), r, rot$_r$
ladders	90	u, v, w, γ	rϕ, z, r, rot$_r$

Table 6.1: Default alignment parameters used for rod and ladder alignment studies.

channel	NLO $\sigma\times$ br. ratio	Level1 + HLT efficiency	events for 1 fb^{-1}
W$\rightarrow \mu\nu$	20.3 nb	0.35	7.1 $\times 10^6$
Z$\rightarrow \mu\mu$	1.87 nb	0.65	1.2 $\times 10^6$
tt$\rightarrow \mu + X$	187 pb	0.62	1.2 $\times 10^5$

Table 6.2: Cross sections and trigger efficiencies for Z^0 and W production during nominal data taking.

6.1 $Z^0/\gamma^* \rightarrow \mu\mu$ Dataset

The $Z^0 \rightarrow \mu\mu$ decay is often called golden channel for alignment, since isolated high energy muons are produced. The high momentum and the high mass of the muons lead to very small multiple scattering. Pattern recognition and particle identification are relatively straight-forward for isolated high momentum muons.
The dataset used in order to study the impact of Z^0 events contains Drell-Yan $Z^0/\gamma^* \rightarrow \mu\mu$ events produced with the pileup expected at nominal luminosity. The invariant mass of γ^* is required to be at least 80 GeV. In figure 6.1 the invariant mass resonance at the Z^0 mass is shown. The most probable value for the transverse momentum of the Z^0 is about 8 GeV as can be seen in figure 6.1 b. Since the resonant production of the Z^0 is dominating the cross-section, the dataset is called the Z^0 dataset in the following.
Each track is required to have at least 8 measurements within the barrel region (aligned region) and a transverse momentum of more than 15 GeV. All measurements of detectors which are not aligned are generally ignored in the alignment procedure. The transverse momentum distribution of the reconstructed muons is shown in figure 6.1 c. Some muons have a transverse momentum far above 45 GeV which is predominately due to the fact that the transverse momentum of the Z^0 can be large. The distributions shown are filled with the parameters of tracks which only use tracker information for reconstruction. However, at these transverse momenta this does not affect the resolution.
At nominal luminosity (10^{34} cm^{2}s^{-1}) the rate is about 20k recorded Z^0 decaying into a muon pair per day and about 100k W decaying to a muon and a neutrino. The cross sections and the trigger efficiencies expected are summarized in table 6.2.

6.2 Cosmic Muons

To study the impact of cosmic muons on the alignment procedure, two cosmic muon samples have been generated. Generation, detector response simulation, and reconstruction are modified with respect to the default simulation and reconstruction which is tuned to *pp* collision data.

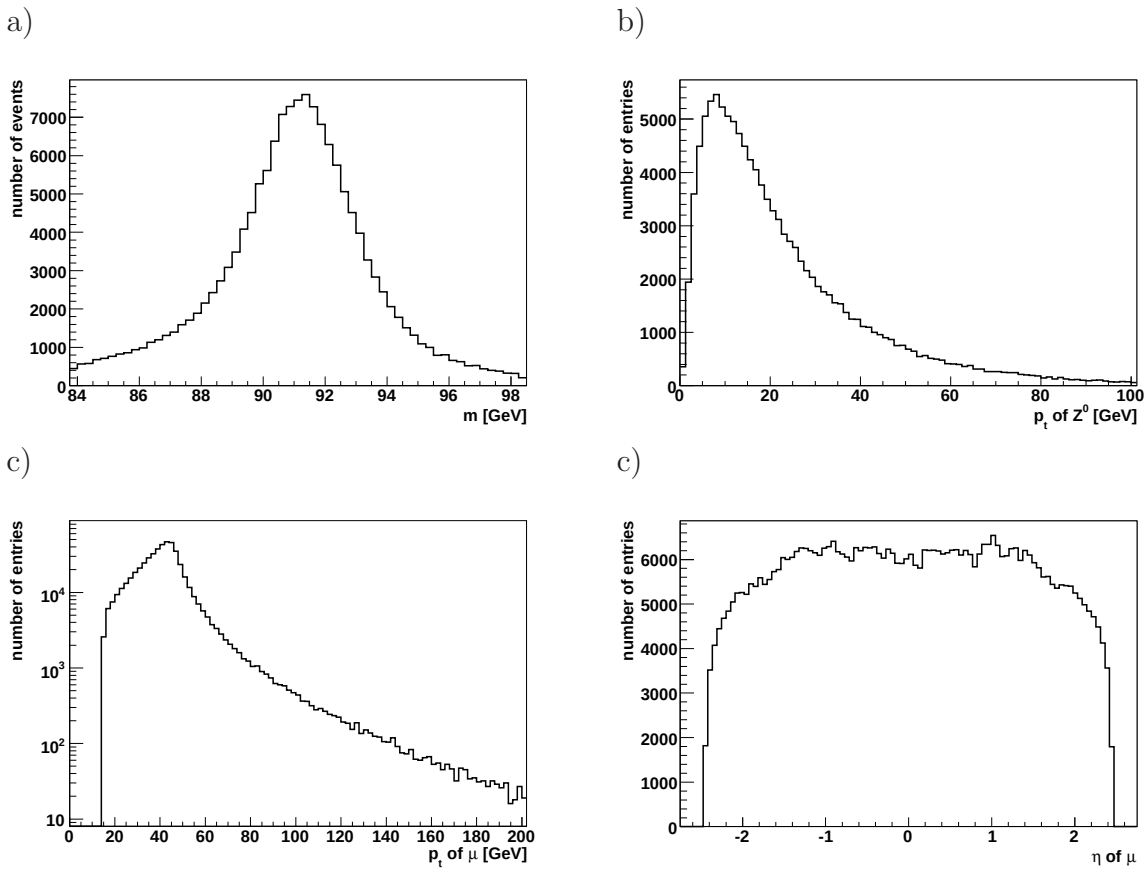

Figure 6.1: Distributions for 500k Z^0 events. a: Invariant mass distribution of the mouns pair closest to the Z^0 mass, b: transverse momentum distribution of the Z^0. The Z^0s are selected by a mass cut on the muon pair mass of $\pm$ 5 GeV around the nominal Z^0 mass. c: Transverse momentum distribution of the muons, and d: η distribution of the muons.

6.2.1 Rates and Generation

The generation of the cosmic muon Monte Carlo data sample is done with a modified version of the cosmic muon generator[1] [51].

Generation The generation splits into two parts. In the first step, cosmic muons are generated on the surface of the earth according to approximate functions, obtained from rate measurements described in [53]. The rate is determined to depend on energy with $\sim E^{-2.7}$, the angular dependence can be described by $\cos^2(\alpha)$, where α is the angle with respect to the vertical axis, and the charge dependency of the cosmic rays leads to 20% more μ^+ than μ^-.
In the second step, the muons are propagated to the CMS detector inside the cavern about 100 m below the surface. The energy loss of muons in the ground is simulated, applying different densities for rock and reinforced concrete and taking the geometry of the cavern and supply core into account. An additional filter has been implemented, which allows to select the events which cross a certain volume within the CMS detector. The generation is rather CPU time intensive, since the vast majority of the cosmic muons generated on the surface does not reach the CMS detector.

Sample Definitions and Rates Two different data samples have been produced. Both datasets are generated with the same magnetic field of 4 Tesla as it will be used for collision data taking. Only cosmic muons penetrating the barrel region were generated, since reconstruction in the tracker end caps is not feasible for vertical tracks.
One data sample reflects a brief period of cosmic data taking of less than one day. Soft cuts on the minimal energy and distance to the beam line have been applied in order to be able to study the impact of variation of these cuts. All muons penetrate the barrel region of the tracker and have a minimum energy of 10 GeV. The rate of such cosmic muons is 32 Hz. Therefore, the one million events that have been generated correspond to $\sim$ 9 h of data taking.
The second dataset simulates a longer period of cosmic data taking. The cuts were tightened, based on the experience of studies with the first data set. The minimal energy has been chosen to be 50 GeV. The tracks are required to cross a volume defined by a box 1 m above the beam line, the height of the box is 20 cm, the length is 60 cm, and the width is 30 cm. All tracks must have an angle to the vertical of 15° or less. For this sample, material interaction effects are reduced due to the high energies of the cosmic muons and many of the tracks traverse the precisely measuring pixel detector. The rate of cosmic muons in compliance with these criteria is 0.016 Hz. 25k events were generated, which correspond to 18 days of cosmic data taking. The cuts and and data accumulation times are summarized in table 6.3.

[1] From the generator interface package CMKIN (version 4_3_1) [52].

cosmic sample	low energy	high energy
events	1 mio.	25k
accumulation time	$\sim$ 9 h	$\sim$ 18 days
energy [GeV] at surface	$10 < E < 5000$	$50 < E < 5000$
angle to vertical α	$\alpha < \|60°\|$	$\alpha < \|15°\|$
selection volume	$\|z_{cylinder}\| < 1$ m $r_{cylinder} < 1$ m	$\|z_{box}\| < 0.3$ m $\|x_{box}\| < 0.15$ m 1 m $< y_{boy} <$ 1.2 m

Table 6.3: Applied cuts at the generator level and the resulting accumulation time for different cosmic muon data samples.

Event Topologies The kinematics of the cosmic muons arriving at the CMS detectors are largely affected by the geometric properties of the cavern and the supply tube. The supply tube is located at z = 14 m and has a radius of 10 m. Therefore asymmetries of distributions are expected. Figure 6.2 shows the generated θ and ϕ distributions for 100k events of the low energy cosmic muon sample. The angles are calculated at the point of closest distance to the beam line. In θ two peaks are visible, one at 90° and one at about 105°. The peak at 90° is due to high energy muons penetrating the soil between the detector and the surface. Their most probable direction is vertical. The other peak at 105° is due to the fact that the access tube is located in this direction. Therefore, also cosmic muons with less energy originate from there. The ϕ of the incoming cosmic muons is quite symmetric and peaks at -90°, which corresponds to vertical tracks in the xy-plane. The asymmetry of the charges produces a slight asymmetry in ϕ, since the trajectories have opposite curvature. However the muons have a minimal energy of 10 GeV and hence the difference in ϕ between the incoming cosmic and the cosmic at the closest distance to the beam line is small. The distribution of the incoming cosmic muon tracks is exactly symmetric, since the center of the supply tube is zero in the x-coordinate.
The transverse momentum spectrum of the cosmic muons is shown in Figure 6.3. The generation cut at E = 10 GeV is clearly visible, however the θ distribution and material effects lead to cosmic muons with less than 10 GeV transverse momentum. Figures 6.4 (left) shows the z position of the muon at its point of closest approach to the beam line. The rather rectangular shape is caused by the demand that the cosmic muons have to cross a cylinder ranging from -100 cm to 100 cm in z. The asymmetry is due to the position of the access tube at positive z.
The number of generated hits, shown in figure 6.4 (right), varies significantly, since it depends on the distance to the beam line of the track. For stereo strip modules two hits are simulated, one hit for each sensor on the module.

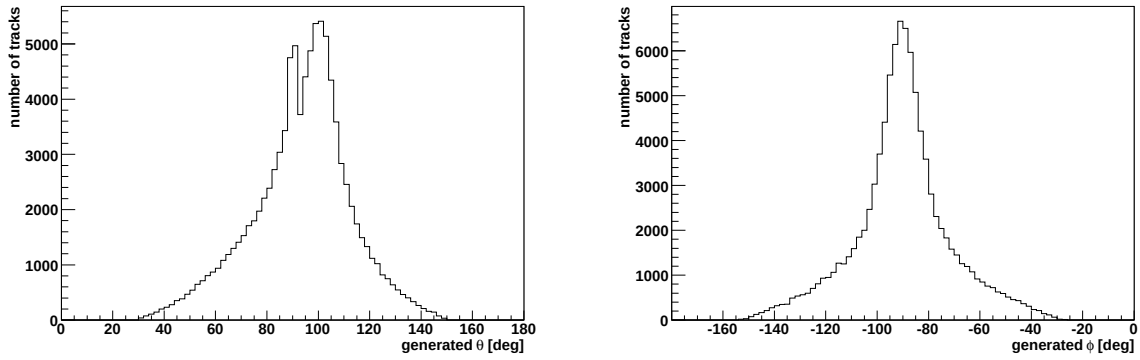

Figure 6.2: Generated cosmic tracks, no trigger efficiency is applied. Left: θ distribution. Right: ϕ distribution.

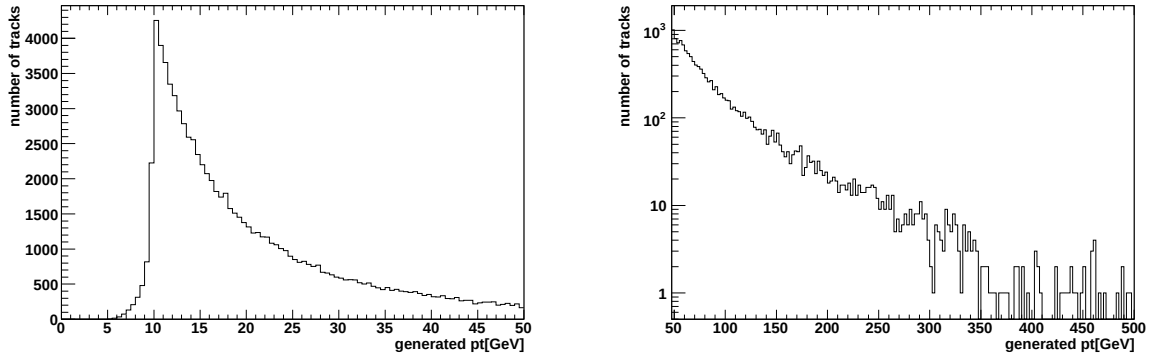

Figure 6.3: Generated cosmic muons, no trigger efficiency is applied.. Left: P_t distribution for small values. Right: P_t distribution for large values.

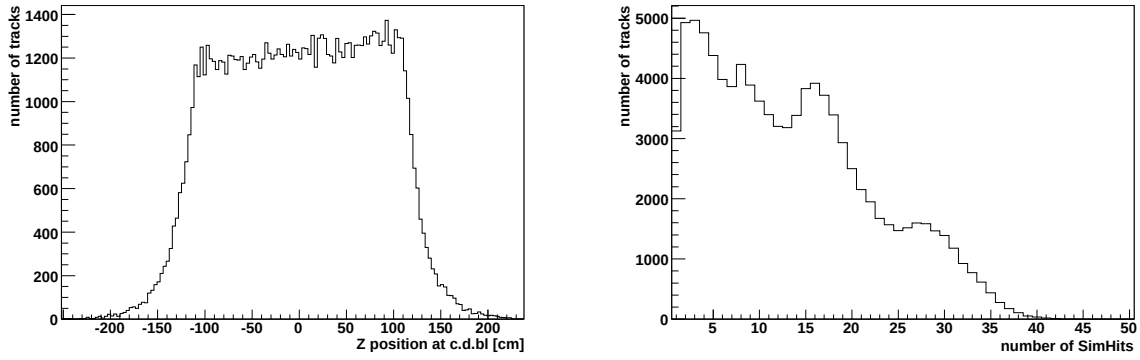

Figure 6.4: Generated cosmic muons, no trigger efficiency is applied.. Left: z position at the point of the closest distance to the beam line. Right: Number of simulated hits.

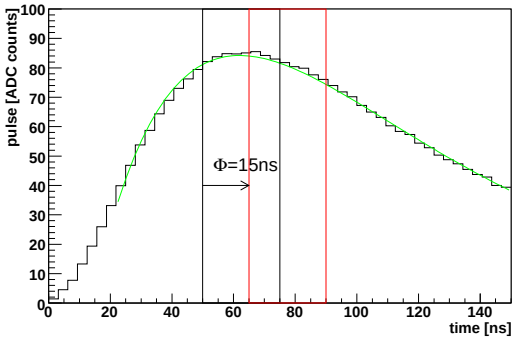

Figure 6.5: Pulse height versus time. The boxes illustrate the timing uncertainty due to the trigger and the arrow the global phase shift.

6.2.2 Detector Response Simulation for cosmic muons

The detector response simulation is done in two steps. First the GEANT4 [56] based package OSCAR [48] (version 3_6_5) simulates the material interaction and energy deposition. In the second step, the CMS reconstruction software ORCA (version 8_13_3) simulates the response of the detectors up to the digital level. Signals due to noise are also included in this step.

Special Detector Settings Cosmic muons are an exotic dataset, demanding special settings for the readout electronics and synchronization of the detectors. The width of a strip detector signal is 25 ns in deconvolution mode (see also section 4.5), which is used by default. However, the trigger signals of cosmic muons are flatly distributed within the 25 ns of the LHC clock. Therefore, the peak mode option which has a signal length of more than 50 ns (fig 6.5), is used.
In addition to the jitter of the trigger, the cosmic muons transverse the CMS detector from a different direction than particles originating from pp collision data. Given the size of the CMS detector this demands a new synchronization of the different detector components with respect to each other. Each silicon detector can be given a different offset in time with respect to the LHC clock. Normally, this is the time required by a particle with the speed of light to travel from the nominal interaction point to the detector. For the reconstruction of tracks from cosmic muons this has to be changed. The reference distance is changed to the distance to a horizontal plane at a height of 8 m above the CMS detector center. This is a natural reference plane, since it is approximately at the beginning of the muon chambers.
For fine tuning, an additional global time offset Φ has been introduced to all silicon detectors. This phase is varied in steps of 5 ns and the hit reconstruction efficiency as well as the signal to noise ratio is determined for different values. The signal to noise ratios are normalized to perpendicular tracks by applying a factor of $\cos(\phi_{local})$,

Φ [ns]	mode	S/N	ϵ [%]
0	peak	9.73	97.9
5	peak	9.81	98.0
10	peak	9.71	98.0
15	peak	9.77	98.3
20	peak	9.7	97.2
0	dec	8.53	86.2

Table 6.4: Signal to noise ratio and hit reconstruction efficiency ϵ in dependence of the applied common shift Φ.

where ϕ_{local} is the angle between the normal and the track. The signal to noise ratio is defined as in section 4.7.1 and the efficiency is the ratio of the simulated and reconstructed hits. Table 6.4 summarizes the results. The jitter of the trigger leads to the effect that the average signal to noise ratio and the efficiency do not have to be optimal for the same phase Φ. As a result, all phases between 5 ns and 15 ns are equally good and a 10 ns shift is chosen for the response simulation. The output of this simulation is the digital response of the detectors in ADC counts.

6.2.3 Reconstruction

The track reconstruction can be split into two basic parts, the hit position reconstruction and the merging of these hits into tracks. The default hit and track reconstruction has to be modified in order to reconstruct the trajectories of cosmic muons.

Hit Reconstruction

The main characteristics of cosmic tracks concerning the hit reconstruction are their large inclination angles with respect to the normal of the sensor surface. This is especially true for the projection onto the xy-plane, in which tracks of high energy particles from the interaction point are always close to normal (figure 6.6). Hence the default hit reconstruction has to be optimized for such characteristics.

Pixel Hits The hit position of a cluster in a pixel sensor is determined from the charges on the edge channels of the cluster [16]. This algorithm is often called head-to-tails algorithm. Large capacitive coupling between the channels, as it is the case for strip sensors, would decrease the resolution of this algorithm significantly, since the measurements of the edge strips can be dominated by cross talk from their neighbors. However, since capacitive coupling of neighboring pixels is small this algorithm is suitable for the pixel sensors. The hit positions p_{hit} are computed as follows:

$$p_{hit} = p_c + \frac{q_{last} - q_{first}}{2(q_{last} + q_{first})}|W_x - (n_x - 2)p_x| - \frac{1}{2}\text{lorentzshift},$$

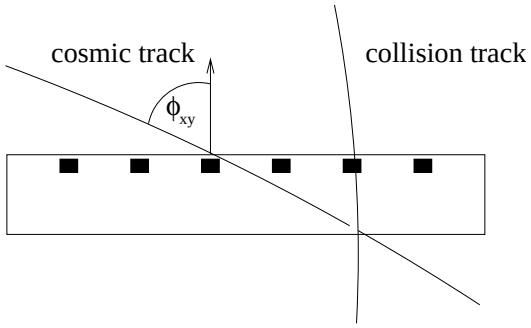

Figure 6.6: Illustration of typical cosmic muon track and high transverse momentum track from the interaction point. The angle ϕ_{xy} between the sensor normal and the track direction in the xy-plane can become large for cosmics.

where p_c is the geometrical center of the pixels, p_x is the pixel pitch in x, q_{last} and q_{first} are the measurements on the last and the first pixel, W_x is the expected trajectory length within the sensors along the measured coordinate and n_x the number of pixels within the cluster. The factor $\frac{1}{2}$ in front of the expected Lorentz shift is due to the definition of the hit position, which is the position in the middle of the sensor material.
The parameter used to estimate the hit position uncertainty for a coordinate is the inclination angle with respect to the corresponding coordinate. The angle can be determined from the cluster itself or from additional track information. Figure 6.7 shows the pulls of the pixel hit position measurements for both coordinates and both methods to determine the inclination angle. The pull distribution of the global z measurement is approximately described by a centered Gaussian with the width of about one. The θ angle of cosmic muon tracks (figure 6.2) is not generally larger than for tracks from pp collision tracks, hence the z-measurement is not more demanding for cosmics than for other tracks.
However, the precision of measurement uncertainties in the global $r\phi$ coordinate is affected by the large absolute values of angle ϕ_{xy}. The sizable amount of data with a deviation of more than five σ could distort the alignment procedures. Such effects are reduced by outlier rejection or down weighting of outliers, as described in section 5.3.5. In figure 6.8 the resolution of hits can be seen. The root-mean-square of the $r\phi$ coordinate residuum is much larger (28.7 μm), than for hits from tracks from the interaction point, where it is about 10 μm. The residual width in the z coordinate is similar to the one with tracks from pp collisions.

Silicon Strip Hits The hit reconstruction algorithm used is described in the test beam section 4.7.1. For wide clusters (containing at least 4 strips) the head-to-tail algorithm described in the previous paragraph is used. The estimated hit resolution

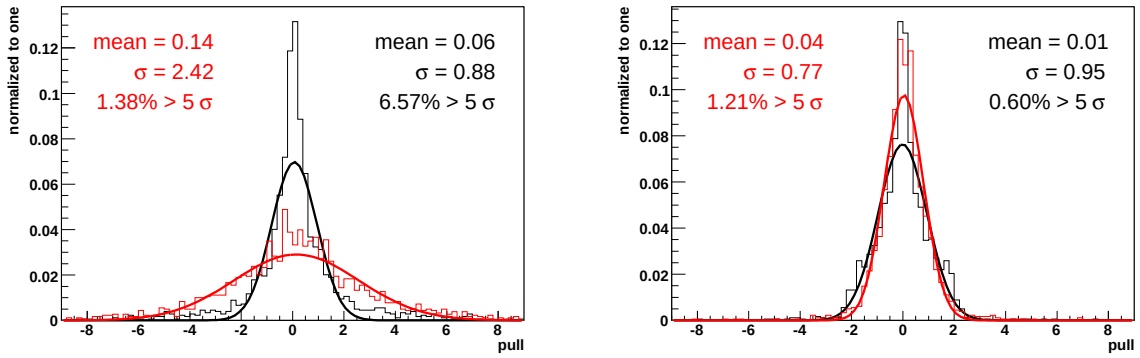

Figure 6.7: Pull distribution of the pixel measurements for the $r\phi$ coordinate (left) and the z coordinate (right). Black: hit position estimated using the inclination angle of the track. Red: Standalone calculation of the hit position.

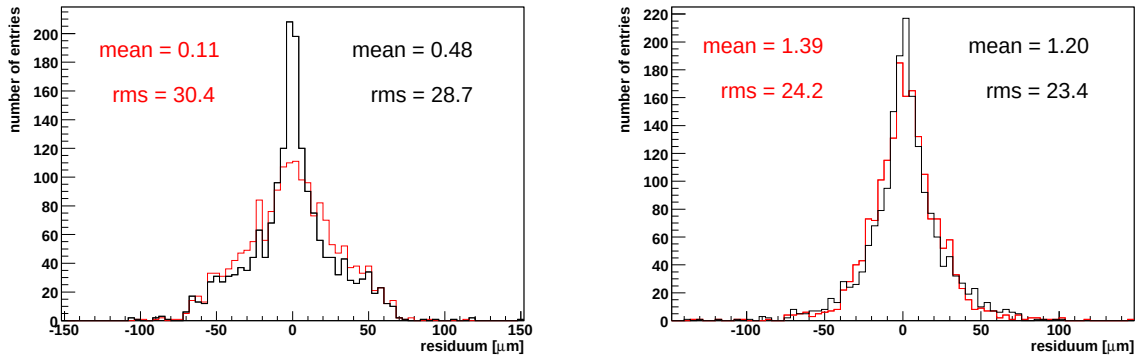

Figure 6.8: Residuals of the hit position measurements of pixel sensors for the $r\phi$ coordinate (left) and the z coordinate (right). Black: hit position estimated using the inclination angle of the track. Red: Standalone calculation of the hit position.

is parametrized as a function of the length transversed by the track in perpendicular direction to the strips of the sensor. The compatibility of the expected cluster size with the measured cluster size, and the compatibility of the expected hit position with the measurement are taken into account as well [69]. This parametrized uncertainty estimation is not the default option, since a simpler estimation results in similar estimates for high energy tracks from the interaction point. Figure 6.9 shows the ratio of the residual of the hit position and the estimated hit position uncertainty (pull). Illustrations 6.9 a and b demonstrate the good uncertainty estimation for single sided silicon strip modules. The parametrized error estimate is better: The width of the pull is one and the mean zero. As expected, the pull distribution is close to a Gaussian function. This holds also true for large inclination angles ϕ_{xy}.

For the double sided stereo modules, only the diagonal elements of the covariance matrix have been taken into account. This is done on purpose, since the measurements of each coordinate are given to the alignment algorithm Millepede as uncorrelated measurements. The pulls for the stereo modules look reasonably Gaussian and centered, but tend to be slightly too small. In addition to the uncertainty of the hit measurements, the uncertainty in the direction of the trajectory amounts to an error of the measurements for stereo modules. The two independent hit measurements of the strip sensors are combined with the track information to give the final hit positions on the modules. Again, the precision of the uncertainty estimation decreases with an increase of the inclination angle $|\phi_{xy}|$.

Overall, the hit reconstruction and error estimation of cosmic hits is sufficient for first studies of the impact of the cosmic muons on the alignment procedure. However further optimization of the hit reconstruction would be desirable on the long term.

Track Reconstruction

The track reconstruction can be divided into two parts, the seeding and pattern recognition which determine the hits belonging to a track and, secondly, the final fitting and smoothing of the track. Pattern recognition should not be a critical subject for cosmics, since in most cases only a single track appears in cosmic data. The combinatorics are therefore much simpler than for events from *pp* collisions. Nevertheless, an efficient procedure for this task is not yet implemented in the reconstruction framework ORCA. To avoid data loss due to a premature procedure, an idealized procedure is used in this thesis: Simulation information is used to assign the correct hits to a track. Afterward the Combinatorial Kalman Filter (CKF) is used for the fitting of the tracks. The resulting track finding efficiency is high, with more than 98% for tracks with more than 20 hits on sensors as shown in figure 6.10.
For the determination of the input to Millepede a reference plane has to be defined for each track. The further the sensor measurement is apart from that plane, the worse is the effective resolution (section 5.5). For symmetry reasons, each track is used twice,

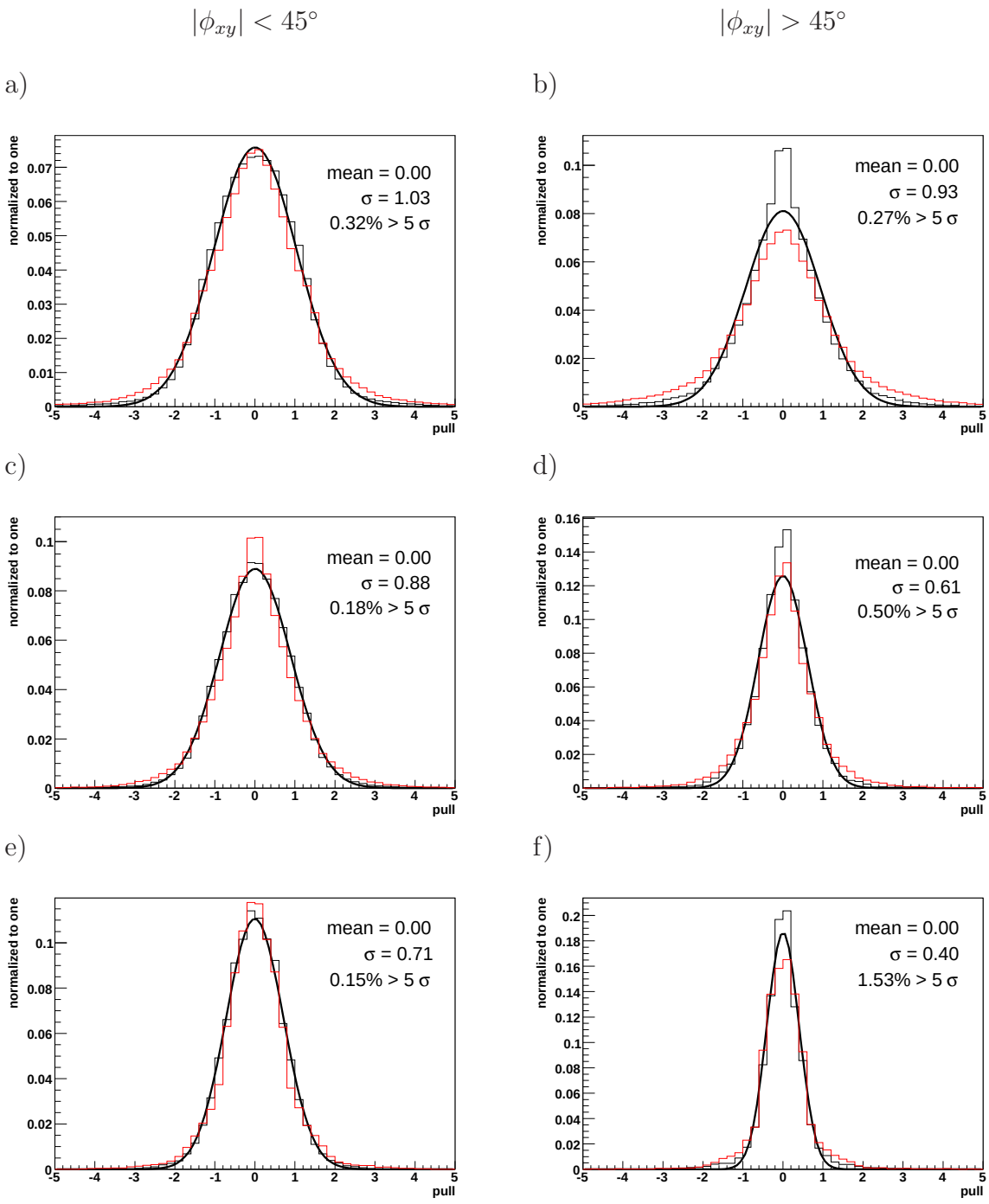

Figure 6.9: Pull distributions of reconstructed hit positions. Left: Track inclination angle $|\phi_{xy}|$ (figure 6.6) smaller than 45°. Right: $|\phi_{xy}|$ larger than 45°. Black: Special uncertainty estimation. Red: Default uncertainty estimation. Distributions are shown for single sided strip modules (a,b), for the $r\phi$ coordinate measurements of double sided stereo modules (c,d), and for the z coordinate measurements of double sided stereo modules (e,f).

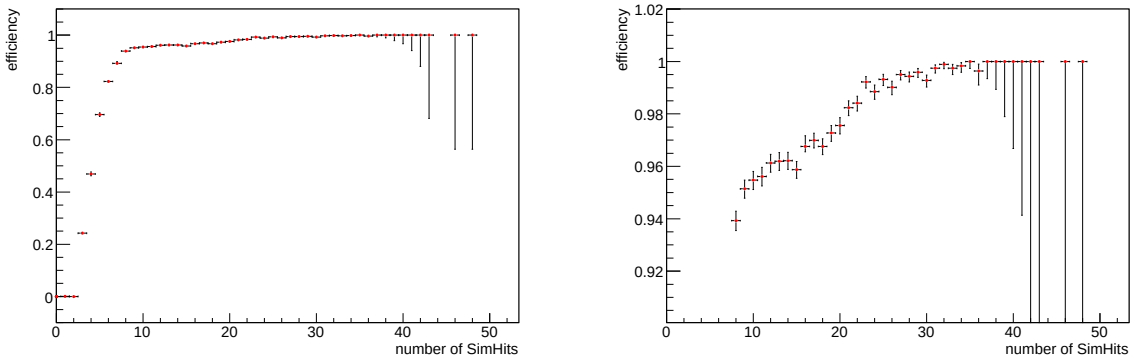

Figure 6.10: Track reconstruction efficiency. Left: Efficiency vs. number of simulated hits. Right: As left, zoomed into high efficiencies. The uncertainties are calculated using Bayesian statistics, to avoid unphysical errors when using binomial errors, if all simulated tracks are reconstructed [68].

once the surface of the first sensor serves as reference and once the surface of the last sensor.

6.3 χ^2 Invariant Deformations

Alignment procedures are generally based on the minimization of the overall χ^2 of the trajectory fits. However, some deformation of the tracker do not increase the overall χ^2, although they change the parameters of the trajectories. In more mathematical terms: The result of the χ^2 minimization can be a sub-vector-space of the alignment parameter vector-space instead of a unique solution. In this chapter χ^2 invariant deformations are identified and classified, beginning with the χ^2 invariant deformations of a telescope-like structure and then extending this to the CMS tracker barrel.

6.3.1 Deformations of a Telescope

Understanding the χ^2 invariant deformations for a telescope is useful to generally understand and classify typical deformations. First the deformations for straight line tracks are discussed and afterward additional deformations due to a helix track model are explained.

Straight Tracks Any linear transformation will conserve the linearity of a straight track and hence linear transformations represent χ^2 invariant deformations. A linear transformation from a three dimensional vector $\mathbf{x}$ to a three dimensional vector $\mathbf{x}'$ can be represented by a matrix $\mathbf{M}$ and vector $\mathbf{c}$:

$$\mathbf{M}\mathbf{x} + \mathbf{c} = \mathbf{x}'$$

The vector $\mathbf{c}$ and the invertible matrix $\mathbf{M}$ together have 12 free parameters, which can be assigned to the following transformations:

- 3 **translations** which define the position of the telescope.
- 3 **rotations** which define the orientation of the telescope.
- 3 **scales** which lead to an **expansion** or **shrinking** of the telescope along the corresponding axis.
- 3 **tilts** or non orthogonalities of the axes, which lead to a **shearing** of the telescope.

The position and orientation of the telescope need to be defined and therefore the translations and rotations are not regarded as χ^2 invariant deformations. Generally six corresponding constraints have to be applied to define the coordinate system.

Curved Tracks If tracks are fitted with a helix model, an additional χ^2 invariant deformation is introduced:

- **bending** of the telescope, which changes the curvature of all tracks.

This deformation can be approximated by a quadratic function in r, where r is the distance to the first sensor of the telescope.

In conclusion, for an individual telescope shearings, expansions, shrinkings, and bending are the deformations remaining undefined, if a χ^2 minimization is used as alignment procedure.

6.3.2 Deformations of the Tracker Barrel

The basic deformations identified in the previous section can also be applied to the full tracker geometry. To some extend the tracker can be understood as a combination of many telescope like substructures which point to the nominal interaction point. This picture, in combination with the known deformations of the telescopes, is used to identify possible χ^2 invariant deformations of the tracker.
In addition it is verified that the identified deformations are truly invariants of the χ^2 minimization problem. The matrix representing the linear equation system, which needs to be solved for the minimization, can be diagonalized. The eigenvectors and eigenvalues have a physical meaning: Deformations along the eigenvectors with the smallest eigenvalues are least sensitive to the χ^2 minimization. These eigenvectors are then compared to the possible χ^2 invariant deformations identified previously.
This method was used for the tracker barrel with the alignment parameters of rods and ladders. The chosen alignment parameters per rod (ladder) were the three translations and the rotation parameter γ. The translation parameter v was not aligned for rods without stereo modules. Muons from one million $Z^0 \rightarrow \mu\mu$ events were used.
If diagonalization is used, the geometry has to be simplified by aligning on rod level, since diagonalizing is rather CPU intensive. Diagonalizing large matrices requires the extensive use of computer clusters and special algorithms [70].

Shearing and Bending The shearings and bendings lead to the deformations shown in figure 6.11 a and b. Since the magnetic field is parallel to the z-axis, the bending induced by magnetic forces can only occur in the rϕ-plane. The shearing and bending can be described by the functions of the mean displacement of all sensors, $\langle \Delta r\phi \rangle$ and $\langle \Delta z \rangle$, in dependence of the radius r of the detector positions:

$$\langle \Delta r\phi \rangle(r) = p_0 + p_1 r + p_2 r^2 \quad \langle \Delta z \rangle(r) = z_0 + z_1 r \tag{6.1}$$

Fitting this function to the misalignment remaining after a χ^2 minimization shows convincingly that the bending deformation is described by the functions defined, as

a) sheering (red) and bending (green) in rϕ:

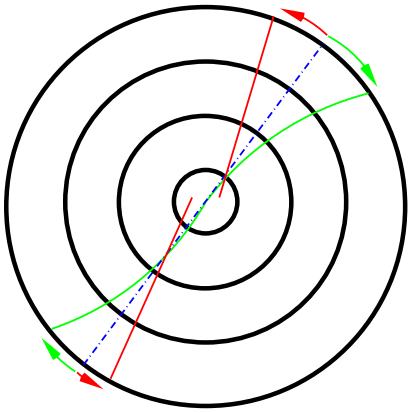

b) sheering in z:

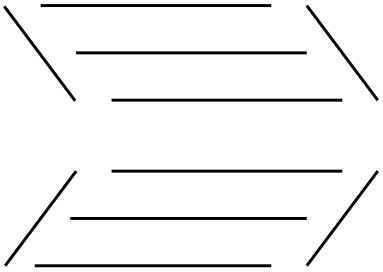

c) r-rϕ mode 1 (or sheering in x):

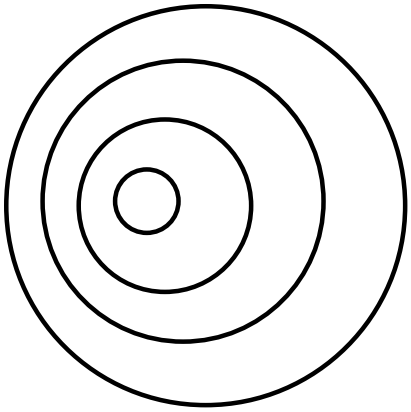

d) r-rϕ mode 2:

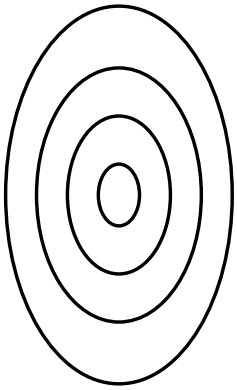

e) twist of barrel:

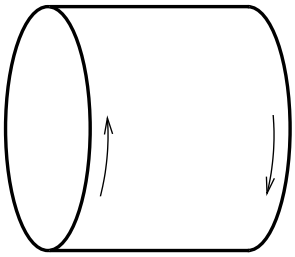

Figure 6.11: Schematic illustration of the χ^2 invariant deformations.

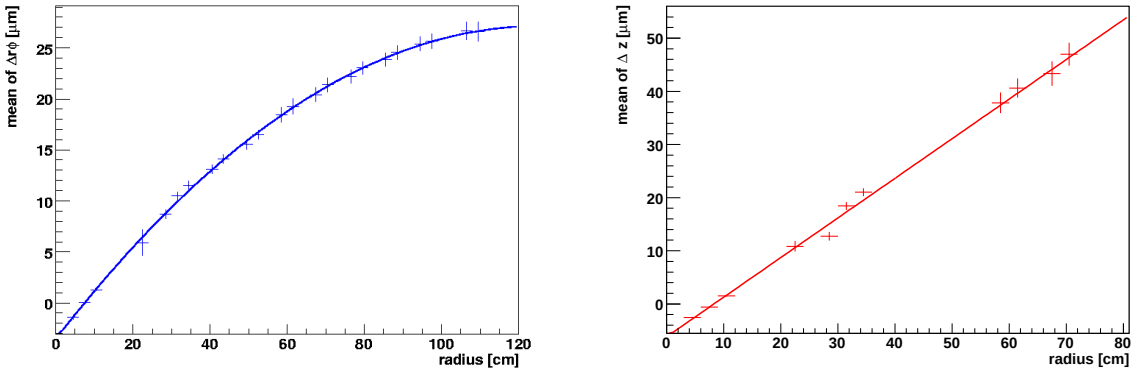

Figure 6.12: Fits of deformation functions 6.1 to the remaining displacements after a χ^2 minimization procedure (see section 6.4). Left: Fit of the deformation function to $\langle \Delta r\phi \rangle(r)$. Right: Fit of a shearing deformation function to $\langle \Delta z \rangle(r)$.

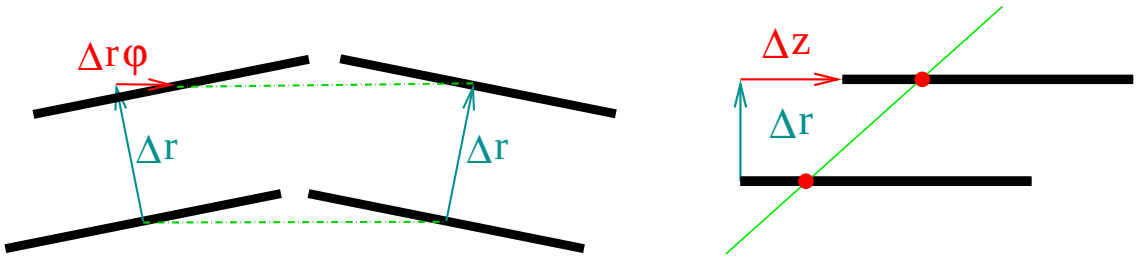

Figure 6.13: Left: Shifts of Δr require a shift in $\Delta r\phi$ to keep the distance between the sensors (green dotted line) constant. Right: Shift of Δr requires shift of Δz to keep the expected hit position on the sensor surface (red dot) constant.

can be seen in figure 6.12.
The amplitude of the shearing and the bending in rϕ can also vary along the z coordinate, leading to a twist of the barrel (see figure 6.11 e). The twist as well as the shearing in z were identified via the diagonalization. Figure 6.15 shows the deformation generated by the eigenvector with the smallest eigenvalue. It can clearly be identified as a twist. The deformation along the z-axis due to the same eigenvector is a shearing in z, as can be seen in figure 6.16.

r-rϕ oscillation The expansion and shrinking described in the telescope-section are constraint to some extent by the scale given by the exactly known size of the sensors. The distance in rϕ between neighboring sensors is well defined, since many tracks crossing one of the neighboring sensors are crossing the same sensors in front of and the same sensors behind the neighboring pair. Increasing the distance in rϕ between the neighboring sensors would therefore require to increase the size of the sensors in front of and behind the pair. Therefore, an overall expansion of the tracker does significantly increase the average χ^2 of the track fits.

However, an expansion of Δr along the r coordinate does increase the distance of the neighboring sensors by an amount $\Delta r\phi$. The resulting difference $\Delta r\phi$ is proportional to Δr and needs to be compensated in order to keep the rϕ-distance constant, as illustrated in figure 6.13 (left). In terms of shrinking and expansion this means that the expansion along r leads to a shrinking along rϕ.
In addition, the translation along the z coordinate of the sensors couples to the translation in r, at least if the dataset consists predominantly of tracks originating from the vertex. In that case, the inclination angle in the rz-plane is roughly the same for all tracks. The predicted hit positions on the sensor surface are therefore not significantly changed if the sensors are moved along the average track direction in the rz-plane, as shown in figure 6.13 (right).
The oscillation of the n^{th} mode can be described as follows:

$$\Delta r(\phi) \sim \cos(n\phi + \alpha) \quad \Delta r\phi(\phi) \sim \sin(n\phi + \alpha) \quad \Delta z(\phi) \sim \cos(n\phi + \alpha) \tag{6.2}$$

where α is an constant shift. Each mode n occurs twice, once with a symmetric function $\Delta r(\phi)$ ($\alpha = \alpha_s$) and once with an asymmetric function ($\alpha = \alpha_s + 90°/n$).
A schematic illustration of the first and second mode can be found in figure 6.11 c and d. As expected, these modes were among the eigenvectors with the smallest eigenvalues. The eigenvectors of the first, second and third mode are illustrated in figures 6.17, 6.18 and 6.19, respectively. Further higher modes are illustrated in appendix C.3. The $\Delta r\phi(\phi)$, $\Delta r(\phi)$ and $\Delta z(\phi)$ functions of the eigenvectors were compared to the expected oscillations. Figure 6.14 shows the fit of the corresponding functions to the displacement of rods on the fifth layer corresponding to an eigenvector identified as the second mode oscillation. This fit shows convincingly that the eigenvectors do correspond to these deformations. The amplitude of the oscillation as a function of the rod position radii can be seen in figure 6.14.

In conclusion, comparing the deformations corresponding to the eigenvectors to the deformations corresponding to the classifications lead to the result that all eigenvectors with small eigenvalues could be assigned to one of the deformations shown in figures 6.11 or a higher mode of them. χ^2 invariant deformations are a core problem of alignment procedures.

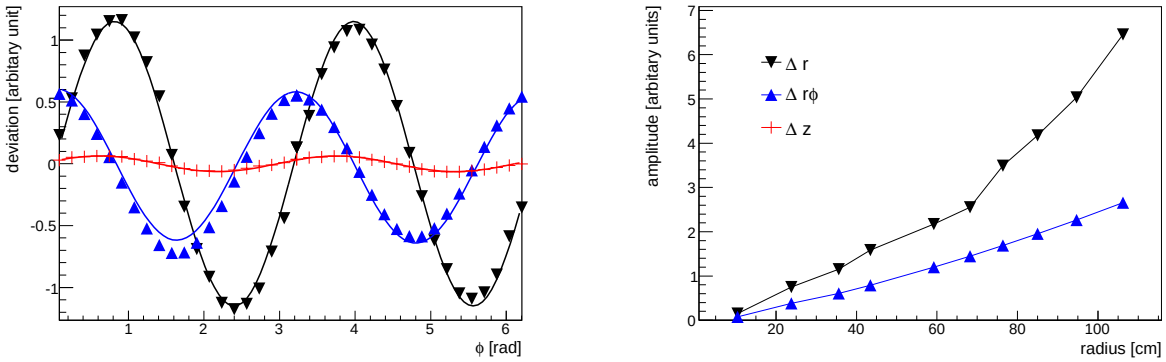

Figure 6.14: Left: Displacements in r, rϕ, and z of rod positions in the fifth layer as a function of ϕ. The displacements correspond to a χ^2 invariant eigenvector. A r-rϕ oscillation (equation 6.2) is fitted to the displacements. Right: Amplitudes derived from fits of the oscillation in dependence of the radius of the layer.

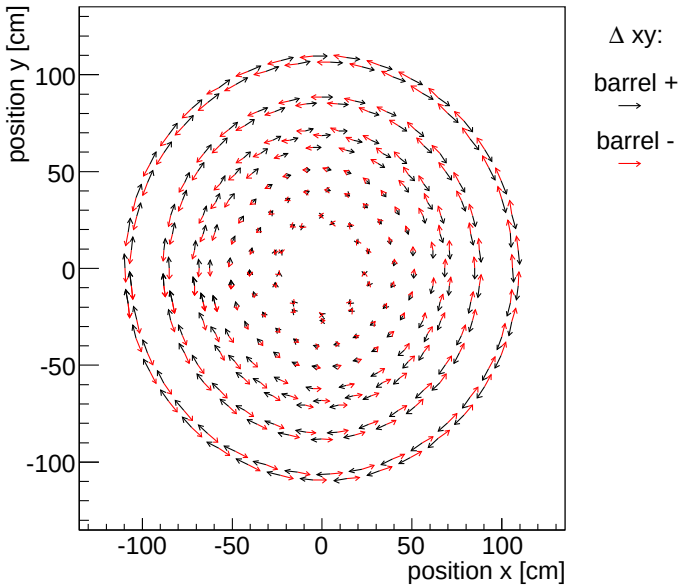

Figure 6.15: Illustration of the eigenvector of the barrel twist. The arrows indicate the displacement of a subset of rods. The arrow origins represents the position of the corresponding rod in the xy-plane.

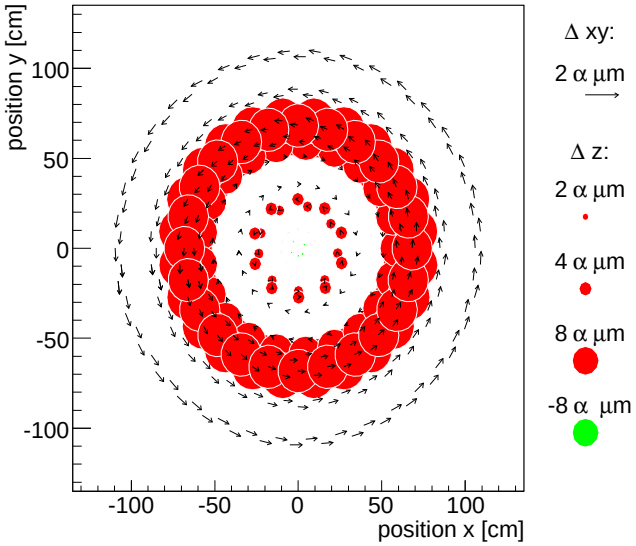

Figure 6.16: Illustration of the eigenvector of the shearing in z. The radii of the circles represent the displacement in the z coordinate for the 2D detectors only. The colors decode the sign of the z displacement. The average ladder position of the pixel ladders defines the coordinate system, hence displacements for the pixel are small.

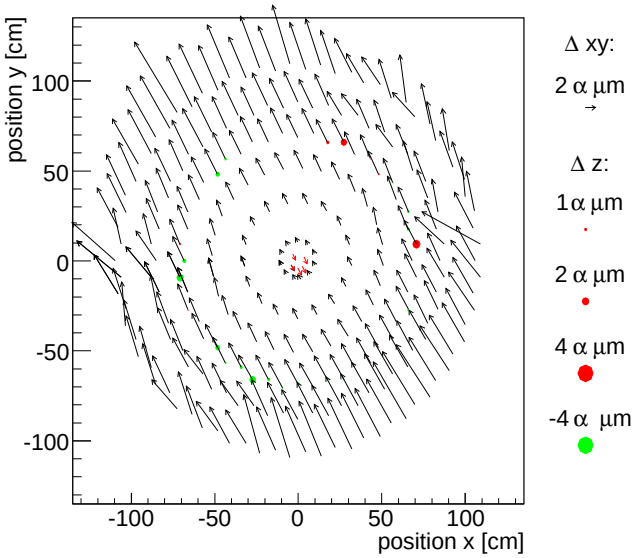

Figure 6.17: Illustration of the eigenvector of the first r-rϕ oscillation. The innermost pixel layer ladders (red) are displaced in the opposite direction than the other detectors. This is due to the coordinate system definition, which requires that the sum of all ladder displacements is zero.

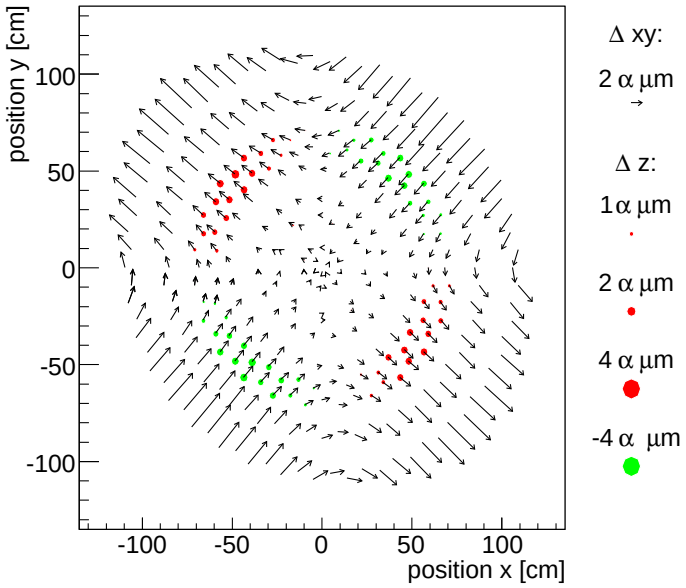

Figure 6.18: Illustration of the eigenvector of the second r-rϕ oscillation. The coupling between the oscillations in r and z is clearly visible.

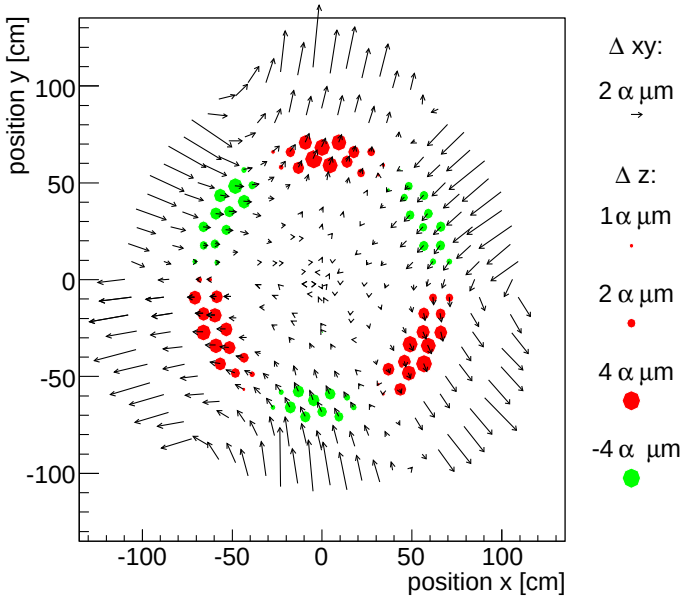

Figure 6.19: Illustration of the eigenvector of the third r-rϕ oscillation.

6.4 Impact of Prior Knowledge

Constraints and presigmas are used to implement prior knowledge about alignment precision. The impact of prior knowledge is studied on rod level in the barrel region. Single muons of two million $Z^0 \rightarrow \mu\mu$ events are used as dataset.

6.4.1 Constraint Scenarios

Several sets of constraints have been applied utilizing the methods described in chapter 5. Note that different levels are aligned simultaneously, as described in section 5.4.6, in order to apply the prior knowledge. The scenarios are:

- *Initial knowledge* In this scenario the widths of the Gaussians used to dice the alignment parameters in the simulation are applied as presigmas for the corresponding alignment parameters. Parameters which are aligned, but not misaligned are given a reasonable estimated initial uncertainty. The applied uncertainties are listed in table 6.5.

- *Prefer barrel* The presigmas of the alignment parameters of the rods are reduced by a factor of 10, hence internal deformations of the barrels, such as bending, are suppressed even further than for the *initial knowledge* scenario. Solutions are preferred which lead to large corrections of the rigid body parameters of the barrels.

- *Prefer layer* Additionally, the rigid body parameters of the layers are introduced as alignment parameters, although they are not misaligned in the *first data* scenario. The presigma was chosen to be 50 μm (table 6.6), which is similar to the expected values of the initial position uncertainty. The rods or ladders within a layer are given the same reduced presigmas as in the *prefer barrel* scenario. This scenario leads to a suppression of higher mode r-rϕ oscillations (see previous section), since a circular profile (in rϕ) of the layers is preferred. Internal bendings or shearings of the barrels are not suppressed in this scenario.

- *Prefer layer + EC* In this scenario the pixel endcaps, the inner discs and the innermost layer of both endcaps are added to the alignment procedure. Wedges, discs and petals are introduced as well as layers and a barrel for the inner discs. The endcap like geometrical structure of these components combined with the cylindric structure of the barrel structures leads to a suppression of overall deformations. The bending of the barrel, which is not suppressed in the *prefer layer* scenario, would imply a bending of a petal, which is suppressed if the endcaps are added. The applied presigmas can be found in table 6.6. Each detector in the endcap is given 4 alignment parameters, namely u, v, w, and γ.

type	u [μm]	v [μm]	w [μm]	γ [μrad]
TOB half barrels	105	105	500	90
TIB half barrels	67	67	500	59
TPB half barrels	13	13	13	10
TOB rods†	100	100	100	10*
TIB rods†	200	200	200	10*
TPB ladders†	5	5	5	10*

Table 6.5: Presigmas of alignment parameters used in the alignment procedure. The presigmas correspond to the uncertainties used in the *first data rod level* misalignment scenario except for the uncertainties labeled with *, are uncertainties of parameters which are not misaligned. Presigmas in rows labeled with † are reduced by a factor of 10 in the *prefer barrel* scenario.

type	u [μm]	v [μm]	w [μm]	γ [μrad]
TIB and TOB layer	50	50	50	50
TPB and TPE layer	5	5	5	5
TID layer	40	40	40	10
TEC layer	57	57	500	46
TID half barrels	400	400	400	100
TEC petals	10	10	10	10*
TID wedges	3	3	3	10*
TPE wedges	0.5	0.5	0.5	10*

Table 6.6: Presigmas of alignment parameters used in the alignment procedure according to the *prefer layer* and the *prefer layer + EC* scenarios. Presigmas labeled with *, are presigmas of parameters which are not misaligned.

6.4.2 Results

To interpret the results it is useful to analyze the average remaining misalignment as well as global distortions and the correlations of the alignment parameters.

Rod and Ladder Position Residuals The residuals between the true and the estimated alignment parameters of the rods and ladders are shown in figure 6.20 for the different constraint scenarios. To understand the bias introduced due to the initial misalignment, also the residuals for the *first data* misalignment scenario are shown. As a reference, the misalignment remaining after an alignment procedure without constraints is illustrated as well.

The use of the initial knowledge helps significantly to suppress the χ^2 invariant deformation, as can be concluded from the improved alignment precisions. The root mean square and the mean of the residual distributions are summarized in table 6.7. The preference of the rigid body parameters of larger structures does improve the results, however it has to be kept in mind that this is only true if these parameters are the dominating source of misalignment. Adding the endcap detector parts improved the alignment precision of the barrel. Hence it can be concluded that simultaneous alignment of the barrel and endcaps improves the overall result.

Remaining Deformations The remaining displacements are highly correlated as can be seen in the figure 6.21, where the mean displacements of the detectors in dependence of their position radii are shown. χ^2 invariant deformations like bending and shearing can clearly be identified in figures 6.21, a-d. The deformation are suppressed to a minimal amount if the *prefer barrel* or *prefer layer + EC* scenarios are used, as can be seen in figures 6.21, e and f.

	initial misalign.	no constraints	initial knowledge	prefer layer	prefer layer+EC	prefer barrel
rms u [μm]	149.8	77.5	9.1	8.47	4.66	4.90
mean u [μm]	-15.3	-10.0	17.2	-6.70	2.17	-0.58
rms v [μm]	200.9	64.7	37.6	35.8	33.8	35.2
mean v [μm]	198.4	106.8	30.2	2.50	-2.7	-4.9
rms w [μm]	144.1	80.3	20.6	13.6	22.3	23.
mean w [μm]	-1.0	-2.2	-0.7	-1.62	-0.31	-1.1
rms γ [μrad]	0.00	30.2	2.5	0.3	-0.1	0.1
mean γ [μrad]	0.00	50.3	0.1	0.0	0.1	0.0

Table 6.7: Root mean squared and mean of alignment parameter residuals for different constraint scenarios. Most corresponding distributions are shown in figure 6.20.

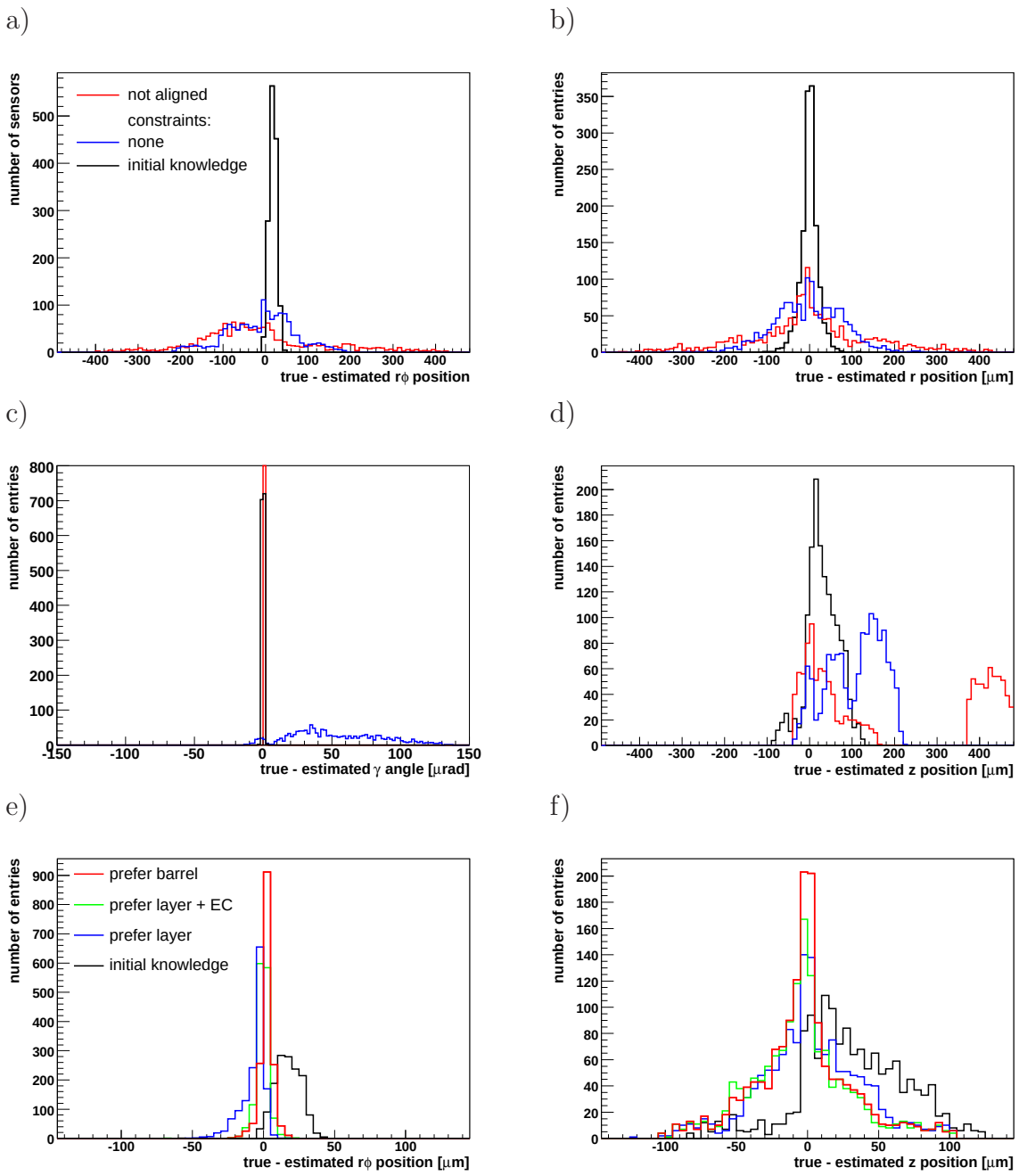

Figure 6.20: Residuals between true and estimated rod and ladder positions for different constraint scenarios. Plots a-d show the residuals of all alignment parameters of the *first data* scenario and of the alignment procedure with and without constraints (initial knowledge scenario). The angle γ is not misaligned in the *first data* scenario, leading to the red straight line at zero in plot c. Figure e and f show the residuals in the two measured coordinates for the various applied constraint scenarios. Note that the scale of the x-axis for the plots e and f is decreased in comparison to the plots above.

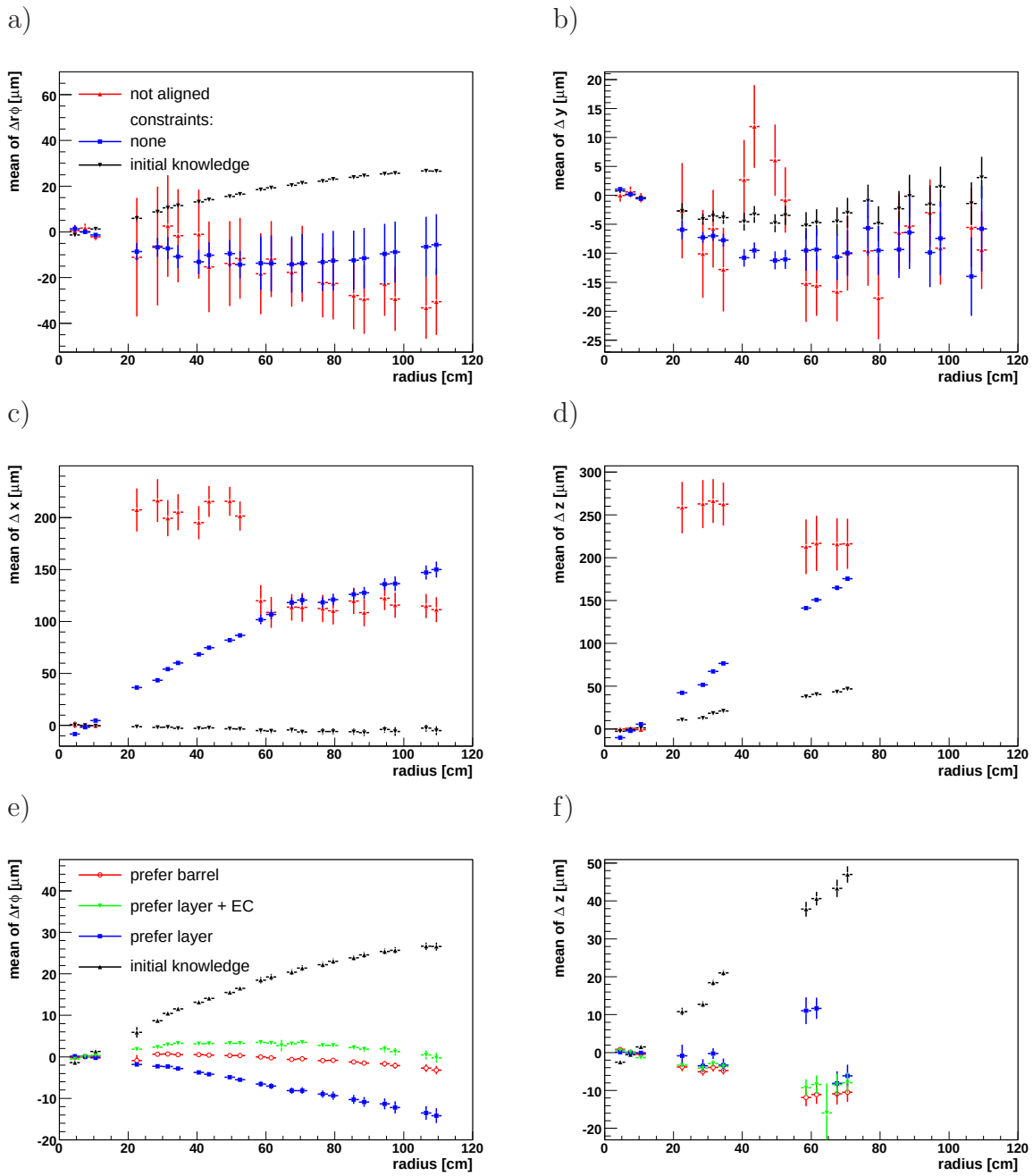

Figure 6.21: Mean of the residual distributions of the rod positions as a function of the radius of the rod positions. Figures a-d show the comparison between initial misalignment and alignment results with and without the use of initial knowledge. Figures e and f show the comparison between different applied initial uncertainties in the two measured directions (rϕ,z).

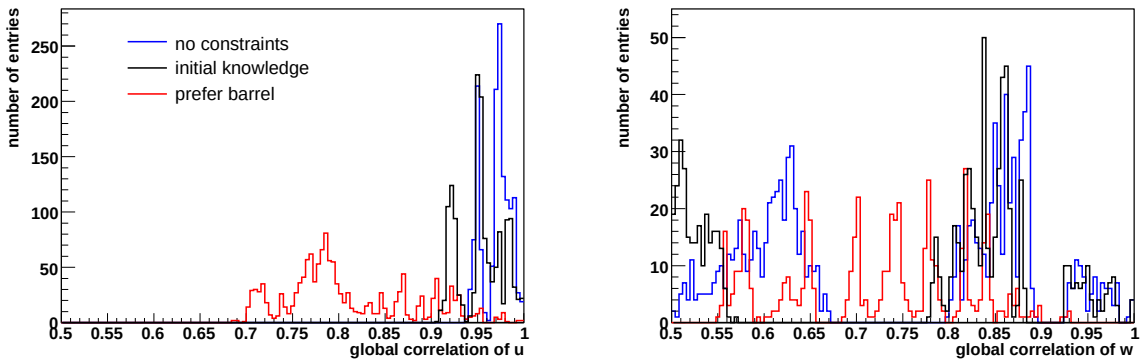

Figure 6.22: Global correlations of alignment parameters. Left: Global correlations of u alignment parameters for different applied constraints. Right: Global correlations of w alignment parameters for different applied constraints.

Global Correlations The global correlation is the maximal correlation between an alignment parameter and any linear combination of other alignment parameters. This can be determined from the covariance matrix which is available if the inversion method is used. High global correlations lead to correlated displacements. The initial uncertainties (presigmas) given to the alignment parameters are completely uncorrelated and hence decrease the global correlations as can be seen in figure 6.22, where the global correlations for different applied constraints are illustrated.
If the highest global correlation is close to one, constraints become necessary. Hence it would be useful to find a procedure to calculate the maximal global correlation without inverting the matrix. The global correlation of a specific parameter can also be determined with fast matrix equation solution methods. Therefore it is of interest which parameters tend to have the largest global correlations.
χ^2 invariant deformations have a specific structure: Displacements and rotations of large structures are compensated by internal deformations. The displacements and rotations of large structures are therefore highly correlated to linear combinations of alignment parameters which represent internal deformations. The displacements of large structures have therefore the highest global correlations as can also be seen in the figure 6.23, where the global correlations are shown separately for different hierarchies.
The values of the highest global correlations for different constraint scenarios are shown in table 6.8. Since the *prefer barrel* scenario suppressed the χ^2 invariant deformations to an acceptable level, it can be estimated that a maximal global correlation of at least below 99.7% is required to get a properly defined solution.

Conclusion Initial knowledge and preference of composite object parameters improve the alignment procedure significantly. The preference of composite object parameters is effectively selecting a plausible solution of an otherwise unsolvable problem. This method should only be used if otherwise χ^2 invariant deformations remain.

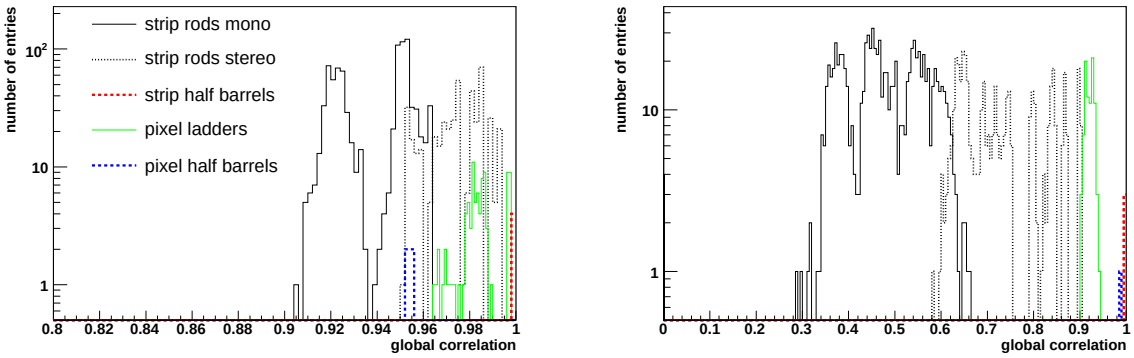

Figure 6.23: Left: Global correlations of u alignment parameters in the *initial knowledge* scenario, separated for different types of parameters. Right: Global correlations of γ alignment parameters in the *initial knowledge* scenario.

constraints	global correlation u	global correlation v	global correlation w	global correlation γ
none	0.9997	0.9999	0.9997	0.7498
initial knowledge	0.9998	0.9998	0.9986	0.7496
prefer barrel	0.9968	0.9972	0.9273	0.7483

Table 6.8: Maximal global correlation for different constraint scenarios.

This can be checked for each specific alignment case by the calculation of the maximal global correlation, which is typically a global correlation of a large support structures parameter.

6.5 Impact of Data from Z^0 Decay

Different datasets are of vital importance to constrain otherwise χ^2 invariant deformations. Z^0 bosons have the advantage that they are heavy and therefore muons from their decay have high energy. This leads to less multiple scattering and also to a higher sensitivity to deformations which change the curvature.

6.5.1 Vertex and Mass Constraints

The impact of vertex and mass constraints has been studied on rod and ladder level in the barrel region. The misalignment, the alignment parameters, and the selection cuts of the 2 million $Z^0 \rightarrow \mu\mu$ sample used are described in the beginning of this chapter. Presigmas according to the *initial knowledge* scenario are applied. Track pairs with an invariant mass between 86 GeV and 96 GeV are considered as products of a Z^0 decay. The remaining tracks are used as single tracks. Keep in mind that the remaining tracks can be tracks from a Z^0 decay, where one track is in the endcap region or outside the tracker acceptance.
Different constraints on the track fits have been tested using the method described in section 5.5:

- *Vertex* The track pair is constrained to have a common vertex.
- *Exact mass* The track pair is constrained to have a common vertex and exactly the mass of the Z^0.
- *Wide mass* The vertex constraint is applied and the mass parameter is given the initial value of the Z^0 mass and an uncertainty of the Z^0 width.

Results The resulting residuals between estimated and true rod and ladder positions are shown in figure 6.24 and the root mean squares and means of these distributions are summarized in table 6.9. The average residuals of the rod and ladder positions do not significantly improve if vertex and mass constraints are used. The global correlations of the alignment parameters are shown in figure 6.25 and it can clearly be seen that the global correlations decrease if the constraints are applied. However, some correlations remain close to one (figure 6.25). This indicates that some χ^2 invariant deformations remain undefined.
The average displacements as a function of the radius are shown in figure 6.26 and the bending and shearing deformation functions (equations 6.1) have been fitted to the alignment results. The deformation function fits well to the displacements and the resulting deformation function parameters are listed in table 6.10 for the different

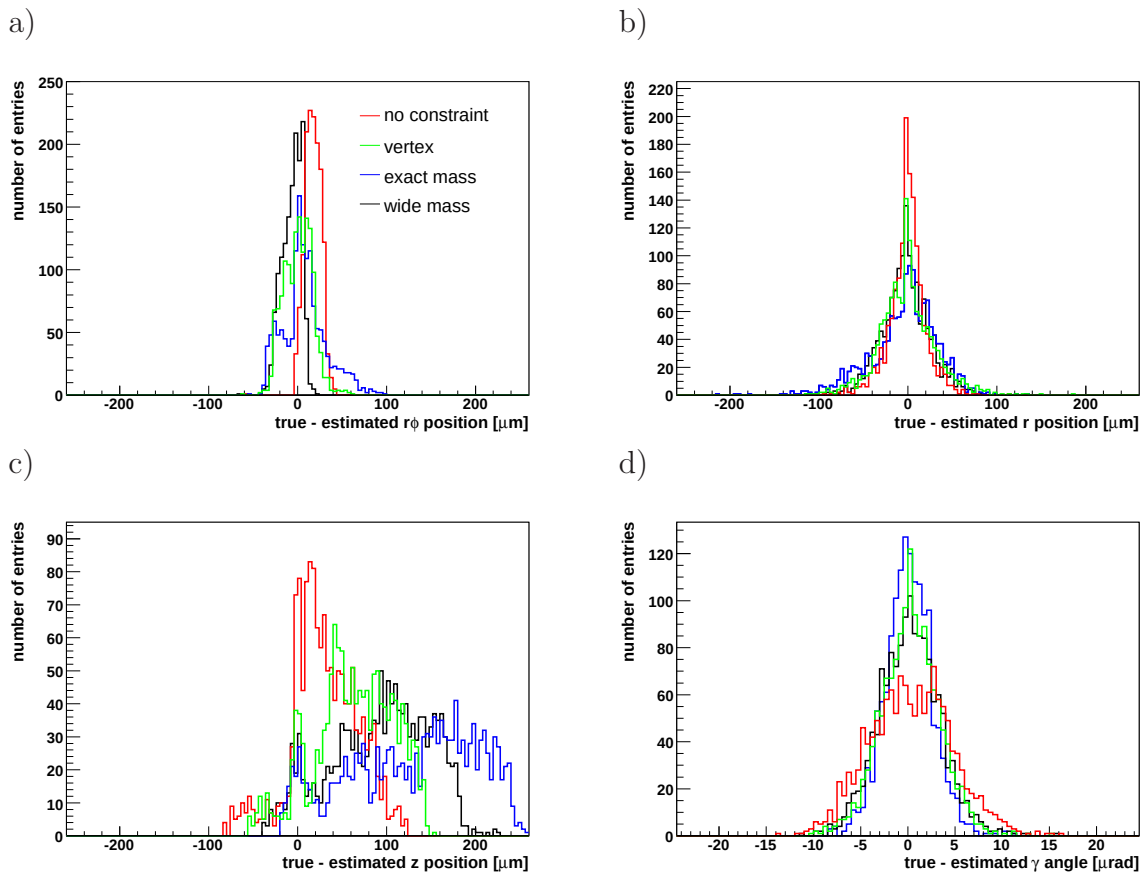

Figure 6.24: Residuals between true and estimated rod and ladder positions and orientations for different applied constraints.

applied constraints. The vertex constraint should naturally decrease the vertex offset, and indeed the offset is reduced from 3.5 μm to 1.1 μm. The mass constraint has impact on the signed curvature measurement. If the mass constraint with width is applied, the curvature changing parameter p_2 is reduced by an order of magnitude. Other deformations like the shearing in z are not suppressed by the mass and vertex constraints as can be seen in figure 6.26 (right).

In conclusion, the vertex and mass constraint have significant impact on the alignment results. The shearing and bending in rϕ is suppressed to some extend and the global correlations decrease. However, Z^0 events are not sufficient to constrain all χ^2 invariant deformations. Hence further complementary datasets are necessary.

	no constraint	vertex	exact mass	wide mass
rms u [μm]	9.1	24.7	16.1	11.0
mean u [μm]	17.2	7.94	0.63	-6.32
rms v [μm]	37.6	71.7	44.78	55.5
mean v [μm]	30.2	127.9	62.9	91.9
rms w [μm]	20.7	38.4	31.9	26.7
mean w [μm]	-0.72	-4.8	-0.96	-2.4
rms γ [μrad]	4.3	3.0	2.5	3.1
mean γ [μrad]	0.3	0.2	0.1	-0.1

Table 6.9: Root mean square and mean of alignment parameter residuals for different constraints applied. The corresponding distributions are shown in figure 6.24.

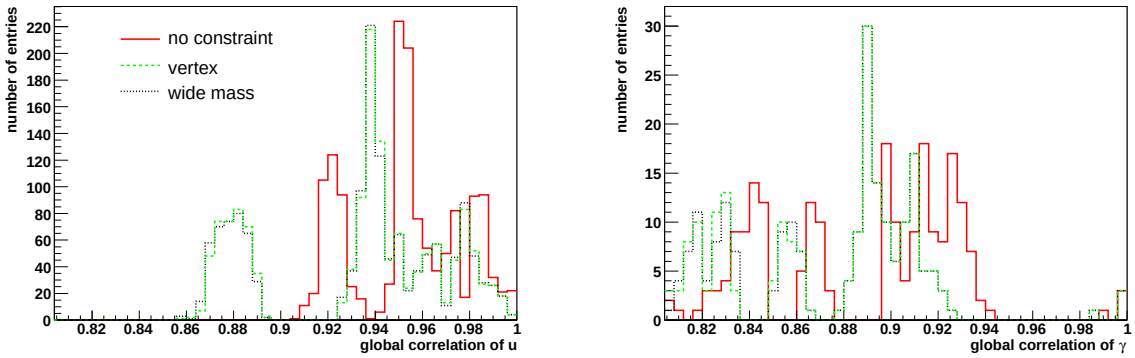

Figure 6.25: Global correlations of alignment parameters for different applied constraints. Left: Alignment parameter u, Right: Alignment parameter γ. The global correlations resulting from the exact mass constraint are not shown, since the correlations are very similar to the wide mass case.

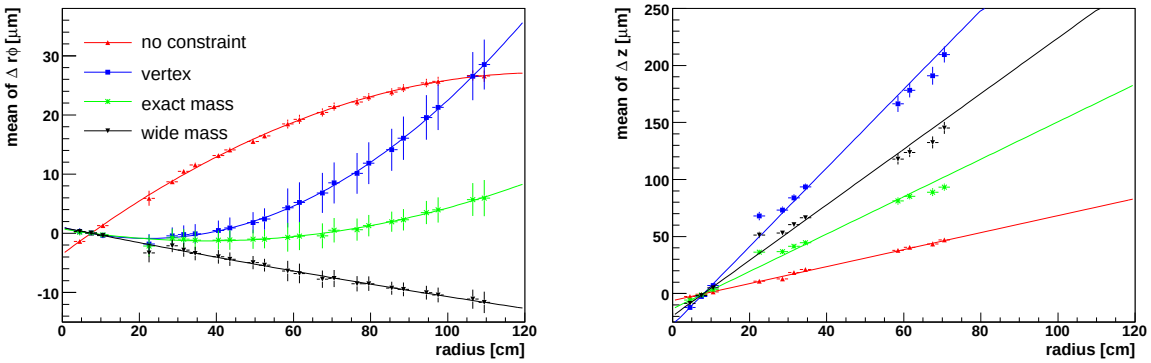

Figure 6.26: Fits of deformation functions (equation 6.1) to the average displacement as a function of radial position of the rods. Compared are results with different applied constraints on the Z^0 events.

	p_0 [μm]	p_1 [$\frac{\mu m}{m}$]	p_2 [$\frac{\mu m}{m^2}$]	z_0 [μm]	z_1 [$\frac{\mu m}{m}$]
no constraints	-3.53	48.8	-19.4	-6.17	74.5
vertex	1.05	-17	38	-27.8	345
exact mass	0.75	-10.7	14.3	-13.4	164
wide mass	0.99	-13.1	1.45	-19.6	243

Table 6.10: Resulting parameters of the fits shown in figure 6.26. The parameter p_0 is the vertex offset in rϕ in μm, the parameter p_1 is the ϕ offset in μrad, and p_2 describes an offset of the signed curvature measurement.

6.6 Impact of Cosmic Muons

Cosmic muons are an important source for calibration and alignment. Their trajectories are of vital importance since they connect different tracker parts and are hence sensitive to otherwise χ^2 invariant deformations. This has also been the experience in other high energy physics experiments, such as H1, ZEUS, BABAR. For example H1 takes cosmic runs without magnetic field to accumulate straight line trajectories which are a crucial element of their alignment procedure. A χ^2 invariant deformation of the H1 tracking device, namely a twist of the central drift tube, had been identified to be only determinable with magnetic field-off cosmic data [49]. However, at CMS the expected deformations of the tracking detectors after turning on the magnetic field are large. Therefore, conclusions drawn from runs without magnetic field cannot be applied to alignment of the tracker in the 4 Tesla magnetic field. Hence, it is not foreseen to utilize cosmic runs in the cavern without the magnetic field.

Event Selection Tracks crossing only marginal parts of the tracker lead to large inclination angles on the sensors and only few hits per track. Such tracks turned out to be of limited use and are rejected by the requirement that each track is composed of more than 18 measurements. Low energy tracks have little predictive power, since the propagation length (up to 2 m) of the cosmic track is especially large and the silicon sensors and supporting structure are crossed with large inclination angles in, leading to more material interaction. Experience showed that a cut at 15 GeV on the transverse momentum lead to the best alignment results. The χ^2 per degree of freedom of the track fit was required to be below 15 to reject tracks effected by outlier hits. Of the one million generated cosmic muons about 75k remained after the selection. Some parts of the tracker barrel are effectively not crossed by any selected cosmic track as can be seen in the hit map in figure 6.27. The 25k high energy cosmic muon sample is hardly affected by the selection criteria.

In addition to the cosmics datasets, the same dataset ($Z^0 \rightarrow \mu\mu$) and selection cuts as for section 6.5 are used. Also the misalignment, the alignment parameters, and presigmas are the same as in the *initial knowledge* scenario (section 6.5).

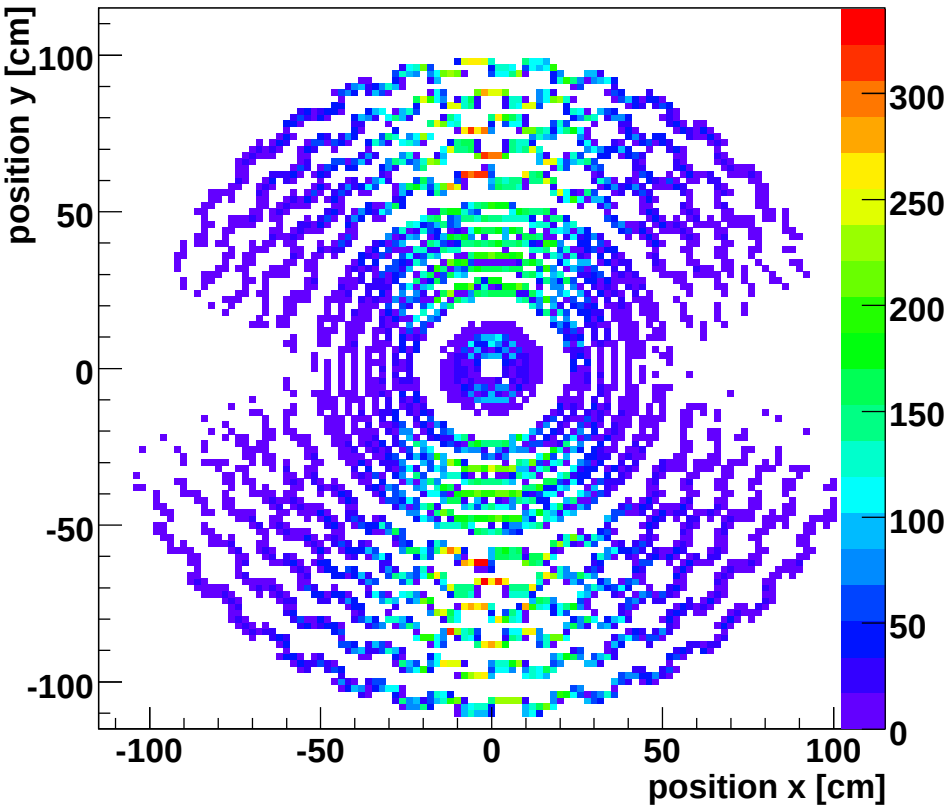

Figure 6.27: Number of hits from selected cosmic tracks as function of the global positions of the hits in the xy plane.

Results The cosmic muons improve the alignment precision significantly. The remaining residuals of the rod and ladder positions and orientations are compared to the results obtained without the use of cosmic muons (figure 6.28). The achieved precisions are summarized in table 6.11. As expected, the global correlations decrease also significantly by the use of cosmics as can be seen in figure 6.29.
The correlations are also significantly smaller and the overall result is better than the results obtained with only Z^0 boson events instead of cosmic muon events (section 6.5). The global bending and shearing deformations are largely suppressed. This can be seen in figure 6.30, where the average displacement in rϕ (left) and z (right) are plotted as a function of the rod position radius. The deformation functions (equation 6.1) fit very well to the remaining misalignment. The results of these fits are summarized in table 6.12. The offset of the curvature measurement is reduced by an order of magnitude, the vertex offset in rϕ is reduced from 3.5 μm to 0.9 μm, and the ϕ offset is reduced from 49 μrad to 13 μrad. Also the shearing in z is largely reduced and the offset in the θ measurement of tracks is reduced from 75 μrad to 19 μrad.

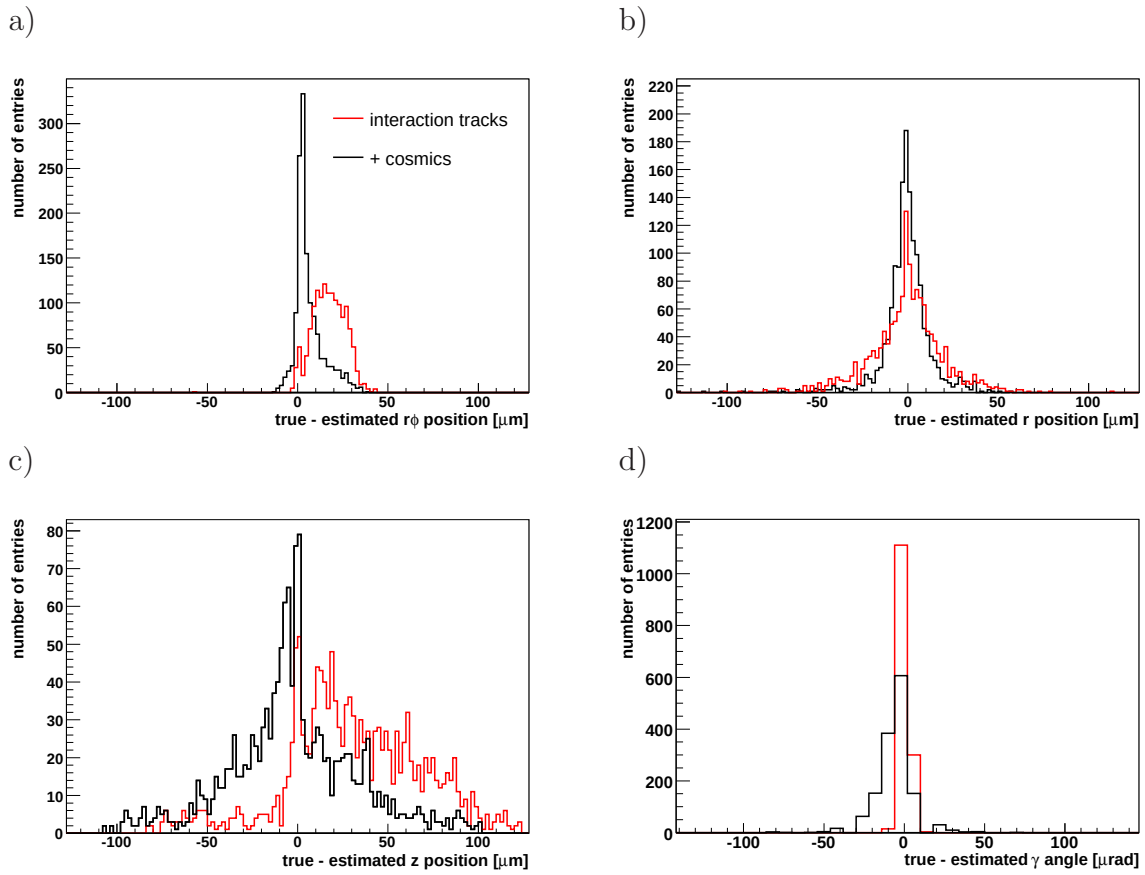

Figure 6.28: Residuals between true and estimated rod and ladder positions and orientations with and without cosmic muons used.

	interaction	+cosmics
rms u [μm]	9.1	8.0
mean u [μm]	17.2	6.2
rms v [μm]	37.6	35.4
mean v [μm]	30.2	-2.3
rms w [μm]	20.7	14.1
mean w [μm]	-0.72	0.91
rms γ [μrad]	4.3	11.7
mean γ [μrad]	0.3	-5.9

Table 6.11: Root mean square and mean of alignment parameter residuals with and without cosmic muons. The according distributions are shown in figure 6.28.

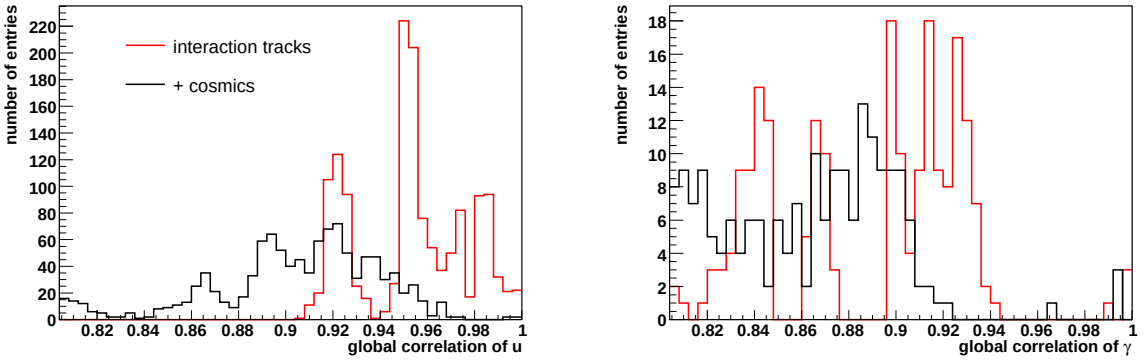

Figure 6.29: Global correlations of alignment parameters with and without cosmic muons. Left: Alignment parameter u, Right: Alignment parameter γ.

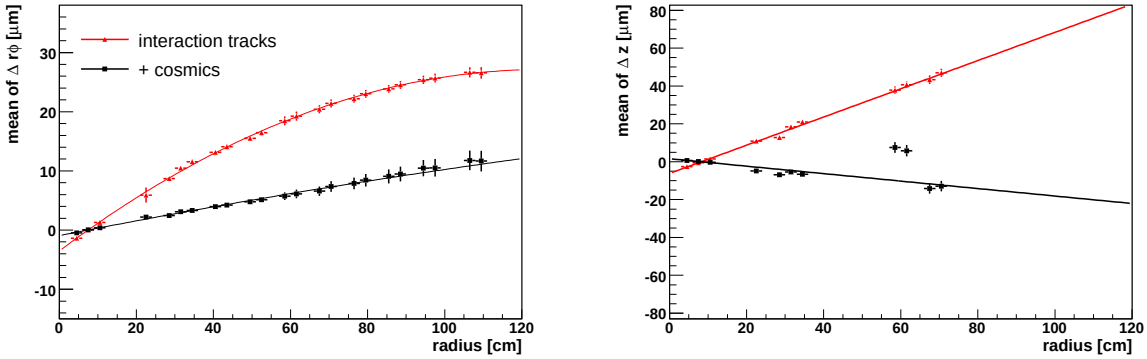

Figure 6.30: Fits of deformation functions 6.1 to the remaining misalignment with and without cosmics.

The γ parameter uncertainty increases, this could be due to the not optimal hit reconstruction for the pixel sensors (section 6.2).

	p_0 [μm]	p_1 [$\frac{\mu m}{m}$]	p_2 [$\frac{\mu m}{m^2}$]	z_0 [μm]	z_1 [$\frac{\mu m}{m}$]
interaction tracks	-3.5	48.8	-19.4	-6.2	74.5
+ cosmis	0.9	-12.8	1.6	1.6	-19.4

Table 6.12: Resulting parameters of the fits of the deformation function (equation 6.1) shown in figure 6.30.

In conclusion, cosmic muons are a vital ingredient to track based alignment. They will be available from the very beginning of data taking and suppress various otherwise χ^2 invariant deformations.

Chapter 7

Full Tracker Alignment Case Studies

In this section alignment studies with all tracker and pixel modules are shown. First the alignment parameters, the misalignment scenario and the constraints used in the following studies are presented:

Alignment The full tracker, including the pixel detector and the endcaps, is aligned down to module level. This amounts to 13252 modules, if stereo modules are counted as single modules as done in the alignment procedure. The module alignment parameters are defined with respect to the half barrels or the endcaps, respectively[1].
Each object is given four alignment parameters: the translation parameters u, v, w, and the most sensitive rotation parameter γ. The parameter v is skipped for 1D modules, since this is the unmeasured direction within the sensor plane. Altogether this amounts to 44432 alignment parameters.

Datasets The datasets and selections are the same as for the rod level studies in chapter 6. The Z^0 sample and its selection are described in section 6.1 and the cosmic samples in section 6.2.

Misalignment The default *first data* scenario (see section 5.8) is used as initial misalignment.

Prior Knowledge In order to prefer plausible deformations (section 5.6.3 and 6.4) the applied presigmas for the alignment parameters of modules are a factor of 10 smaller than the initial uncertainty (tables 5.5, 5.6). If γ is not misaligned, then a position uncertainty of 10 μrad is assumed. The presigmas for parameters of higher level structures are exactly equal to the misalignment uncertainties (table 5.6).

[1]The position uncertainty of rods is similar to the module position uncertainty and since rods only consist of a small number of sensors this level can be skipped. The layer levels are also skipped, since they are not misaligned in the *first data* scenario.

Coordinate System The coordinate system is defined by the constraint that the sum of the alignment parameter vectors **a** of the pixel half barrels has to be zero. Hence the average position of the pixel modules defines the origin of the coordinate system.

Millepede II Options In order to be able to solve such large alignment problems the GMRES (see section 5.3) method of Millepede II is used. The linear equation system is preconditioned using the result of the band Cholesky method with a bandwidth of 6. Outlier hit reweighting is used and tracks with an average hit weight below 80% are rejected. The track (local) refit is done itertively (5 iterations), since outlier reweighting is applied. The number of the alignment parameter (global) fit iterations is set to 5.

7.1 Impact of Datasets

Three different data combinations have been used for the alignment procedure in order to study the impact of different data.

- Single μ: Single tracks of the 2 million $Z^0 \rightarrow \mu\mu$ sample.
- Single μ + Z^0 mass: Single tracks of 1.5 million Z^0 events and 0.5 million Z^0 events with mass and vertex constraint.
- Single μ + cosmic μ: Single tracks of 2 million Z^0 events and cosmics of the high energy sample.

The residuals of the module positions after the alignment procedure are presented in figure 7.1 and 7.2. The mean and root-mean-square values of the residuals are listed in table 7.1 for the different datasets. It turns out that using only the single tracks in combination with applied constraints already leads to promising results. However, the means of the residuals in the most important direction (rϕ) are about 10 μm off, mainly due to bending and shearing deformations in rϕ (figure 7.3).

Z^0 mass constraint Using the 500k Z^0 events with mass constraints reduces the mean position error in rϕ by about 2 μm in the barrel and endcap region. The improvement is relatively small, showing that the statistics needed to suppress deformations is relatively high. This is due to the Z^0 width of about 2 GeV and due to the fact that the derivatives of the Z^0 mass with respect to some deformations are small. For example, the χ^2 invariant bending deformation reduces the transverse momentum of one of the muons (e.g. with positive charge), while increasing the transverse momentum of the other muon (e.g. with negative charge). Hence the invariant mass is not significantly changed.
The shearing and bending in rϕ remain to be the dominating source of misalignment if the mass constraint is used as can be seen in figure 7.3.

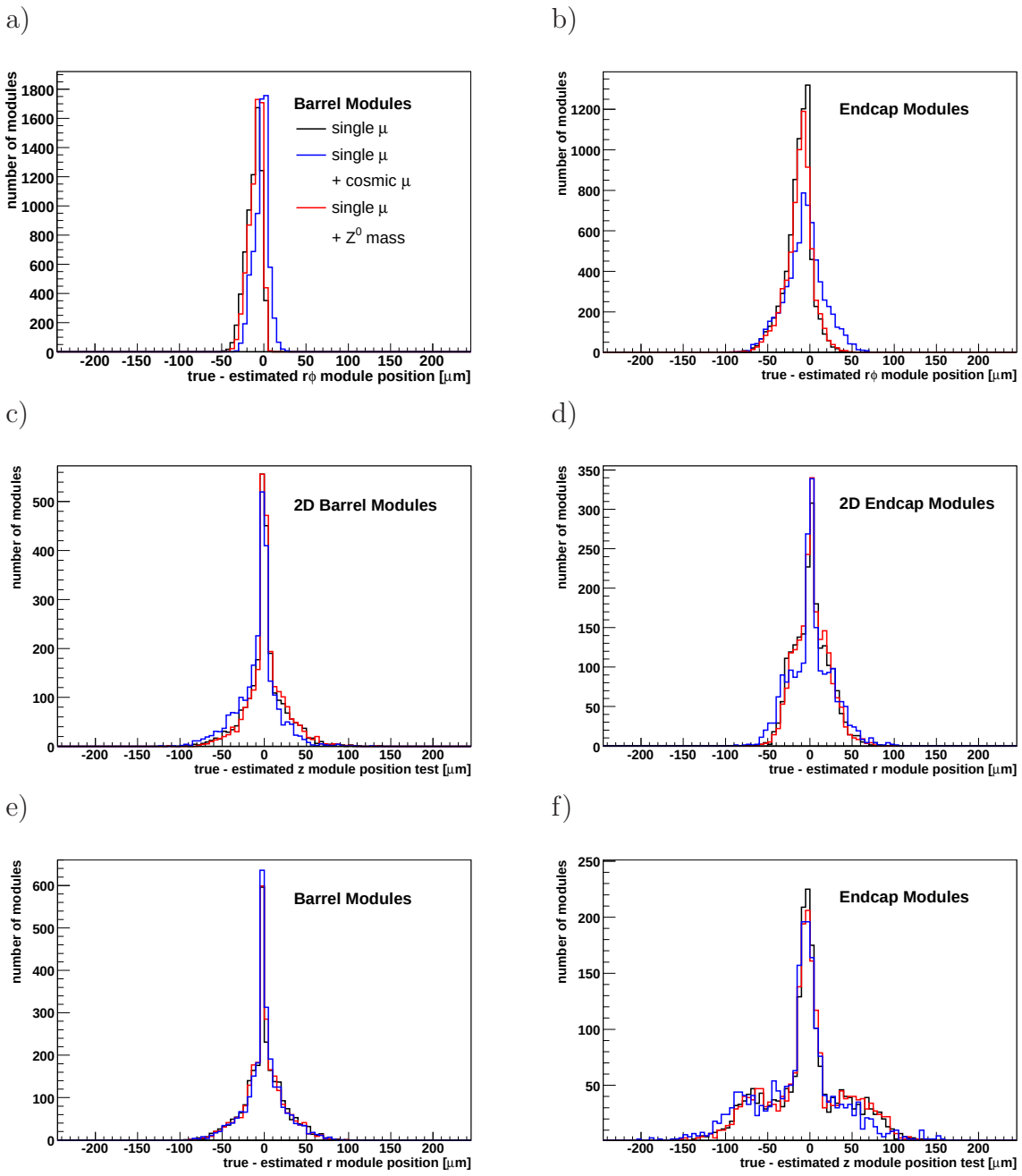

Figure 7.1: Residuals between true and estimated module positions in different directions and separated in barrel (left) and endcap (right) modules for different datasets (see text). The first row (a,b) shows the displacements in the precisely measured coordinate, the second row (c,d) the displacements in the other measured direction for 2D modules, and the third row the displacements in the direction normal to the sensor surface.

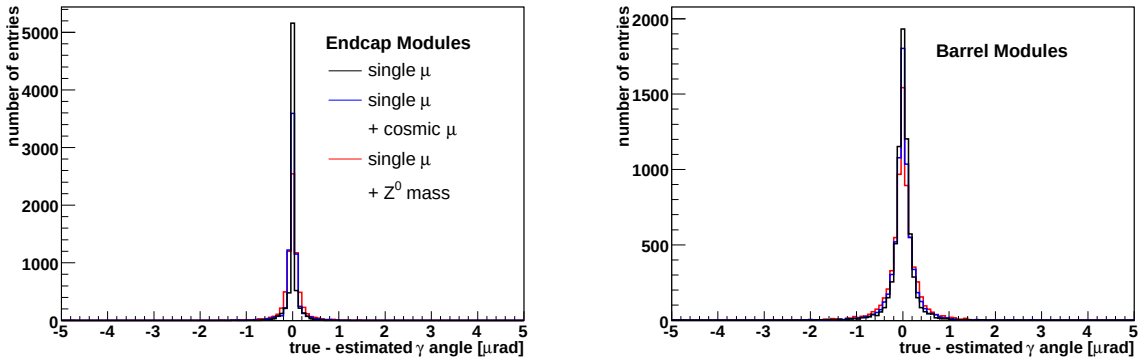

Figure 7.2: Residuals between true and estimated γ parameter separated for barrel (left) and endcap (right) modules for different datasets.

single μ from	2 mio. Z^0	1.5 mio. Z^0	2 mio. Z^0
mass & vertex constrained	-	500k Z^0	-
cosmic μ	-	-	25k high E
barrel rϕ [μm] mean	-12.1	-10.0	-3.2
rms	9.0	8.0	8.6
barrel z [μm] mean	0.8	2.5	-6.9
rms	23.8	22.7	24.6
barrel r [μm] mean	0.1	0.2	0.0
rms	24.2	23.0	23.1
endcaps rϕ [μm] mean	-13.3	-11.5	-6.1
rms	16.2	16.0	22.5
endcaps r [μm] mean	1.8	2.3	1.5
rms	21.0	20.0	25.5
endcaps z [μm] mean	-5.3	-3.8	-13.4
rms	47.8	47.5	51.9

Table 7.1: Mean and root mean square of the displacements of the modules in different direction for different used datasets. The table separates barrel (PB,TIB,TOB) and endcap (PE,TID,TEC) modules. The corresponding distributions are shown in figure 7.1.

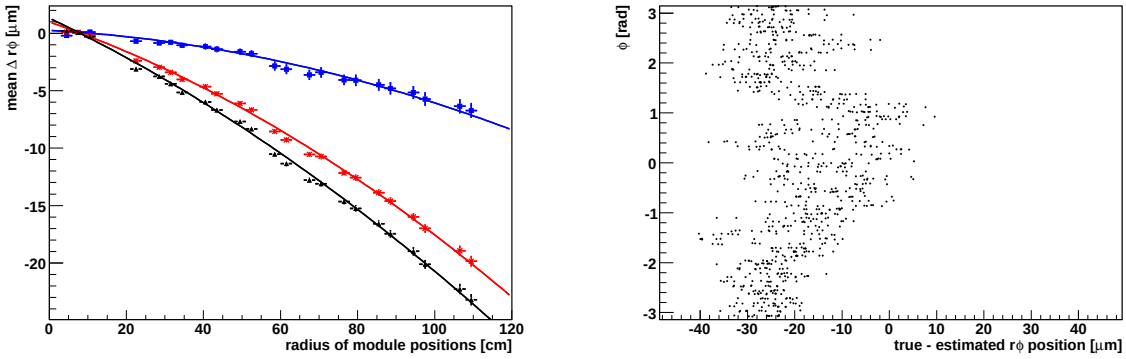

Figure 7.3: Left: The mean of the displacements of barrel modules in rϕ as a function of the radius. The shearing and bending function (6.1) is fitted to the displacements. Color code as in figure 7.1. Right: The displacement in rϕ for the modules of the last barrel layers for the single $\mu + Z^0$ mass dataset (see text).

Cosmics The use of cosmic muons significantly improves the results. Especially the bending and shearing in rϕ are suppressed, as can be seen in figure 7.3. The mean of the residual distribution in rϕ decreases by a factor of four in the barrel region and by a factor of two in the endcap region. The width of the residual distribution in rϕ increases in the endcap region. This effect is not yet completely understood.
A r-rϕ oscillation of mode zero remains undetermined even if cosmic muons are used. In terms of displacement in global coordinates x and y, this leads to linearly increasing average displacements ($\langle \Delta y(r) \rangle$) as a function of the radius of the module positions. An oscillation with a maximum deviation of the rϕ position at ϕ equal to zero translates to a linearly increasing average displacement function in y. This function is plotted in figure 7.4 and a roughly linear increase can be identified. This displacement dominates the remaining misalignment in rϕ.
The oscillation leading to displacements in x are suppressed by cosmics, since the cosmic tracks would be kinked as is shown in figure 7.5 (right). The displacements along y hardly affect the measurements of the hits from cosmic muons, since the direction of flight of cosmics is generally close to the direction of the y axis. In sensor level studies this remaining deformation is better visible than in the rod level studies. Note that beam halo muons and LAS trajectories are not expected to constrain this mode, since they do not connect different rϕ regions of the tracker with each other. Therefore deformations in the rϕ plane are not expected to be suppressed.

The precision of the γ parameter of the modules is below 1 μrad for all datasets, but it has to be kept in mind that the parameter is also not misaligned on module level. In addition a presigma on the alignment parameters is applied, which increases the χ^2 value, if γ deviates from 0. Therefore, the γ parameter is not listed along with the other parameters in the following.

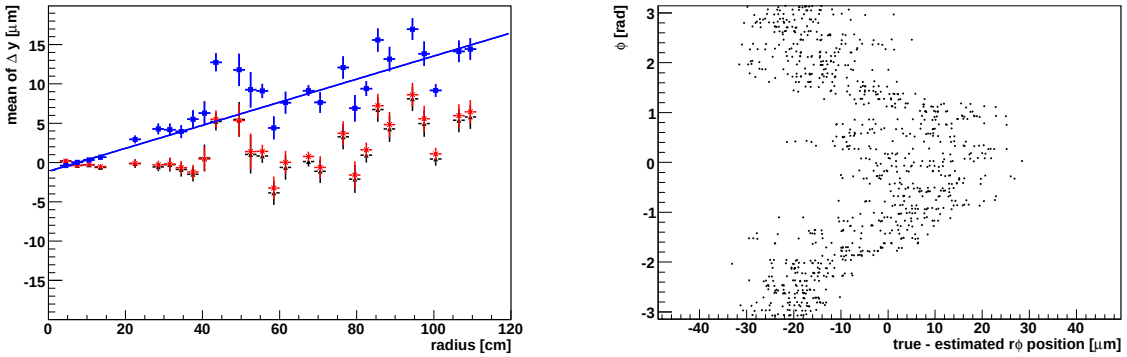

Figure 7.4: r-rϕ mode 0 oscillation. Left: The oscillation is visible as roughly linearly increasing mean displacement $\langle \Delta y \rangle$ as a function of the radius of the module positions. The Δy of all modules are used in the plot. Right: The displacements in rϕ of the barrel modules of the last layer versus ϕ. An oscillation of the order of 20 μm is clearly visible.

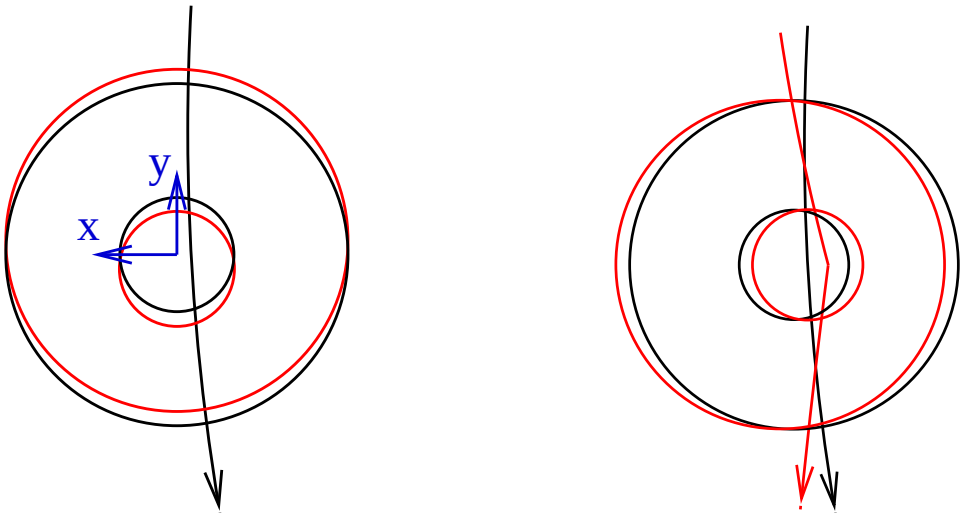

Figure 7.5: Left: Schematic illustration of r-rϕ mode 0 with the maximal rϕ (tangent of circle) displacement at $\phi = 0$ (y=0). The black arrow represents a typical cosmic track. Right: r-rϕ mode 0 with the maximal rϕ displacement at $\phi = 90°$. The red arrow represents a reconstructed cosmic track with the corresponding misalignment.

In conclusion, the cosmic muons turn out to be a very effective additional dataset complementing single muons from the interaction vertex. The reason is, that cosmic muons, which are described by only 5 parameters, connect different parts of the detector. Mass constrained Z^0 events also help suppressing χ^2 invariant deformations, however the relatively large number of free parameters in mass constrained refits (9 parameters) and the Z^0 width lead to limited improvements.

7.2 Results for 0.5 fb^{-1} Luminosity

In this study data is used which will be available after collecting 0.5 fb^{-1} of integrated luminosity. The data consist of:

- 500k $Z^0 \rightarrow \mu\mu$ events (table 6.2).
- Single muons of 1.5 million $Z^0 \rightarrow \mu\mu$ events, which are interpreted as muons of 3 millions the $W^0 \rightarrow \mu\nu$ events.
- 25k high energy cosmic muons.

However, sources for single tracks other than heavy boson decay might lead to data which could be available before 0.5 fb^{-1} of integrated luminosity are gathered and could have similar effects on the alignment. The used prior knowledge and alignment parameterization are described in the beginning of this chapter.

Alignment Results The remaining misalignment is presented in comparison to the *first data* misalignment scenario, which is also used as initial misalignment for the alignment procedure. In addition, the *long term* misalignment is shown to bring the results of the alignment procedure into perspective[2]. Figure 7.6 shows the remaining displacements separated for barrel (PB,TIB,TOB) and endcap (PE,TID,TEC) modules. The position estimate after the alignment procedure in the most sensitive direction (rϕ) for the barrel has an uncertainty of only $\sim$10 μm and thus is significantly better than the *long term* misalignment scenario estimations. For the endcap modules, the mean of the position residual in rϕ after the alignment procedure is close to 5 μm and the width is 23 μm. For the other directions the results of the alignment procedure are more precise than the position errors assumed in the *long term* scenario.
For the pixels modules the difference between true and estimated positions are presented in figure 7.7. The remaining position uncertainty in rϕ for the pixel barrel modules of 1 μm after the alignment procedure is an order of magnitude smaller than the *long term* estimate. The pixel sensor position uncertainties are in the order of a few μm for all directions and module types. The barrel module positions are generally better determined than those of endcap modules.
The residuals between the true and estimated position in rϕ are shown separately for the different detector components TIB, TID, TOB, and TEC (figure 7.8). The position estimate improves with decreasing distance of the modules to the pixel detector. The intrinsic resolution of modules closer to the beam line is generally better by construction and in addition the inner sensors are hit more often by tracks. Furthermore, the displacement due to global deformation increases with the distance

[2]The *long term* misalignment is an estimate of the achieved alignment precision after reaching $\sim$ 1 fb^{-1} of integrated luminosity. However, it is not a result of an alignment procedure.

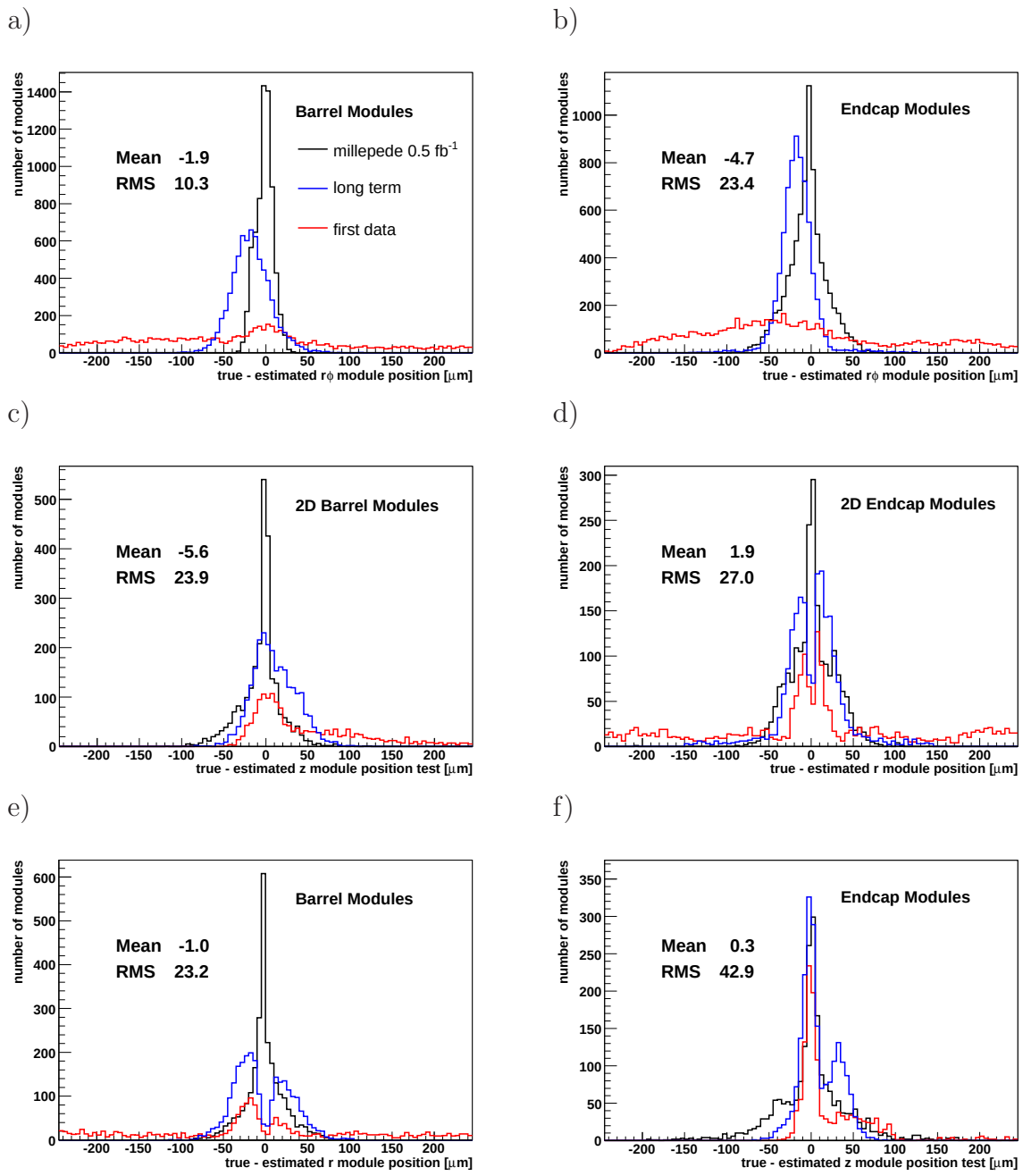

Figure 7.6: Residuals between true and estimated module positions in different directions and separately for barrel (left) and endcap (right) modules for the *first data* scenario, the *long term* scenario, and after the alignment procedure. The first row (a,b) shows the displacements in the precisely measured coordinate, the second row (c,d) the displacements in the other measured direction for 2D modules, and the third row the displacements in the direction normal to the sensor surface.

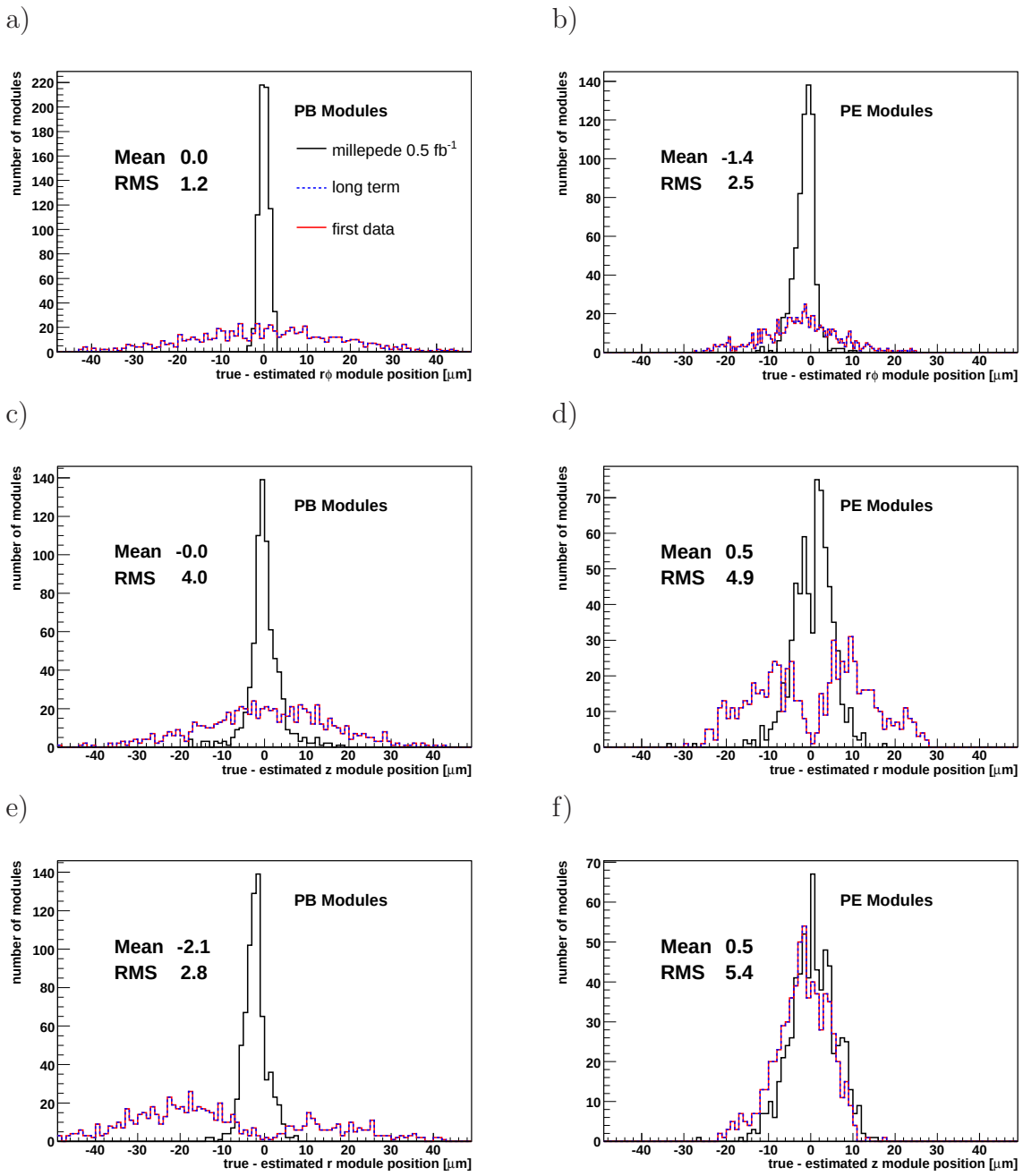

Figure 7.7: Residuals between true and estimated module positions in different directions and separately for pixel barrel (left) and pixel endcap (right) modules for the *first data* scenario, the *long term* scenario, and after the alignment procedure. The first row (a,b) shows the displacements in the rϕ direction, the second row (c,d) the displacements in the other measured direction, and the third row the displacements in the r (barrel) and z (endcap) coordinate directions.

to the pixel detector, whose sensors define the origin of the coordinate system. This can clearly be seen in figure 7.9 (left), where the average displacement of modules is shown as a function of the radius of the modules.
The overall remaining misalignment is dominated by a global χ^2 invariant deformation. A r-rϕ oscillation of mode zero, with the rϕ displacement maximum for modules positioned at ϕ close to zero, is clearly visible in figure 7.9 for the barrel modules. This effect is explained in detail in section 7.1. This also explains the double peak like structure in the residual distribution for the outer barrel modules (7.8, b). The peak at about 15 μm is caused by modules with a ϕ position around 0, while the peak at -15 μm is due to the modules with a ϕ position around $\pm\pi$. That this displacement is also present in the endcaps can be seen in figure 7.9 (left), where all modules were used to plot the roughly linearly increasing mean $\Delta y(r)$ distribution, which is typical for this r-rϕ oscillation (as discussed in section 7.1).

In conclusion, the positions of the modules have been determined to a precision between 1-20 μm. It is the first time that a full tracker alignment strategy for the CMS tracker has been proven to work in principle. However, small χ^2 invariant deformations remain, leading to position precisions which are still of the size of a significant fraction of the intrinsic resolution of the sensors. An especially weakly suppressed deformation, namely a r-rϕ oscillation, has been identified. In general, the results are better than the misalignment estimates used in the current technical design report [2] for studies on the impact of misalignment.

Computing Requirements The datasets used lead to a matrix density of 8.6% which translates to less than 2 GB of memory needed. The CPU time used on a 64 Bit CPU is 1.2 hours. If low energy cosmics are added, the results do not significantly improve, however, the matrix is denser due to the broader variation of the direction of flight in the production of this cosmic dataset (table 6.4). This leads to a matrix density of 15% and CPU need of 2 hours. The building of the matrix takes about 50 minutes (only done once), while the solving of the matrix equation takes about 10 minutes, but has to be done 5 times in the course of the outlier rejection.
The computing requirements are very limited and still leave space for more alignment parameters and datasets.

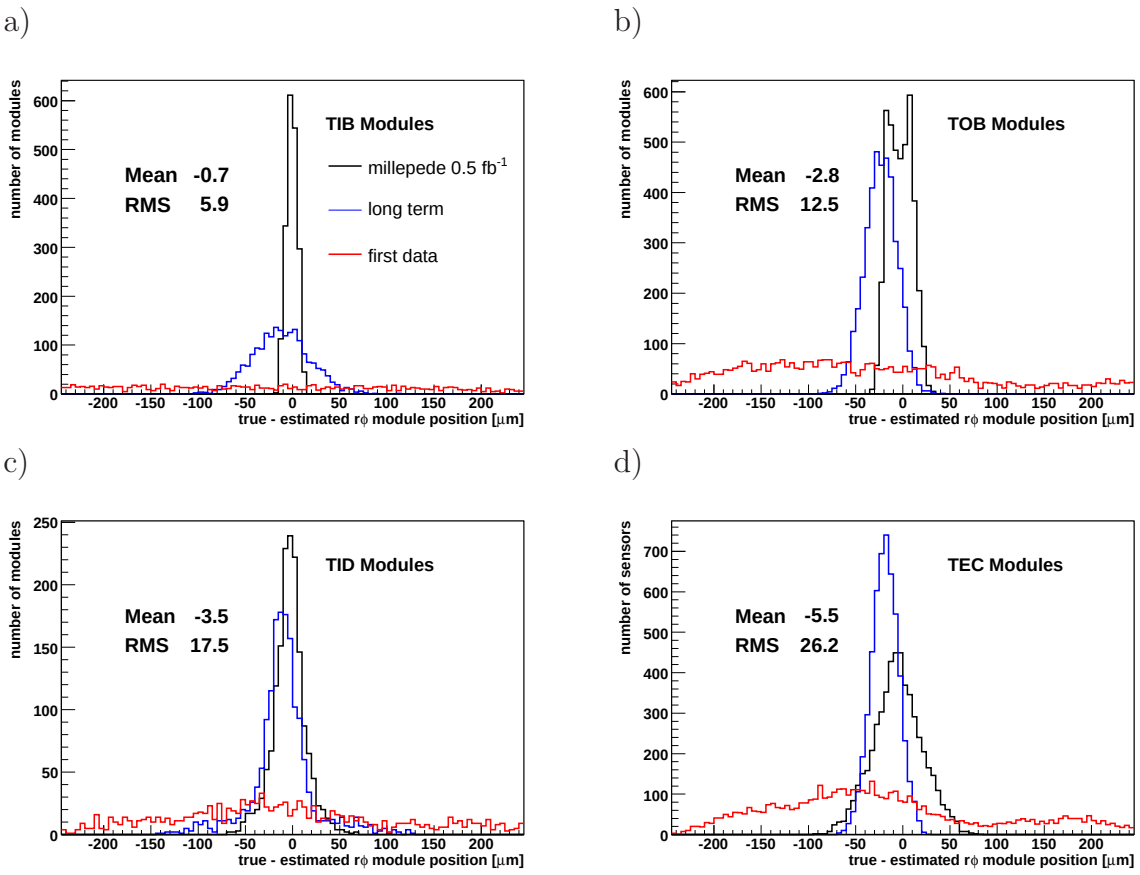

Figure 7.8: Residuals between true and estimated module rϕ positions for different detector components for the *first data* scenario, the *long term* scenario, and after the alignment procedure.

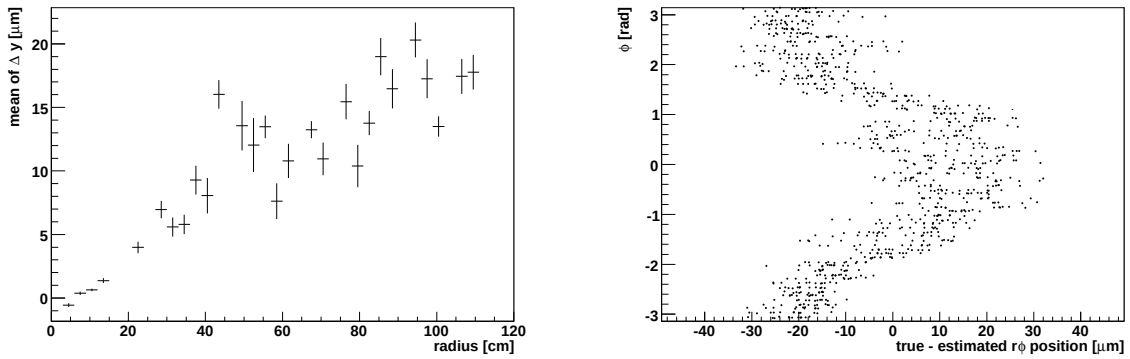

Figure 7.9: r-rϕ mode 0 oscillation. Left: The oscillation is visible as roughly linearly increasing mean displacement Δy as a function of the radius of the module position. The Δy of all modules are used in the plot. Right: The displacements in rϕ of the barrel modules of the last layer versus ϕ. An oscillation is clearly visible.

7.3 Variation of Statistics and Event Weights

The results in the 0.5 fb^{-1} scenario are very promising, however, this requires several months of data taking at nominal luminosity. In this section it is studied how the statistics impact the result. In addition it was tested what happens if important datasets like the cosmic muons are given more weight in the χ^2 minimization by using the same tracks several times. Five different dataset combinations have been tried:

- Single muons from 2 million Z^0 events and 1/5 of the high energy cosmics (5k events).
- Single muons from 2 million $Z^0 \rightarrow \mu\mu$ events and the full high energy cosmic muon dataset (25k events).
- Single muons from 0.5 million Z^0 events and the full high energy cosmics.
- Single muons from 2 million Z^0 events and using the full high energy cosmic muon events five times.
- Single muons from 2 million Z^0 events and all cosmic muon events five times.

The results for the different datasets are summarized in table 7.2.
If all high energy cosmics are used the result is significantly better than without them as already shown in section 7.1. If only a fifth of the cosmics statistics is available, this has significant impact on the remaining deformations. The mean of the position errors after the alignment procedure in rϕ are larger and hence much closer to alignment results obtained without cosmics (table 7.1). The displacement in other directions than rϕ are not significantly effected by the reduced cosmic muon statistics.
If the number of single tracks from the interaction vertex is reduced by a factor of four, then the precision of the module position estimate along the rϕ coordinate only slightly degrades. The modules measure the hit position along the rϕ direction very precisely (5-40 μm) and on average each module has thousands of hits even if only 0.5 million $Z^0 \rightarrow \mu\mu$ events are used. Therefore the position would be determined to a level of a fraction of a μm (eg. $\frac{20\mu\text{m}}{\sqrt{5000}} = 0.3\mu\text{m}$), if the global correlations of the alignment parameters would be small. Clearly, the remaining displacement in rϕ are dominated by global deformations and adding more tracks from the interaction point with similar energy does not suppress such deformations. However, displacements along directions which are not that precisely measured by the module profit much more from higher statistics. The strategy of reweighting cosmic events by reusing the tracks five times leads to slight improvements in some directions and slight degradations in others. Adding the medium momentum (transverse momentum>25 GeV) cosmics generally improves the alignment precision by a few %.

Z^0 (single μ) cosmic μ		2 mio. 1/5 high E	2 mio. high E	1 mio. high E	500k high E	2 mio. 5×high E	2 mio. 5×all
barrel rϕ [μm]	mean	-7.3	-3.2	-2.2	-1.4	-2.6	2.7
	rms	9.0	8.6	8.7	9.3	8.1	7.6
barrel z [μm]	mean	-4.5	-6.9	-9.8	-11.9	-9.9	-8.2
	rms	24.2	24.6	28.9	33.2	25.2	23.0
barrel r [μm]	mean	0.0	0.0	0.2	1.2	0.0	-0.1
	rms	23.5	23.1	25.6	32.3	22.7	20.0
endcap rϕ [μm]	mean	-9.6	-6.1	-4.9	-4.1	0.8	0.8
	rms	22.6	22.5	24.7	26.8	22.3	22.1
endcap r [μm]	mean	1.2	1.5	1.2	1.2	1.6	1.6
	rms	26.0	25.5	28.4	32.3	25.0	24.8
endcap z [μm]	mean	-10.9	13.4	-17.8	-24.5	-16.6	-15.0
	rms	52.6	51.9	53.2	52.2	51.8	52.3

Table 7.2: Mean and root mean square of position errors for barrel and endcap modules in different directions. The used datasets are indicated in the first two rows. No vertex or mass constrained was used for Z^0 events.

7.4 Impact of Outlier Rejection

To test the impact of outlier rejection, the scenario with a luminosity of 0.5 fb^{-1} has been used (section 7.2). Different outlier rejection methods (section 5.3.5) have been tested.

By default the hit reweighting method is used to treat outliers in this thesis. Tracks with an average weight of the hits of below 80% are rejected. The alignment precision is compared to the alignment precision achieved without outlier rejection in table 7.3. The comparison convincingly demonstrates that outlier rejection is essential. For example, the position uncertainty for barrel modules along the rϕ direction is reduced from 18 μm to 10 μm by the use of outlier rejection.

Also the method of rejecting whole tracks if the standard deviation of the track fit has been large, is tested. Standard deviation cuts of 54, 27, 3, 3, and 3 in the respective iterations are applied. The achieved alignment precision is similar to the precision reached with the default settings.

As a further test the number of iterations was increased from the value 5 (default) to 10 using the otherwise default options. The resulting positions error distributions tend to have a slightly larger mean and slightly thinner width.

method		none	reweighting	χ^2 cut	reweighting
iterations		1	5	5	10
barrel rϕ [μm]	mean	1.9	-1.9	1.1	-4.3
	rms	17.9	10.3	9.6	8.4
barrel z [μm]	mean	-10.9	-5.9	-7.0	-3.3
	rms	33.7	23.9	23.6	20.9
barrel r [μm]	mean	-0.8	-1.0	-0.9	-1.0
	rms	32.7	23.2	22.8	20.5
endcaps rϕ [μm]	mean	-3.1	-4.7	-1.3	-6.9
	rms	31.47	23.4	23.0	19.9
endcaps r [μm]	mean	1.7	1.9	1.6	1.9
	rms	35.9	27.0	26.3	23.7
endcaps z [μm]	mean	-6.0	0.3	-0.2	2.1
	rms	44.9	42.9	42.7	40.6

Table 7.3: Mean and root mean square of position errors for barrel and endcap modules in different direction. Different procedures for outlier rejection have been applied.

7.5 Summary and Outlook

Promising results have been achieved with the proposed CMS tracker alignment strategy. The remaining misalignment is smaller than the initial estimates used in the technical design report. For the first time within the CMS collaboration a proof of principle for the vital task of tracker alignment has been achieved. The strategy presented can be understood as a milestone and builds a solid base for further studies that could include more factors which improve or degrade the alignment precision. In the following the next most important steps for full tracker alignment studies are presented.

More Complementary Data The cosmic muons produced connect different regions of the detector in the xy-plane with each other via tracks. Regions of the tracker which are far apart in z are not connected at all via tracks so far. However, the trajectories of beam halo muons and the laser beams of the LAS will have this property. Therefore deformations, which lead to displacements depending in the z coordinate rather than on the yx-coordinates, are expected to be suppressed by this data. An example for such χ^2 invariant deformations is the twist of the tracker, shown in section 6.12.

New Misalignment Scenarios In this thesis the *first data* scenario was used in order to be compatible with other alignment strategies and studies proposed within CMS. This scenario is already quite realistic, but could still be improved. More rotations could be implemented, such as the rotations of the TEC around the global

y coordinate, which is currently set to zero. Also intrinsic deformations of large structures like a twist of the barrel could be implemented. The rotation and twist just mentioned are expected to be determined by the use of beam halo muons, since they lead to large displacements between sensors which are far apart in the z direction.

Systematic Errors In the studies a correct magnetic field, a correct material budget estimation, correct initial uncertainty estimates, and a stable positioning of the modules for a period of weeks or months are assumed. All these assumptions will not hold entirely true and will lead to a degradation of the alignment precision. However, especially the material budget and the magnetic field uncertainty also affect the tracking and a common procedure within CMS to simulate these effects would be desirable.

Chapter 8

Effects of Misalignment

In this chapter procedures to monitor the impact of misalignment on track parameters with and without the knowledge of the simulation truth are proposed. A way to translate a possible track parameter bias discovered into an alignment correction is described and tested.

8.1 Misalignment Monitoring

The alignment results have so far been presented in comparison to the true geometry. This is only possible in a simulation study, but not with real data. However, comparing physical distributions obtained from simulations with ideal knowledge of the geometry with the scenario, where the misalignment was aligned as described using data corresponding to a integrated luminosity of 0.5 fb^{-1}, can be used to understand the effects of the remaining misalignment. So far this has been done in dedicated studies [3] using the *long term* and *first data* misalignment scenarios. Another method to monitor the effects of misalignment is to investigate expected symmetries, which can be distorted by misalignment. For the studies of both methods, 500k Z^0 events (section 6.1) have been used.

8.1.1 Comparison of Ideal and Aligned Geometry

The detector is misaligned according to the results of the alignment study using data from 0.5 fb^{-1} of integrated luminosity (previous chapter). In figures 8.1 a and b the transverse momentum distributions of the reconstructed μ^+ tracks and μ^- tracks are shown, respectively. For both charges, no difference between the distributions with the aligned detector and with the ideal geometry can be seen. This is consistent with the fact that the bending deformation has been largely suppressed by the use of cosmic muons and the Z^0 mass constraint. Figure 8.1 c shows the invariant masses of the muon pairs. No impact of the remaining misalignment on the mass can be seen, which is expected to some extent, since the Z^0 mass was used as constraint in the alignment procedure. The reconstructed transverse momentum of the Z^0 is

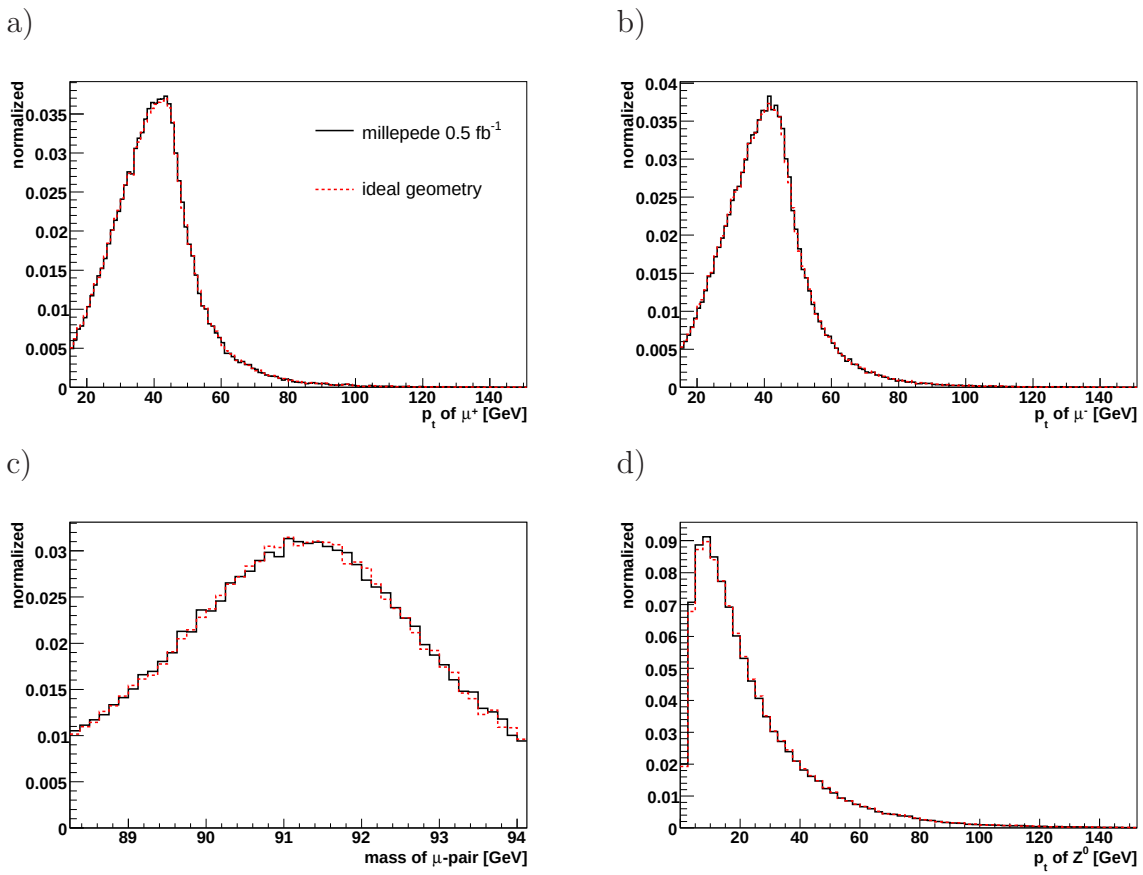

Figure 8.1: Comparison of resulting distributions with ideal geometry and a geometry determined by alignment using 0.5 fb^{-1} of integrated luminosity. a (b): Transverse momentum of μ^+ (μ^-), c: invariant mass of muon pair, and d: transverse momentum of Z^0.

also hardly effected by the remaining misalignment (figure 8.1 d). The impact on the reconstruction of the impact points (point of closest approach to the beam line) of tracks has also been studied. A small r-rϕ oscillation occurred in the 0.5 fb^{-1} scenario. Figure 7.9 (left) shows the average displacement in the global coordinate y as a function of the radial position of the modules. A straight line fitted to this distribution can be understood as the bias of the tracks due to the remaining misalignment. The fitted line crosses the y axis (radius = 0) at about -1 μm, hence the impact point position is biased by about -1 μm in the y-coordinate. The mean of the impact point distribution in the y coordinate (figure 8.2, a) is indeed -1.1 μm with misalignment compared to 0.0 μm without misalignment. The mean of the impact point distribution in the x coordinate (figure 8.2 b) is 0.5 μm after alignment. The slight offset of the average impact point position leads also to a slightly higher average impact point position in the radial direction, as can be seen in figure 8.2 c. The z distribution of the impact point is very similar for misaligned and ideal geometry. Note that the coordinate system is defined via the average pixel barrel

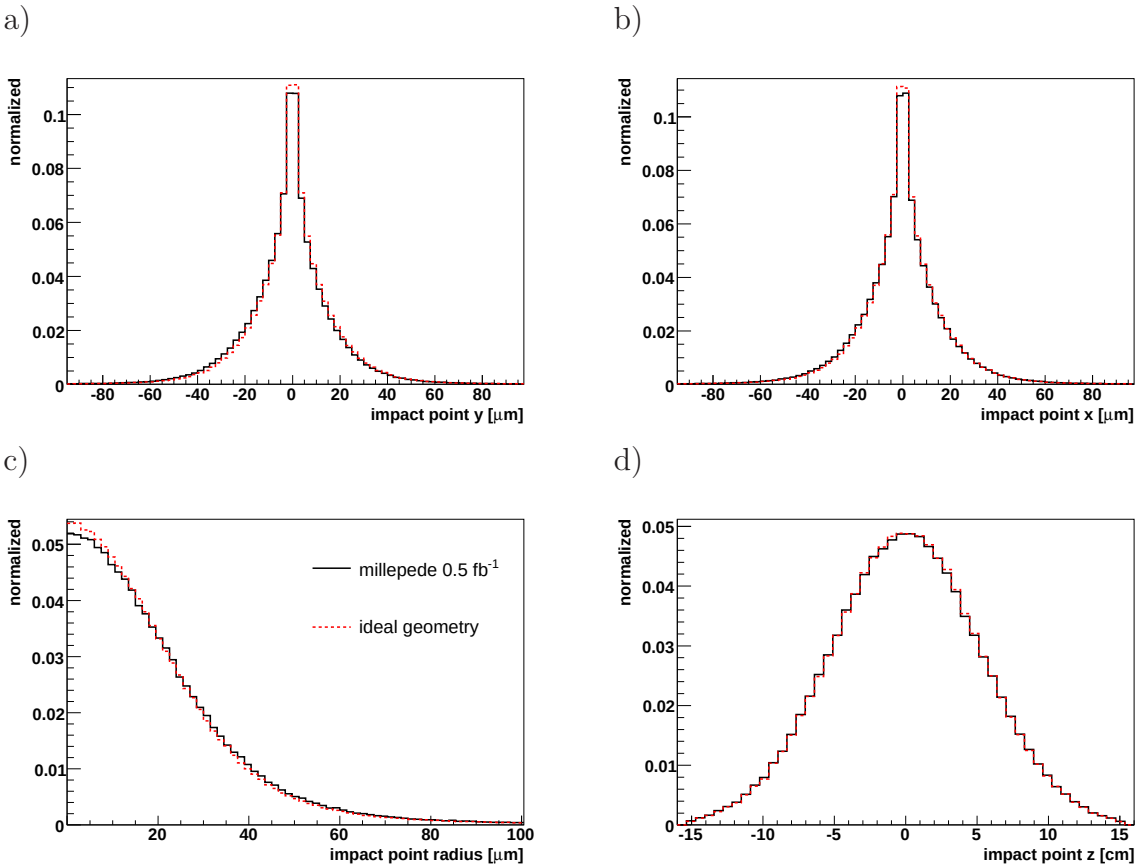

Figure 8.2: Comparison of resulting distributions with ideal geometry and a geometry determined by alignment using 0.5 fb^{-1} of integrated luminosity. a: Radial position of the point of closest approach to the beam line (impact point), b: z position of the impact point, c (d): x (y) position of the impact point.

sensor positions in this thesis. There is no reason to expect the interaction point to be exactly at the center of the pixel detector, hence the impact point does not need to be (0,0,0) on average if real data is used. Only the fact that average impact point in the simulation is set to zero leads to the centered distribution for the ideal geometry.

The discussed figures 8.1 and 8.2 show the impact of misalignment on distributions which can also be produced with real data, however the effects of the misalignment are hard to detect in these rather broad distributions. Therefore the effect on reconstructed track parameters is also studied with 50k single μ^+ tracks from a particle gun with a transverse momentum of exactly 100 GeV. The tracks are equally distributed in ϕ and η and their vertex position is exactly zero. Material interactions effects are not supported by the gun. The gun simulates the hits with misaligned geometry,

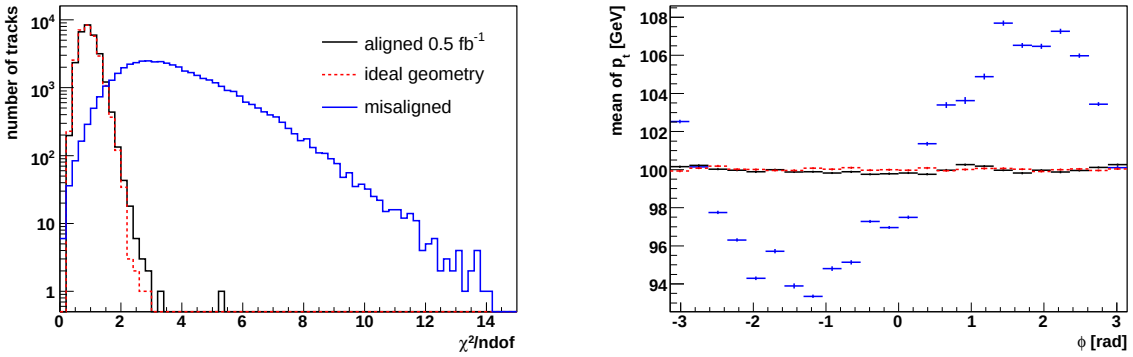

Figure 8.3: Comparison of resulting distributions from μ^+, which have a transverse momentum of exactly 100 GeV, with ideal geometry, aligned geometry using 0.5 fb^{-1} of integrated luminosity, and initial misalignment. Left: χ^2 of track fits. Right: Mean of transverse momentum as a function of the azimuthal angle ϕ.

while the reconstruction assumes an ideal geometry. Hence[1] the alignment parameters effectively switch the sign in comparison to alignment parameters used previously.

The χ^2 of the track fits is shown in figure 8.3 (left). The average χ^2 values with the ideal geometry and after the alignment are similar to the % level. The χ^2 values with the intial misalignment are much larger. The bias on the transverse momentum with ideal, aligned and intial misalignement is illustrated in figure 8.3 (right). The intial bias of several % in some ϕ region is reduced to about a permille. The reconstructed transverse momentum for all tracks is shown in figure 8.4 (left). The relative error of the transverse momentum measurement at 100 GeV increases from 1.68 % to 1.72 % if the aligned geometry is used instead of the ideal geometry. A bias in the transverse momentum of 0.1 % is introduced. The bias of the transverse momentum as a function of ϕ can be seen in figure 8.4 (right), for the aligned and ideal geometry. A very small dependence of the bias on ϕ for the aligned geometry can be identified. The impact of the remaining misalignment on the reconstruction of the point of closest approach to the beam line is shown in figure 8.5. A bias of only about 1 μm of the measurement in the y coordinate is visible. The root mean square of the distribution is about 7 μm with and without misalignment.

In conclusion, the uncertainties introduced due to misalignment are small in comparison to the absolute resolution of the reconstruction. The vertex position (1 μm bias) and transverse momentum measurements (1 permille at 100 GeV) are biased only by small amounts and the overall resolution does only slightly decrease.

[1]The simulation of hits is normally done with ideal geometry and the reconstruction uses a misaligned geometry.

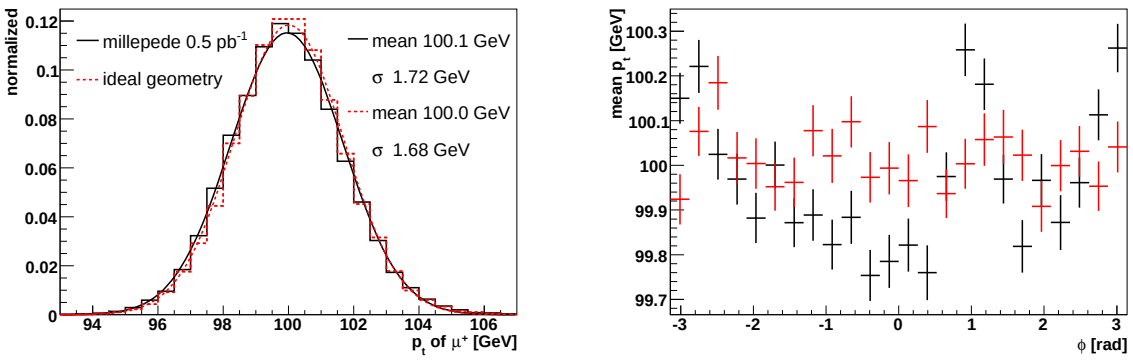

Figure 8.4: Comparison of resulting distributions from μ^+, which have a transverse momentum of exactly 100 GeV, with ideal geometry, aligned geometry using 0.5 fb^{-1} of integrated luminosity, and initial misalignment. Left: Transverse momentum distributions fitted with Gaussian distributions. Right: Average transverse momentum as a function of ϕ.

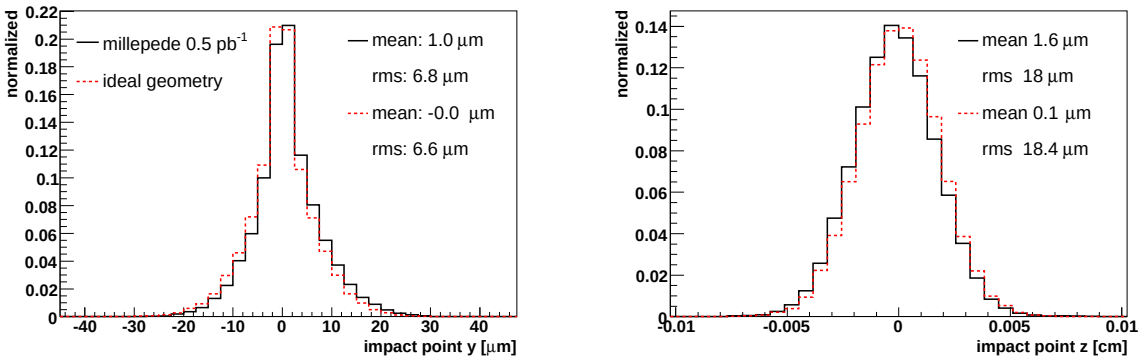

Figure 8.5: Comparison of resulting distributions from μ^+, which have a transverse momentum of 100 GeV and a vertex position of exactly (0,0,0), with ideal geometry, aligned geometry using 0.5 fb^{-1} of integrated luminosity, and initial misalignment.Left: y position of the impact point. Right: z position of the impact point.

8.1.2 Monitoring Expected Symmetries

The average signed curvature (κ) of negatively and positively charged tracks can be assumed to be identical. Neither wrong material budget estimates nor magnetic field deviations would explain such an asymmetry. On the other hand, the bending deformation, which is likely to emerge in alignment procedures, adds a constant bias to the signed curvature. To visualize such a potential shift of the signed curvature, the positive part (κ^+) and the absolute value negative part ($\kappa^- <$) are shown together in figure 8.6. Except for statistical fluctuation the distributions should be identical if the curvature is not biased. The compatibility of the distributions can be tested, defining:

$$\frac{\chi^2}{\text{ndof}} = \frac{1}{N}\sum_{i=0}^{i=N}\frac{(\kappa_i^+ - \kappa_{i+j}^-)^2}{\sqrt{(\kappa_i^+)^2 + (\kappa_{i+j}^-)^2}}, \tag{8.1}$$

where N is the number of bins used and κ_i^+ the entry at bin i of the corresponding histograms. The index j denotes an artificial shift which can be added. A window with a width of $\pm 10^{-4} cm^{-1}$ ($\pm$100 bins) around the maximum of the distribution is used to determine the χ^2. The $\frac{\chi^2}{\text{ndof}}$ should be about one and minimal for j=0, if no bias exists. For the 0.5 fb^{-1} scenario this is the case as can be seen in figure 8.6 b, where the $\frac{\chi^2}{\text{ndof}}$ is shown as a function of j.
The muons of the Z^0 decay of 500k events are used to monitor the symmetry for the case that the 0.5 fb^{-1} scenario is applied. The bending could vary for different $\eta\phi$-regions. Hence the same procedure has been performed for histograms filled with tracks of certain $\eta\phi$-regions. 8 bins in ϕ and 3 bins in η have been introduced. Each $\eta\phi$-bin contains approximately 40k tracks. A typical histogram is plotted in figure 8.6 c. The small statistics leads to fluctuations in the result of the fit. The estimated shift in the fits with misalignment are compared to the results without misalignment in figure 8.6 d. Again no difference can be seen.

In conclusion, the remaining misalignment of the 0.5 fb^{-1} scenario has very small impact on the curvature symmetry and it will be hard to actually monitor such small displacements.

8.2 Applying Symmetry Corrections

In the previous section it is described how to monitor the symmetry of the signed curvature distribution. If an asymmetry is found in such a distribution, the sensor positions should be changed correspondingly. In section 5.7 it is described how such a constrained can be introduced. The procedure requires iterations since the asymmetries are monitored after the alignment procedure has been applied once. In the second step, the desired corrections are added to the measurements and derivatives obtained and calculated from the track informations.
As a technical test of the procedure single muons of 500k Z^0 events and the same

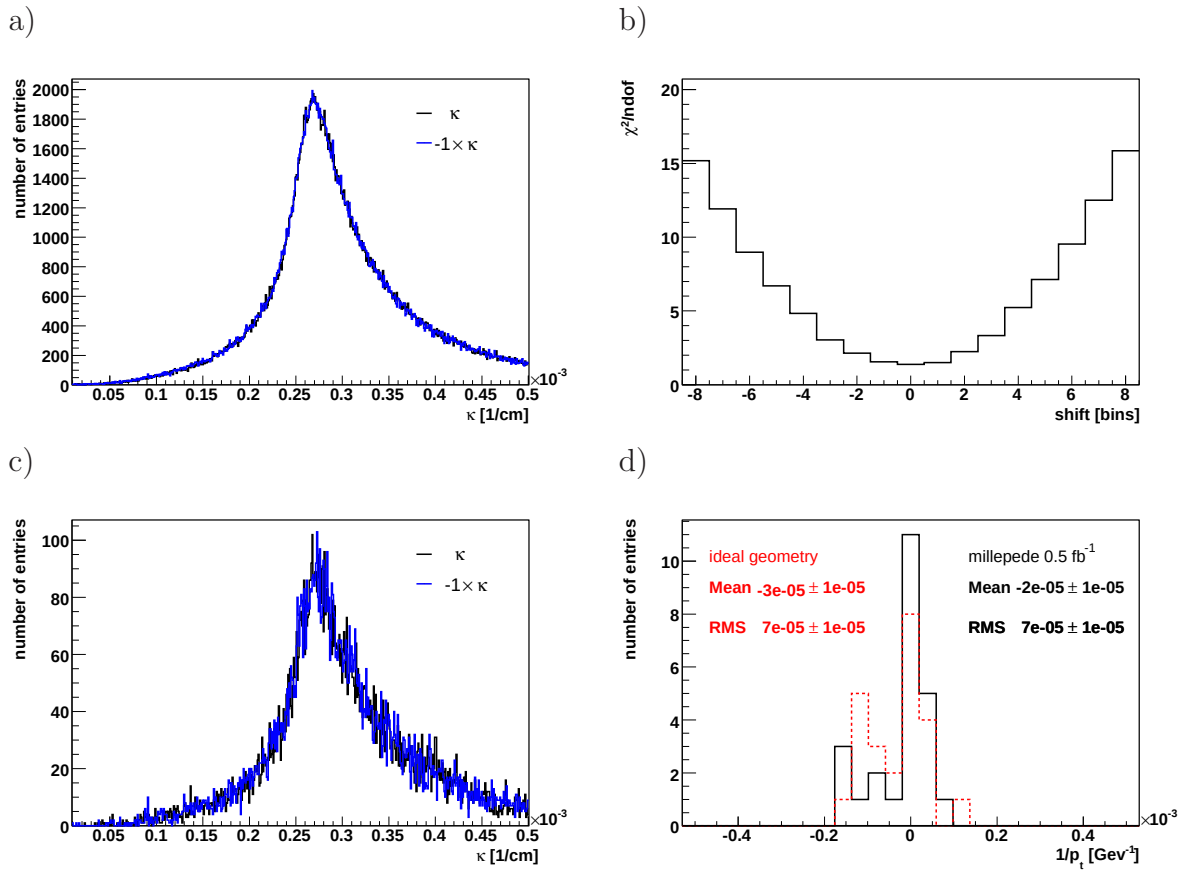

Figure 8.6: Monitor plots for the signed curvature symmetry. a: Signed curvature and -1 × signed curvature in the same histogram, b: Resulting $\frac{\chi^2}{\text{ndof}}$ (equation 8.1) for different shifts j of the signed curvature. c: signed curvature and -1 × signed curvature of tracks within a certain $\eta\phi$-bin in the same histogram, and d: signed curvature shifts determined by χ^2 minimizations for the 28 $\eta\phi$-bins. Results for the ideal geometry and a geometry determined by alignment using 0.5 fb^{-1} of integrated luminosity.

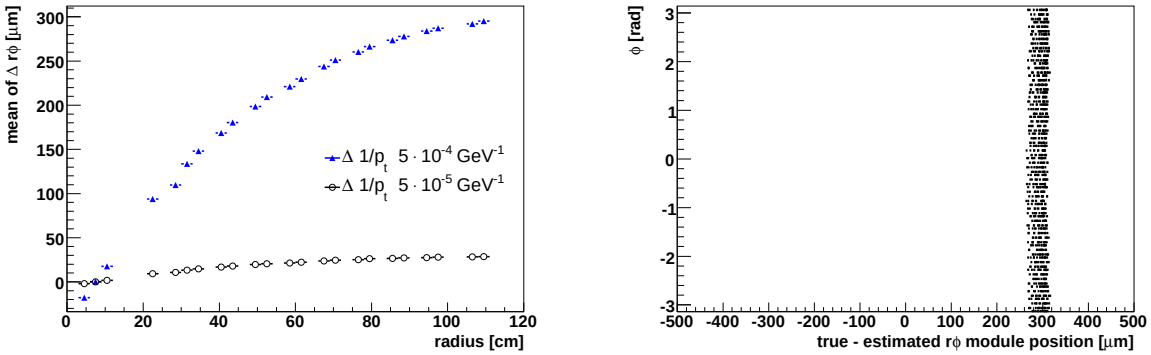

Figure 8.7: Left: Average displacement of modules in rϕ as a function of the module radial position for different signed curvature corrections. Right: Displacement of modules in rϕ in the last barrel layer as a function of the module ϕ position after a $5 \cdot 10^{-4}$ GeV^{-1} signed inverse transverse momentum correction has been enforced.

alignment parameters and constraints as for the 0.5 fb^{-1} scenario have been used. Starting from the ideal geometry, Millepede has been used to enforce geometries with an increase of the signed inverse transverse momentum by $5 \cdot 10^{-4}$ GeV^{-1} and $5 \cdot 10^{-5}$ GeV^{-1}, respectively. A bending deformation of the barrel modules is expected as a result of this procedure. In figure 8.7 (left) the average displacement in rϕ as a function of the radial module position is shown and the bending deformation is clearly evident. The maximal displacements occur in the last layer, since the pixel detector defines the coordinate system. A change of $5 \cdot 10^{-4}$ GeV^{-1} of the signed inverse transverse momentum leads to a displacement of about 300 μm for modules of the last layer as can be seen in figure 8.7 (right). The displacements do not depend on ϕ. The demanded change of $5 \cdot 10^{-5}$ GeV^{-1} lead to maximal displacements of $\sim 25\mu$m. This deformation translates to a bias of the transverse momentum of +1% at 200 GeV. This is a relatively large effect compared to the relative error of the transverse momentum measurement of only 2% at 200 GeV.

Figure 8.8 (left) shows the signed curvature and the signed curvature multiplied by -1 for muon tracks from 500k Z^0 events within a certain $\eta\phi$-region. The geometry which should lead to a shift of the inverse transverse momentum of $5 \cdot 10^{-4}$ GeV^{-1} has been applied, and the expected asymmetry is visible in figure 8.8. The curvature shift is determined via the fit described in the previous section. The resulting shifts for the 8 ϕ-bins in the barrel region are shown in figure 8.8 (right). The bias is correctly identified to be $5 \cdot 10^{-4}$ GeV^{-1}. The standard deviation of the resulting shifts is $5 \cdot 10^{-5}$ GeV^{-1} and can be understood as the uncertainty of the fitted parameter for an individual ϕ-bin. For comparison, also the resulting shifts from fits with ideal geometry and with the geometry resulting from the 0.5 fb^{-1} scenario studies without artificial curvature change are shown in figure 8.8 (right).

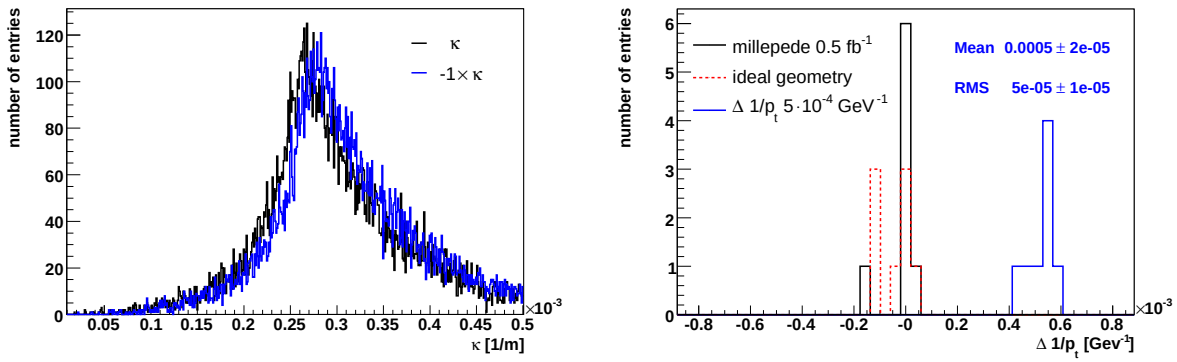

Figure 8.8: Left: Signed curvature and -1 × signed curvature of tracks within a certain $\eta\phi$-bin in the same histogram. The geometry resulting from enforcing a $5 \cdot 10^{-4}$ GeV^{-1} signed inverse transverse momentum correction has been applied. Right: signed curvature shifts determined by χ^2 minimizations for the 8 ϕ-bins. Results for the ideal and 0.5 fb^{-1} scenario and the curvature changing geometry are shown.

To visualize the impact of the bending deformation on physics results, typical distributions have been produced using the geometry with the $5 \cdot 10^{-4}$ GeV^{-1} curvature bias and 500k Z^0 events. The peak of the transverse momentum distribution of the muons close to half of the Z^0 mass is spread wider than that for the distribution obtained with the ideal geometry, as can be seen in figure 8.9 a. The closest distance of the track to the beam line is also systematically shifted, as shown in figure 8.9 b. The reason for the shift is that pixel sensors are used for the coordinate definition, as a result the pixel detector is not allowed to rotated exactly around the z-axis (figure 8.7 left). The increase of the reconstructed muon momentum in combination with the decreased momentum of the other muon leads to little impact on the reconstructed Z^0 mass (figure 8.9 c). Instead of a systematic shift of the mass of the Z^0, the bending deformation leads to an increased transverse momentum measurement of the Z^0 as can be seen in figure 8.9 d.

A different approach to monitor and correct the signed curvature bias is to compare the energy measured in the electromagnetic calorimeter with the track momentum determined by the curvature and the measurement of θ. The average relative difference should be the same for electrons and positrons. Such a method has been used for the W mass measurement [71] at the CDF detector at the Tevatron. However, this thesis concentrates on standalone tracker alignment and hence this approach was not followed.

In conclusion, the monitoring and correction for the bending deformation has been proven to work in principle. However, the identification of the deformation required very large displacements of the sensors. An alignment precision to the 10 μm level can not be achieved with this method and 0.5 fb^{-1} of data taking. More data and

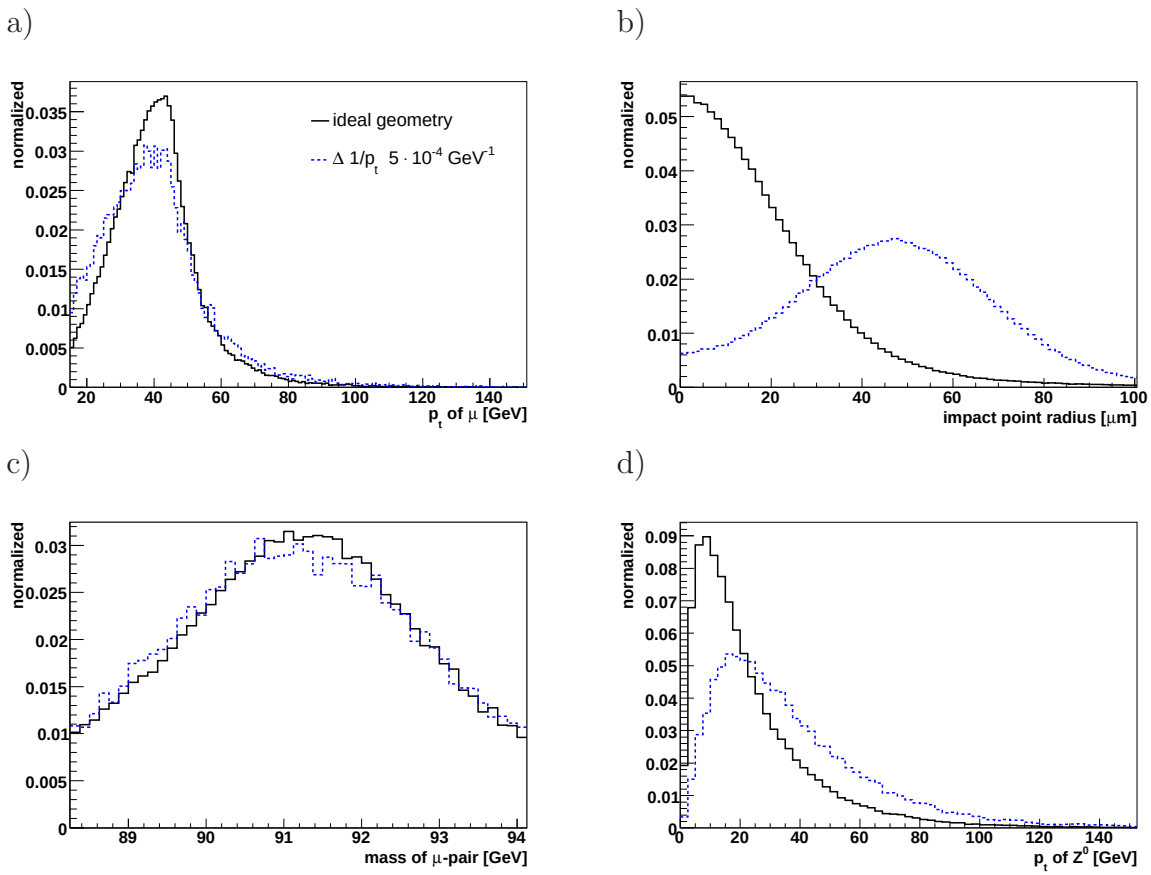

Figure 8.9: Distribution obtained with ideal geometry and a geometry with an enforced curvature change for $Z^0 \to \mu\mu$ events. a: Transverse momentum of muons, b: minimal distance of track to the beam line, c: invariant mass of muon pairs, and d: transverse momentum of the Z^0.

eventually the merging of W and Z^0 events for such fits could improve the precision of such methods and could serve as a useful tool in the long term. It is planned to implement similar methods directly into Millepede II [67]. Especially the W width measurement or searches for extra heavy Z bosons should include a monitoring and eventually corrections of bending deformations with distributions such as in figure 8.8.

Chapter 9

Conclusions

First the conclusions of the beam test measurements and alignment studies are given. Then an outlook on continuing studies is presented.

9.1 Beam Test Measurements

At the Large Hadron Collider (LHC) the high design luminosity of 10^{-34} $\mathrm{cm^2 s^{-1}}$ leads to a hostile radiation environment close to the interaction region, setting high demands on the radiation hardness of the CMS silicon tracking detector. Prototype silicon sensors of the CMS strip detector have been irradiated with protons up to a dose expected after 10 years of operation. These sensors have been tested in an electron beam at DESY II. The test beam setup, the slow control, the DAQ, and the data analysis tools have been prepared in the course of this thesis. A signal to noise ratio of 16 has been measured at a bias voltage of 450 V for the most severely irradiated module. This is well above the signal to noise ratio of $\sim$10 required for track reconstruction. The leakage current, inter strip coupling, and depletion voltage have been measured and were found to be within acceptable values. Hence there is no doubt that the high radiation doses will prevent the modules from operating up to their foreseen 10 years of operation.

9.2 Standalone CMS Tracker Alignment

The alignment of the CMS silicon tracking detector is a unique challenge compared to previously built detectors. The required sensor position uncertainties of a few μm, starting from $O(100)$ μm uncertainties, stems from the high resolution of the tracker. In addition, the size of the tracker, with about 16000 modules, leads to a computational challenge as geometry parameters for all 16000 modules need to be determined, many of which are highly correlated The aimed precision can only be achieved via track based alignment. However, certain deformations introduce a bias to the track parameter measurements, but leave the mean χ^2 of track fits unchanged.

This is particularly important because at LHC there are no single tracks with known momentum or vertex position which could be used as reference to reduce this bias.
Given this task, a sophisticated alignment strategy for the tracker needed to be developed. The alignment algorithm chosen was Millepede II [5]. It is a non-iterative algorithm for solving χ^2 minimization problems incorporating all correlations between the geometry parameters. It is capable of dealing with the large amount of position parameters at CMS.
Both types of degrees of freedom, i.e. those which can be determined by a χ^2 minimization using tracks and those which are χ^2 invariant, have been systematically studied to understand the most critical problem of alignment. The χ^2 invariant deformations have been systematically determined and classified (section 6.3). To constrain these deformations, all available complementary sources of information have been used.
A key ingredient is the use of complementary datasets like those from pp interactions at the central vertex and cosmic ray muons, which connect different tracker parts via tracks. The reconstruction and detector settings for cosmic muon data have been tuned and a large dataset has been produced for alignment studies. The cosmic muons turn out to reduce some χ^2 invariant deformations, however other deformations remain. Vertex constrained and mass constrained $Z^0 \rightarrow \mu\mu$ decays have been used, but turned out to be not sufficient to reduce all deformations. The results were used as arguments for an efficient cosmic muon trigger setup at CMS.
The prior knowledge about the mechanical mounting and survey measurement precisions is implemented in the alignment procedure. The correlated nature of the initial displacements of the sensors (with respect to the global frame), due to the displacements of large mechanical support structures, is also utilized for alignment. A hierarchical structure of alignment parameters has been introduced, which reflects the mechanical support frames. This turned out to be an efficient tool to reduce χ^2 invariant deformations (section 6.4).

All previously mentioned ingredients were used for a full scale alignment study, aligning all modules of the CMS silicon tracker in one go. A *first data* misalignment scenario[1], which represents the displacement at startup, has been used as the initial misalignment. Events from Z^0 and W decay equivalent to 0.5 fb^{-1} of integrated luminosity and cosmic muons data have been used. The positions are determined with an uncertainty in the order of 10 μm to 25 μm for the silicon strip sensors in the precisely measured direction of the sensors. For the pixel detector, a precision of a few μm is achieved. The bias on the transverse momentum measurement is reduced from a several percent level for 100 GeV transverse momentum tracks to about a permille after alignment (figure 9.1). The transverse momentum resolution (σ of gauss fit) is degraded by less than half a permille (figure 9.1) with respect to the ideal geometry. After alignment the vertex position resolution is changed negligibly and the vertex is systematically shifted at the μm level. Overall, the tracker is well calibrated and the

[1]The current default *first data* misalignment scenario of CMS [3].

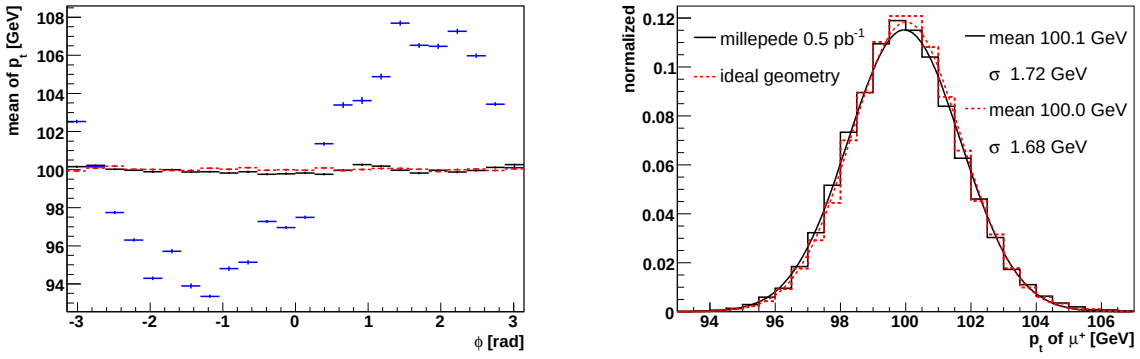

Figure 9.1: Comparison of resulting distributions from μ^+, which have a transverse momentum of exactly 100 GeV, with ideal, aligned and misaligned geometry. Left: Mean transverse momentum as a function of ϕ in the barrel region. Right: Resolution of the transverse momentum measurement at 100 GeV.

impact on physics measurements would be very small.
The CPU-time of the actual position parameter calculation has been only ∼2h and 2 GB of memory were required. This is remarkable, since the incorporation of all correlations is computationally a challenging task and only algorithms avoiding this had been proposed so far.
The result of this study marks a breakthrough at CMS since for the first time a successful alignment concept for full CMS tracker has been presented. However, this is a study utilizing simulated data and the real data will lead to further challenges discussed in the next section.

Critical Discussion

The results of the study show that the tracker can be aligned to high precision. However a small χ^2 invariant deformation remains (section 7.2). Global correlations remain very high even if cosmics muons or Z^0 events with vertex and mass constraint are used (section 6.5), indicating that further data needs to be utilized. Therefore, prior knowledge about the uncertainty of the sensor positions and about the correlations between displacements of the sensors due to their common mechanical support structures is used. Such information require a precise understanding of the support structures and likely deformations of them. Since for alignment and misalignment simulation the same position parameters (rigid body parameters) are used, the information about the correlations of displacements is exact in this thesis.
In addition, the simulation of the initial *first data* misalignment which defines the starting value for this study is quite, but not completely, realistic. The pixel detector is assumed to be aligned with the very first data to a 15 μm level[2]. The individual sensors are not rotated and complex deformations like twists and shearings do not

[2]First studies indicate that this is a reasonable assumption.

occur in this simulation. On the other hand, data from beam halo muons and laser trajectories are expected to be sensitive to twist deformations. They will generally reduce χ^2 invariant deformations, hence more emphasis can be given to the event data and the prior knowledge has less impact. Unfortunately, no simulated data for beam halo muons, laser trajectories and survey measurements was available. Further systematic uncertainties, like the magnetic field uncertainty or thermal movements, are not yet included. However, the alignment strategy and the developed alignment tools are fully able to take these into account once they become available.

Outlook

Currently cosmic muon data is taken in the tracker test facility and 25% of the tracker modules are read out. This will make it possible to test the alignment strategy with real data on a large scale. The production of simulated beam halo and laser alignment data is ongoing. These additional complementary datasets will even improve the alignment procedure.
A mandatory step for the future will be to identify observables to monitor the success of alignment in real data, especially χ^2 invariant deformations. First ideas for this are developed in section 8.1. The alignment strategy and alignment tools developed here can be used to align the CMS tracker with real data and even more complementary datasets than utilized in this thesis will be available.

Appendix A

Tracker Support Structures

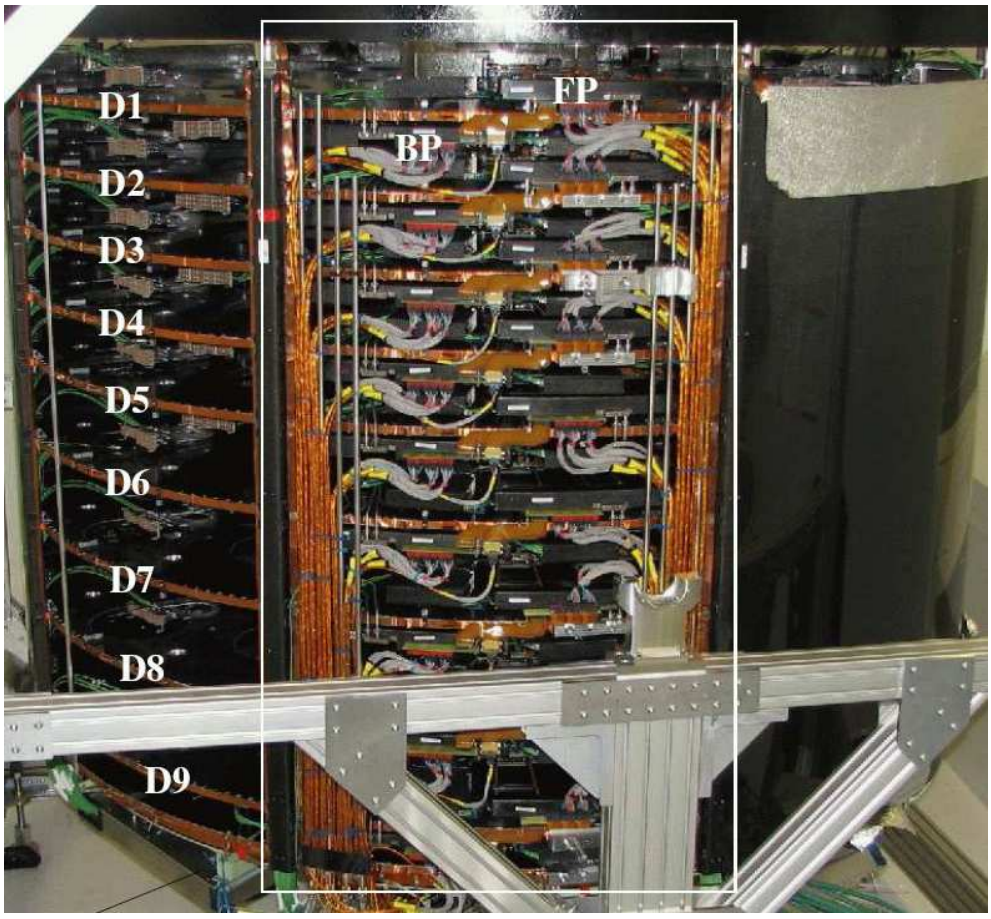

Figure A.1: The TEC+, Dx indicate the disk numbers. FP the position of a forward petal, and BP the position of backward petal. The vertical direction corresponds to th z direction of the CMS detector.

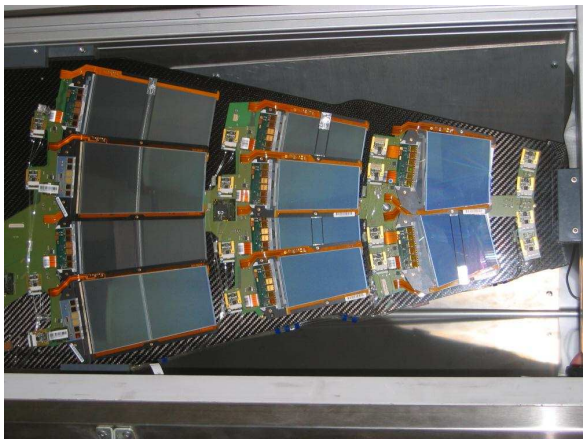

Figure A.2: Modules mounted on a petal supporting structure.

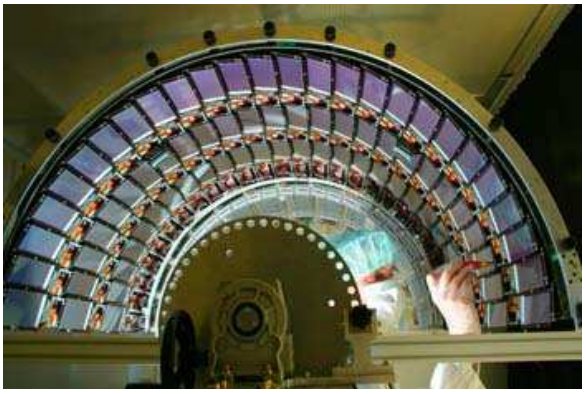

Figure A.3: Mounting of a string (3 modules) on a half shell of the TIB.

Figure A.4: Left: A Ring of the TID. Right: A TID disk composed of three rings.

Figure A.5: The TOB frame structure. Rods are directly mounted into this structure.

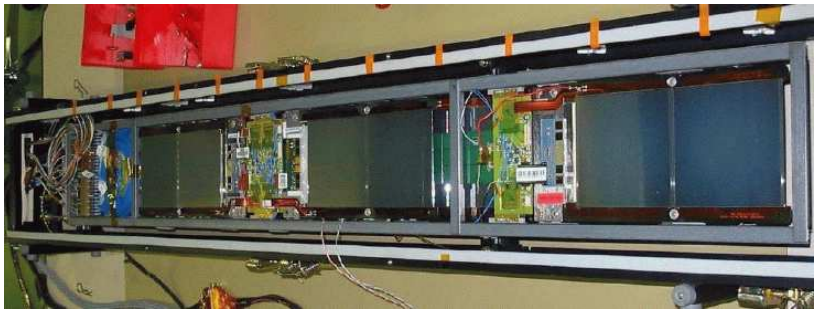

Figure A.6: A Rod supporting structure.

Appendix B

Combined Test Beam Reconstruction Software

A schematic illustration of the software is given in figure B.1. The **MergeDataTree** is the base class for the data storage. The **TrackTree** stores the reconstructed tracks, the **HitTree** stores the hits and the **AlignmentTree** stores the position of the sensors in the global frame. **MergeDataBase** is the base class for reconstruction. **TelMergeDoT** is an abstract class, which reads the telescope ntuples and has virtual functions to read the device under test data. **TelMergeCMS** is the concrete implementation for CMS, supporting the reading of CMS module data. The **MergeReAlign** class and the **MergeReFitTrack** classes finalize the reconstruction. All hits from the **HitTree** are transformed to the global frame via the **SensorGeometry** class.

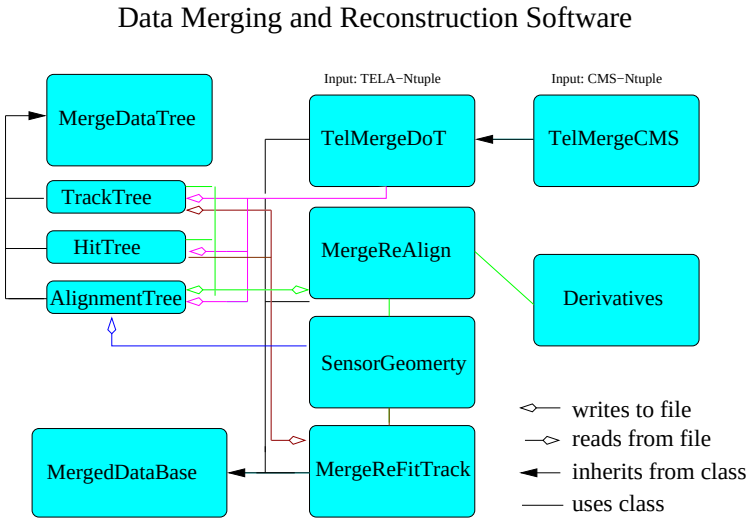

Figure B.1: Schematic illustration of the software merging the CMS-module data stream and the telescope data stream.

Appendix C

Details on Alignment

C.1 Global Derivatives of the Residuum

In this section the global derivatives are calculated. The notation and definitions introduced in section 5.4 are used. The derivative is calculated at the natural linearization point, which is the ideally aligned detector. The alignment corrected position $\mathbf{q}_a$ of the initial hit position $\mathbf{q}_h$ is:

$$\mathbf{q}_a = \Delta\mathbf{R}\mathbf{q}_h + \Delta\mathbf{q} \tag{C.1}$$

The used hit position $\mathbf{q}_h$ should be the best prior estimate of the position and can be a mixture of the initial measurement $\mathbf{q}_m$ and the initially predicted penetration point $\mathbf{q}_p$. The correction angles α, β and γ are assumed to be smaller than a few mrad, such that the linearizion of the rotations is valid. The derivatives of the rotation correction matrix at the point $\alpha = \beta = \gamma = 0$ are:

$$\frac{\partial\Delta\mathbf{R}}{\partial\alpha} = \begin{pmatrix} 0 & 0 & 0 \\ 0 & 0 & 1 \\ 0 & -1 & 0 \end{pmatrix} \quad \frac{\partial\Delta\mathbf{R}}{\partial\beta} = \begin{pmatrix} 0 & 0 & -1 \\ 0 & 0 & 0 \\ 1 & 0 & 0 \end{pmatrix} \quad \frac{\partial\Delta\mathbf{R}}{\partial\gamma} = \begin{pmatrix} 0 & 1 & 0 \\ -1 & 0 & 0 \\ 0 & 0 & 0 \end{pmatrix} \tag{C.2}$$

The derivatives for the measured point are therefore:

$$\frac{\partial\mathbf{q}_a}{\partial\mathbf{a}} = \begin{pmatrix} 1 & \frac{\partial\Delta\mathbf{R}}{\partial\alpha}\mathbf{q}_h & \frac{\partial\Delta\mathbf{R}}{\partial\beta}\mathbf{q}_h & \frac{\partial\Delta\mathbf{R}}{\partial\gamma}\mathbf{q}_h \end{pmatrix} = \begin{pmatrix} 1 & 0 & 0 & 0 & -w_m = 0 & v_m \\ 0 & 1 & 0 & w_m = 0 & 0 & -u_m \\ 0 & 0 & 1 & -v_m & u_m & 0 \end{pmatrix}$$

w_h is by definition 0, since the hit $\mathbf{q}_h$ is on the sensor surface. It is furthermore needed to calculate the derivative of the predicted measurement with respect to the alignment corrections. The predicted measurement is the propagation of the fitted track to the surface of the sensor. Only the movement along the normal (w-axis) of the sensor will change the plane to which the trajectory is propagated. The movement of the sensor plane in the vicinity of the hit is equivalent to the movement of the hit.

Hence the chain rule can be applied:

$$\frac{\partial \mathbf{q}_p}{\partial \mathbf{a}} = \frac{\partial \mathbf{q}_p}{\partial \mathbf{q}_a}\frac{\partial \mathbf{q}_a}{\partial \mathbf{a}} = \begin{pmatrix} 0 & 0 & \frac{du_p}{dw} \\ 0 & 0 & \frac{dv_p}{dw} \\ 0 & 0 & 1 \end{pmatrix} \frac{\partial \mathbf{q}_h}{\partial \mathbf{a}} = \begin{pmatrix} 0 & 0 & \frac{du_p}{dw} & -v_h\frac{du_p}{dw} & u_h\frac{du_p}{dw} & 0 \\ 0 & 0 & \frac{dv_p}{dw} & -v_h\frac{dv_p}{dw} & u_h\frac{dv_p}{dw} & 0 \\ 0 & 0 & 1 & 0 & u_h & 0 \end{pmatrix}$$

The derivative of distance between the predicted and true hit position then becomes:

$$\frac{\partial \mathbf{q}_p}{\partial \mathbf{a}} - \frac{\partial \mathbf{q}_a}{\partial \mathbf{a}} = \begin{pmatrix} -1 & 0 & \frac{du_p}{dw} & -v_h\frac{du_p}{dw} & u_h\frac{du_p}{dw} & -v_h \\ 0 & -1 & \frac{dv_p}{dw} & -v_h\frac{dv_p}{dw} & u_h\frac{dv_p}{dw} & u_h \\ 0 & 0 & 0 & 0 & 0 & 0 \end{pmatrix} \tag{C.3}$$

For two dimensional measurements a change in the hit position $\Delta\mathbf{q}_a$ translates to an equivalent shift of the measurement $\Delta\mathbf{q}_m$. The w coordinate is by definition zero and can be neglected. The derivatives of the residuum are then the first two rows of equation C.3. For a one dimensional measuring sensor the derivatives are the first row, if the sensitive coordinate at the measured point $\mathbf{q}_m$ is parallel to u. If the sensitive coordinate differs from u at at the measured point $\mathbf{q}_m$ the residuum needs to be defined in a different coordinate system, in oder to be reduced to one dimension. One coordinate needs to be the sensitive coordinate, the other the insensitive one. If ϕ is the angle between the sensitive coordinate and u, then the projection $\mathbf{P}$ to the sensitive coordinate is:

$$\mathbf{P} = \begin{pmatrix} \sin^2\phi & \sin\phi\cos\phi & 0 \end{pmatrix}$$

The derivative of the residuum with respect to the alignment parameters is:

$$\frac{\partial \mathbf{r}}{\partial \mathbf{a}} = \mathbf{P}(\frac{\partial \mathbf{q}_p}{\partial \mathbf{a}} - \frac{\partial \mathbf{q}_a}{\partial \mathbf{a}}) \tag{C.4}$$

C.2 Transformation from Composite to Subcomponent Alignment Parameters

The alignment parameters of a composite object $\mathbf{a}_c$ can be transformed to a set of its subcomponents alignment parameters $\mathbf{a}_i$ (5.4.4). The corresponding matrices $\mathbf{C}_i$ are calculated in this section. The matrix $\mathbf{C}_i$ is the linearizion of a nonlinear transformation(includes rotations). The alignment corrections are small, hence this is perfectly valid. The linearizion point chosen is $\mathbf{a}_c = 0$. The transformation matrix $\mathbf{C}$ can be divided into four parts.

$$\mathbf{C} = \begin{pmatrix} \mathbf{C}_{11} & \mathbf{C}_{12} \\ \mathbf{C}_{21} & \mathbf{C}_{22} \end{pmatrix}$$

$\mathbf{C}_{11}$ represents the transformation of translations of the composite structure to translations of the subcomponent. The translation alignment corrections of the composite structure need to be transformed to the local coordinate system of the subcomponent.

$$\mathbf{C}_{11} = \mathbf{R}_s \mathbf{R}_c^T$$

$\mathbf{R}_s$ is the orientation matrix 5.8 of the subcomponent and $\mathbf{R}_c$ the orientation matrix of the composite object.

$\mathbf{C}_{12}$ represents the change of the position of a subcomponent due to the rotation corrections of the composite structure. The first column $\mathbf{C}_{12}^1$ of the matrix is determined by:

$$\mathbf{C}_{12}^1 = \mathbf{R}_s(\mathbf{R}_c^T \frac{\partial \Delta \mathbf{R}}{\partial \alpha} \mathbf{R}_c(\mathbf{r}_{s0} - \mathbf{r}_{c0}))$$

$\mathbf{r}_{s0}$ is the origin in global coordinates of the local coordinate system of the subcomponent and $\mathbf{r}_{c0}$ the origin of the composite structure. $\frac{\partial \Delta \mathbf{R}}{\partial \alpha}$ can be found in Appendix C.1 equation C.2. For the second and third column α has to be exchanged with β and γ respectively.

$\mathbf{C}_{21}$ transforms translations of the composite structure to rotations of the subcomponent and is therefore obviously zero.

$\mathbf{C}_{22}$ translates rotations of the composite object to rotations of the subcomponent. The first column $\mathbf{C}_{22}^1$ of the matrix is determined as follows:

$$\mathbf{R}_{22}^{\alpha} = \mathbf{R}_s(\mathbf{R}_c^T \frac{\partial \Delta \mathbf{R}}{\partial \alpha} \mathbf{R}_c) \mathbf{R}_s^T$$

The linearely approximation euler angles of $\mathbf{C}_{22}^1$ build the first column $\mathbf{C}_{22}^1$. Again, for the second and third column α has to be exchanged with β and γ respectively.

C.3 χ^2 Invariant Deformations

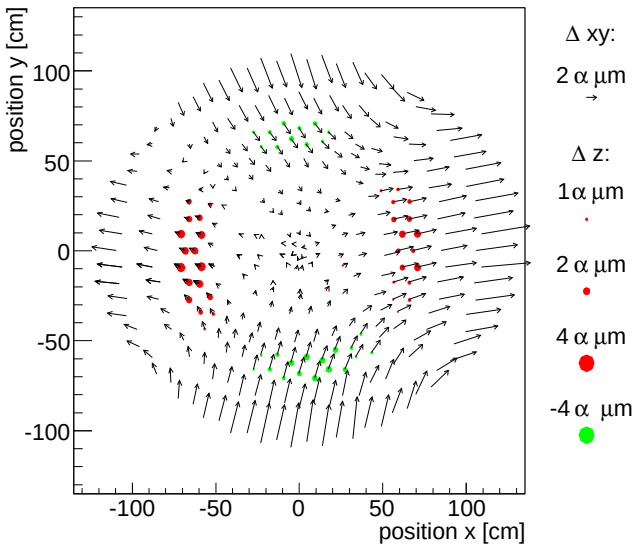

Figure C.1: Illustration of the eigenvector of the second r-rϕ oscillation. The phase of the oscillation is shifted by 45° in comparison to figure 6.18.

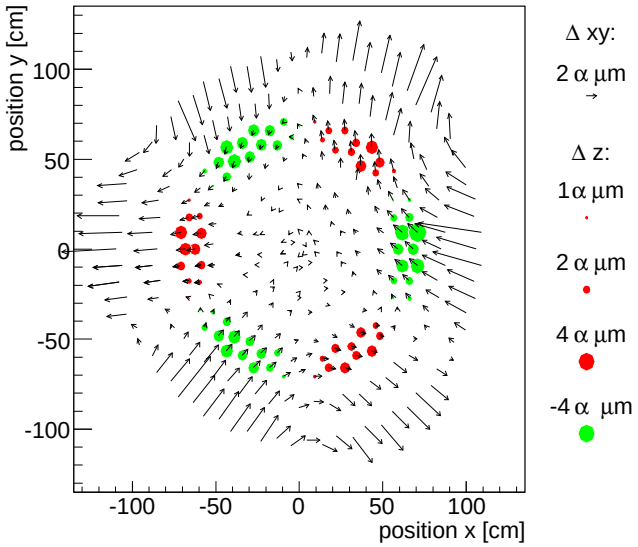

Figure C.2: Illustration of the eigenvector of the third r-rϕ oscillation. The phase of the oscillation is shifted by 30° in comparison to figure 6.19.

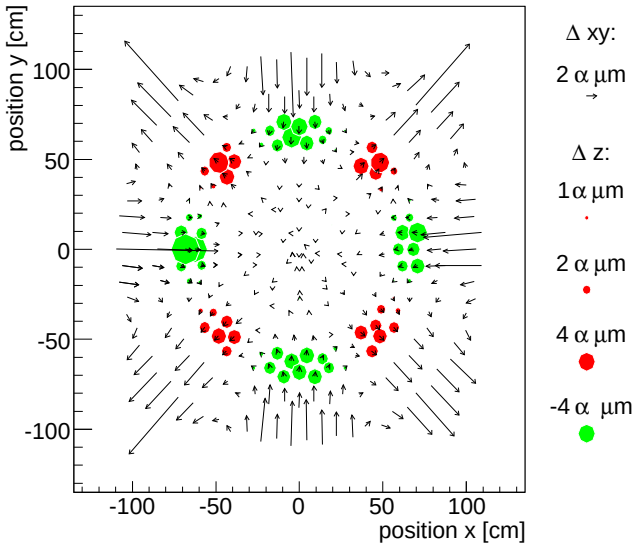

Figure C.3: Illustration of the eigenvector of the forth r-rϕ oscillation.

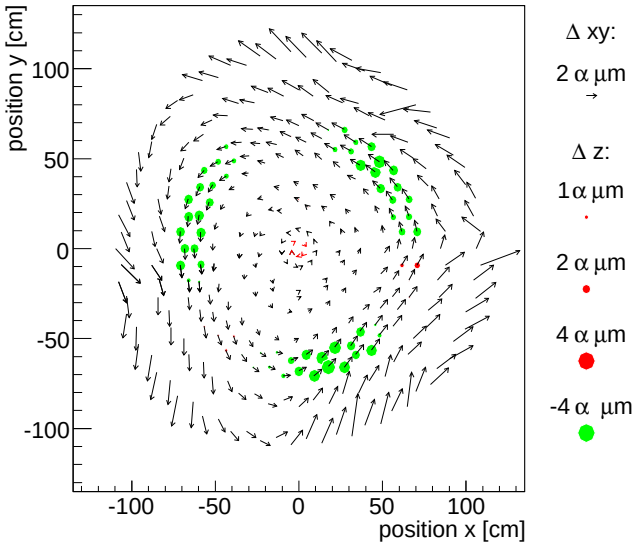

Figure C.4: Illustration of the eigenvector of the rϕ shearing and a r-rϕ oscillation.

Bibliography

[1] CMS Collaboration, "Addendum to the CMS Tracker TDR by the CMS collaboration," CERN/LHCC 2000-16 CMS TDR Addendum 1, (2000).

[2] CMS Collaboration, "Detector performance and software," Physics TDR Volume I, CERN/LHCC 2006-001, CMS TDR 8.1, (2006).

[3] P. Vanlaer et al., "Impact of CMS silicon tracker misalignment on track and vertex reconstruction," CMS-NOTE 2006-029, (2006).

[4] G. Steinbrück, "Impact of misalignment on physics", proceedings of the I. LHC Alignment Workshop 2006, (2007).

[5] V. Blobel, "Millepede II Manual Draft", http://www.desy.de/ blobel (2007).

[6] ATLAS Collaboration, "ATLAS detector and physics performance," CERN/LHCC 99-14, ATLAS TDR 14, (1999).

[7] CMS Collaboration, "Physics Performance," CERN/LHCC 2006-021, CMS TDR 8.2, (2006).

[8] C. H. Lai, "Gauge theory of weak and electromagnetic interactions selected papers", World Scientific Publishing, ISBN 9-971-83022-1, (1981).
Includes reprints the decisive papers of S. L. Glashow, S. Weinberg, and A. Salam.

[9] P. W. Higgs, "Broken symmetries, massless particles and gauge fields," Physical Letters 12, page 132, (1964).
P. W. Higgs, "Higgs Spontaneous symmetry breakdown without massless bosons," Physical Review, 145, page 1156 (1966).

[10] H Georgi et al., "Unity of all elementary particle forces," Physical Review, D10, page 897, (1974).

[11] H. T. Haber et al., "The search for supersymmetry: probing physics beyond the standard model," Physics Reports 117, page 75, (1985).

[12] J M Campbell et al., "Hard interactions of quarks and gluons: a primer for LHC physics," Rep. Prog. Physics, Volume 70, page 89-193, (2007).

[13] The LEP Electroweak Working Group, http://lepewwg.web.cern.ch/LEPEWWG/ (May 2007).

[14] CMS Collaboration, CMS Tracker TDR, CERN/LHCC 98-6 CMS TDR 5, (1998).

[15] R.L. Glückstein, "Uncertainties in track momentum and direction, due to multiple scattering and measurement errors," Nuclear Instruments and Methods, Volume 24, page 143-147, (1963).

[16] S. Cucciarelli et al., "Position determination of the pixel Hits," CMS-NOTE 2002-049, (2002).

[17] R. Adolphi, "Construction and calibration of the laser alignment system for the CMS tracker," PhD Thesis, RWTH-Aachen, (2006).

[18] M. Thomas, "Monte Carlo simulation of the laser alignment system of the CMS tracker," PhD Thesis, RWTH-Aachen, (expected 2007).

[19] CMS Collaboration, "CMS reconstruction package," outdated 2006, http://cmsdoc.cern.ch/orca

[20] W. Adam et al., "Track reconstruction in the CMS tracker", Nuclear Instruments and Methods A, Volume 559, page 143-147, (2006).

[21] C. Berger, "Elementarteilchenphysik", Springer-Verlag, ISBN 3-540-41515-7, (2002).

[22] CMS Collaboration, "The electromagnetic calorimeter technical design report," CERN/LHCC 97-33, CMS TDR4,(1997).

[23] CMS Collaboration, "The hadron calorimeter technical design report," CERN/LHCC 97-31, CMS TDR2, (1997).

[24] CMS Collaboration, "The muon project technical design report," CERN/LHCC 97-32, (1997).

[25] D. Contarato "Silicon detectors for particle tracking at future high-energy physics experiments," PhD Thesis, University of Hamburg, DESY-THESIS-1005-044, (2005).

[26] J.-L. Agram et al., "The silicon sensors for the Compact Muon Solenoid tracker design and qualification procedure," Nuclear Instruments and Methods A, Volume 517, Issues 1-3, (2004).

[27] ST Microelectronics, http://www.st.com

[28] Hamamatsu Photonics, http://www.hamamatsu.com

[29] R. Chierici et al., "The effect of highly ionizing events on the APV25 readout chip," CMS-NOTE 2002-038, (2002).

[30] http://adweb.desy.de/∼testbeam/

[31] C. Colledani et al., "A submicron precision silicon telescope for test beam purposes," Nuclear Instruments and Methods A, Volume 372, page 379-384, (1996).

[32] M. Milite, "The internal structure of charmed jets in photoproduction at Hera and tests of the Zeus microvertex silicon sensors," PhD Thesis, University of Hamburg, DESY-THESIS-2001-050, (2001).

[33] M. Moritz, "Measurement of the high Q^2 neutral current DIS cross section at HERA," PhD Thesis, University of Hamburg, DESY-THESIS-1999-040, (1999).

[34] http://www.pi.ws/products/micropositioning.htm

[35] J. French et al., "Design and results from the APV25, a deep-submicron CMOS front end chip for the CMS Tracker," Nuclear Instruments and Methods A, Volume 462, page 359-365, (2001).

[36] M. Axer et al., "The ARC system - the appropriate test system in CMS Tracker module production," Nuclear Instruments and Methods A, Volume 535, page 374-378 (2004).

[37] M. Axer et al., "Test of CMS tracker silicon detector modules with the ARC readout system," Nuclear Instruments and Methods A, Volume 518, page 321-323, (2004).

[38] S. Gadomski et al., "The deconvolution method of fast pulse shaping at hadron colliders," Nuclear Instruments and Methods A, Volume 320, page 217-227, (1992).

[39] P. Murray, "APVMUX User Guide," Version 1.0, (2000).

[40] R. Brun and F. Rademakers, "ROOT - An object oriented data analysis framework," Proceedings AIHENP'96 Workshop, Lausanne, Nuclear Instruments and Methods A, Volume 389, page 81-86, (1997).
See also http://root.cern.ch/

[41] M. Bleyl, "Testbeam measurements on CMS silicon strip detectors," Diploma Thesis, University of Hamburg, (2005).
http://www.desy.de/∼schleper/Group/cms.html

[42] W. Adam et al., "Design and test beam performance of substructures of the CMS Tracker End Caps," CMS-NOTE 2005-025, (2005).

[43] CMS Collaboration, "CMS reconstruction package," http://cmsdoc.cern.ch/cmssw.

[44] E. Butz., PhD Thesis, University of Hamburg, expected (2008).

[45] Paul Avery, "Applied fitting theory IV: Formulas for track fitting," CLEO-NOTE, CBX 92-45, (1992).

[46] I. Belotelov et al., "Simulation of misalignment scenarios for CMS tracking devices," CMS-NOTE 2006-008, (2006).

[47] A. Ostapchouk et al., "The alignment system of the CMS Tracker," CMS-NOTE 2001-053, (2001).

[48] CMS Collaboration, "CMS simulation package," http://cmsdoc.cern.ch/oscar

[49] Claus Kleinwort, private communication, (2006).

[50] Rainer Mankel, private communication, (2006).

[51] V. Drollinger, "Simulation of beam halo and cosmic muons," CMS-NOTE 2005-012, (2005).

[52] CMS Collaboration, "CMS physics generator interface package," http://cmsdoc.cern.ch/cmsoo/projects/CMKIN/

[53] S. Eidelman et al., "The review of particle physics," Physical Letters, B592 1, (2004).

[54] F. Berman et al., "Grid computing: making the global infrastructure a reality," John Wiley & Sons, ISBN 047085319, (2004).

[55] "Job description language, how-to," DataGrid-01-TEN-0102, (2001). http://www.grid.org.tr/servisler/dokumanlar/DataGrid-JDL-HowTo.pdf

[56] S. Agostinelli et al., "GEANT4: a simulation toolkit," Nuclear Instruments and Methods A, Volume 506, page 250-303, (2003).

[57] National Instute of Standards and Technology, http://www.nist.gov, (2007).

[58] V. Blobel and C.Kleinwort, "A new method for high-precision alignment of track detectors," Contribution to the Conference on Advanced Statistical Techniques in Particle Physics, Durham, hep-ex/0208021, March 18-22 (2002).

[59] V. Blobel and E. Lohrmann, "Statistische und Numerische Methoden der Datenanalyse," Teubner, ISBN 3-519-03242-0, (1998).

[60] Paul Avery, "Applied fitting theory IV: General least squares fitting theory," CLEO-NOTE, CBX 92-45, (1992).

[61] A. Strandlie, "Propagation of covariance matrices of track parameters in homogeneous magnetic fields in CMS," CMS-NOTE 2006/001, (2001).

[62] Edmund Widl, "CMS-Tracker alignment with a Kalman filter method," PhD thesis, expected (2008).

[63] V.Karimaki et al., "The HIP algorithm for track based alignment and its application to the CMS pixel detector," CMS-NOTE 2006/018 (2206).

[64] W. Adam et al., "A Kalman Filter for track-based alignment," CMS-NOTE 2006/022, (2006).

[65] R. Barrett et al. "Templates for the solution of linear systems: building blocks for iterative methods," SIAM, 2nd Edition, (1994).

[66] C. C. Paige and M. A. Saunders, "Solution of sparse indefinite systems of linear equations," SIAM, Numerical Analysis 12, page 617-623, (1975),

[67] Volker Blobel, private communication, (2007).

[68] M. Paterno, "Calculating efficiencies and their uncertainties," FERMILAB-TM-2286-CD, (2004).

[69] Ian Tomalin, private communication, (2006).

[70] P. Brückman et al., "Least squares approach to the alignment of the generic high precision tracking system," Proceedings of PHYSTAT/2005, (2005).

[71] CDF Collaboration, F. Abe et al., "Measurement of the W boson mass," Phys. Rev. D 52, 4784 - 4827, (1995).

Danksagung

Bedanken möchte Ich mich bei meinen Gutachtern Peter und Prof. Mnich. Für das Korrigieren der Arbeit bedanke Ich mich bei Georg, Gero, Prof. Blobel, Roger und Christian. Besonders möchte Ich Prof. Blobel für lehrreiche Diskussionen danken und für die Verfügungstellung des Programms Millepede II. Für die Erlösung von büreaukratischen Problemen gilt mein Dank Uwe Pein. Die gute Arbeitsathmosphäre ist der gesamten Arbeitsgruppe ZEUS-CMS zu verdanken.
Für stetige Unterstützung danke Ich meiner Familie und Oldona.